Magnetic properties of Terbium-Scandium Alloys

D. Chatterjee

Magnetic Properties of Terbium-Scandium Alloys

by

D. Chatterjee, M.Sc.

Presented in candidature for the degree of

Doctor of Philosophy

January 1972

ABSTRACT

Measurements have been made of the lattice parameters, density and magnetic characteristics of a series of alloys between Terbium and Scandium. Both single crystal and polycrystalline materials have been used in this investigation. It is found that the lattice parameters show a slight deviation from Vegard's Law. The Néel temperatures follow a $T_N \propto \bar{G}^{1.33}$ dependence unlike the rare earth metals and other alloy systems, where a $T_N \propto \bar{G}^{0.66}$ law is obeyed. ($\bar{G}$ = effective de Gennes function). The paramagnetic Curie points show an approximate dependence on $\bar{G}^2$ unlike the $\theta_p \propto \bar{G}$ variation observed for the rare earth metals and the alloys with Yttrium.

Thermal expansion and magnetostriction measurements have been made along the principal directions of single crystals of alloys of composition $Tb_{0.89}Sc_{0.11}$ and $Tb_{0.825}Sc_{0.175}$. An estimate of the exchange constants and their derivatives has been made for the alloy $Tb_{0.89}Sc_{0.11}$ with the help of the turn angle data provided by Dr. H.R. Child.

The contribution of magnetostrictive energy has been estimated in the two alloys following Cooper's analysis. It is observed that the magnetostrictive energy drops rapidly with composition and this is assumed to be the cause of the absence of ferromagnetism even in materials containing fairly high proportion of Terbium.

Page No.

List of Figures

LIST OF TABLES

CHAPTER 1

INTRODUCTION

1.1.(a) Electronic Structure of Rare Earths

A brief summary of the principal physical properties of the rare earth metals is relevant in a report on the investigation of the properties of a rare earth alloy system.

The members of Group IIIA of the periodic table (Atomic nos. 57 to 71) are collectively known as the 'Rare Earths'. The lanthanides, as they are alternatively classified, have very similar chemical properties. This is due to the essentially unchanged outer electron configuration through the series. The general representation

$$\left[(Xe)\ 4d^{10}\ 4f^{n}\ 5s^{2}\ 5p^{6} \right]^{+++}$$

where n increases from 0 to 14 from La(Z = 57) to Lu(Z = 71) and (Xe) denotes the Xenon core fits the trivalent rare earth ions with the exceptions of Europium and Ytterbium. They are normally divalent. The outer (5d 6s) electrons are removed easily to form these ions. The 4f shell lies deep in the atom shielded by the 5s and 5p shells and is generally assumed to be tightly bound and localised.

Scandium (Z = 21) and Yttrium (Z = 39)are frequently classified as rare earths because of their similar electronic and crystal structures.

1.1.(b) Crystal Structure of Rare Earths

As the nuclear charge increases through the series, there is growing attraction for the orbital electrons and the atomic radius decreases while the density increases. This decrease in size with increasing Z (known as the lanthanide contraction) results in a progressive increase in bond strength if the number of bonding electrons stays constant. This is manifested in increasing melting

points. This regular behaviour is not followed by Eu and Yb because of their divalent nature.

The seven elements La to Eu are known as the light rare earths, while the rest are called the heavy rare earths. Among the light rare earths, La, Pr and Nd exhibit a double hexagonal close-packed structure (d.h.c.p.) with packing sequence ABACABAC .... at room temperature while Ce has a f.c.c. and Eu a b.c.c. structure. La however transforms to a f.c.c. structure at higher temperatures while Ce shows the formation of a d.h.c.p. phase below 260°K. There is also a collapsed phase in Ce at low temperatures. Sm has a complicated nine-layer hexagonal close packed structure with a stacking sequence ABCBCACAB .... . The structure of Pm has not yet been reported.

The heavy rare earths together with Y and Sc exhibit a simple h.c.p. structure at room temperature with a stacking sequence ABAB.. . The exception is Yb which is f.c.c. The magnetic ordering at low temperature in certain rare earths (e.g. Dy) has been reported to be accompanied by a change to orthorhombic structure. The lowering of symmetry can also be treated as a deformed h.c.p. phase. Most of the rare earths which have hexagonal structure at room temperature, transform to a body centred cubic phase as they approach their melting points. The exceptions are Er, Tm and Lu. GSCHNEIDNER (1) discusses these in detail in his book.

1.2. Magnetic Properties and Magnetic Structure of Rare Earths

The 4f shell in the rare earths has been the subject of a great deal of attention to explain the magnetic properties. The 4f electrons can be specified by the appropriate combinations of the magnetic quantum number (+3 to -3) with the spin states $+\frac{1}{2}$ and $-\frac{1}{2}$.

The ionic S, L and J (spin angular momentum, orbital angular momentum and the total angular momentum) may be calculated using Hund's rule, Pauli's principle and Russell-Saunders coupling. The orbital and spin momenta couple antiparallel in a shell which is less than half full (i.e. J = L-S) and couple parallel when the shell is more than half full (i.e. J = L+S). The observed ionic moment compares well with the value $g\mu_B\sqrt{J\ (J+1)}$, where g is the Landé factor and μ_B is the Bohr magneton. The exceptions are Sm and Eu. The discrepancy is cleared by using Van Vleck's postulate of contribution to susceptibility from higher energy states. The metallic moments in the paramagnetic state are also very near to the ionic value except in Yb, which exists in a divalent state with a complete 4f shell. This gives rise to a temperature independent susceptibility, which is also observed in the terminal elements, La and Lu. The closeness of the ionic and metallic moments in the paramagnetic state points to the localized nature of the 4f electrons. Fig. 1.1 shows the variation of the calculated and observed paramagnetic moment through the series. Books on magnetism (e.g. CHIKAZUMI (2)) deal with this topic in detail.

In spite of the localized nature of the 4f shell, the majority of the rare earths develop magnetic order at low temperature. The spin arrangement in the ordered state may be determined by neutron diffraction experiments and has been the subject of investigation by the Oak Ridge and other groups (3-13). The accumulated data on the spin structure of the heavy rare earths in their ordered state can be schematically represented as in Fig. 1.2.

The light rare earths have not been explored in as much detail

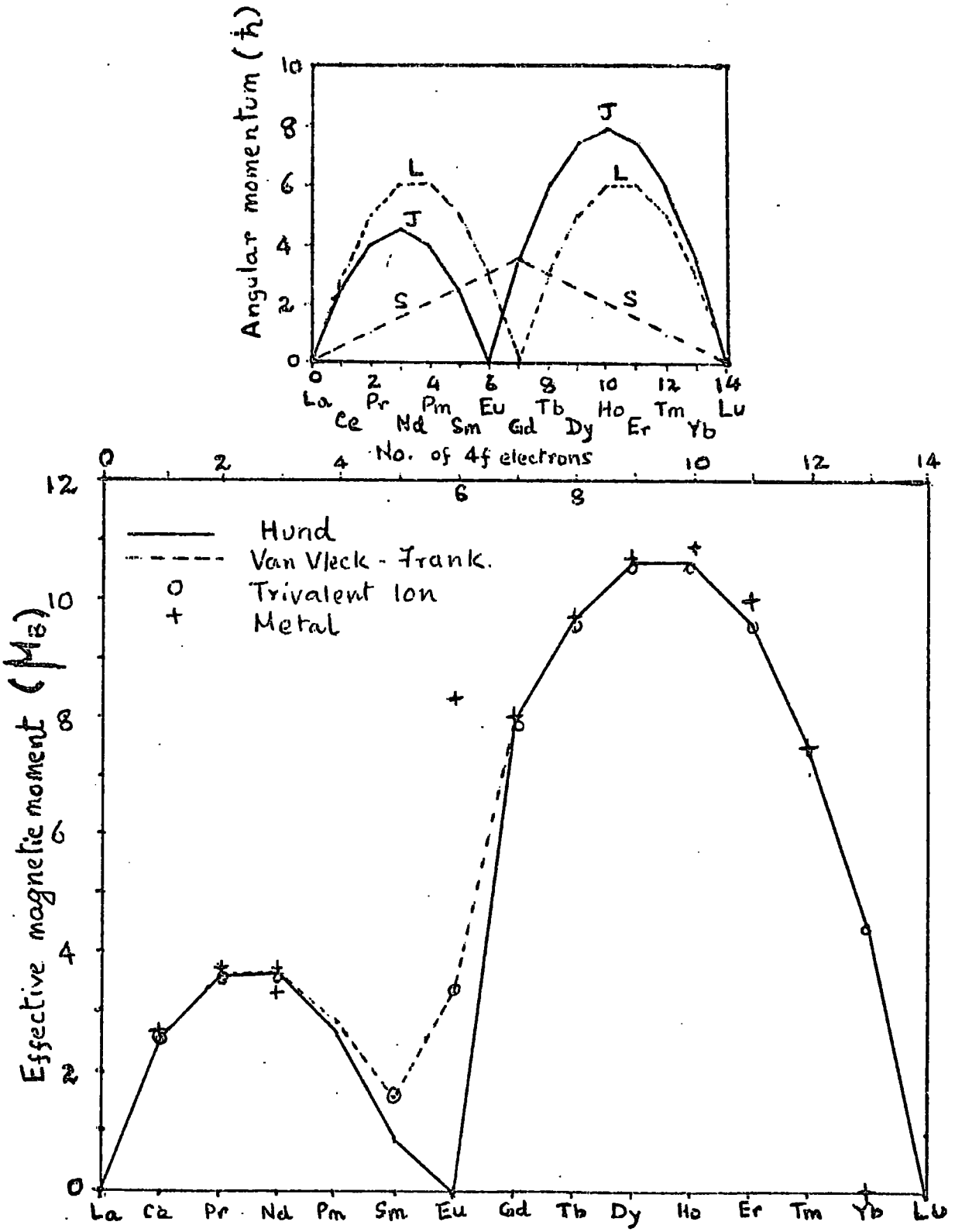
Angular momentum (ħ)
J
L
S
No. of 4f electrons
La Ce Pr Nd Pm Sm Eu Gd Tb Dy Ho Er Tm Yb Lu
Hund
Van Vleck - Frank.
Trivalent Ion
Metal
Effective magnetic moment (μB)

Fig. 1.1

as the heavy ones. The d.h.c.p. phase of Ce shows ordering at ~12.5°K. The ordering is ferrimagnetic in each plane but the overall structure is antiferromagnetic. Single crystal Pr has recently been reported by Lebech and Rainford (14) not to show any ordering whereas earlier experiments on polycrystalline specimens pointed to a structure like that of Nd. In Nd, the moments on the hexagonal sites order at about 19°K and the moments on the cubic sites order at 7.5°K. The spin structures of Pm and Sm have not been reported in the literature yet. Eu orders to a helical antiferromagnetic structure below 91°K.

The heavy rare earths show peculiar magnetic behaviour and the details are complicated. In Gd, the spins align ferromagnetically below 293°K but the easy direction of magnetization is temperature dependent. The single crystal magnetization data of Nigh et al.(15) is in agreement with the neutron diffraction results as well as the data on magnetocrystalline anisotropy published by Corner et al.(16) and Graham (17). The saturation moment is found to be in excess of the gJ value and this is attributed by Liu (18) to conduction electron polarization. The antiferromagnetic ordering between 210°K and 293°K, as postulated by Belov et al.(19) has not been observed in neutron diffraction experiments.

Terbium and Dysprosium show a two step ordering process. Below a characteristic temperature T_N, the moments order ferromagnetically in the basal plane, but the direction changes from one layer to the next by an equal amount giving rise to a screw type spin structure and the material behaves as an antiferromagnet. Below another characteristic temperature Tc, the screw structure, also known as helical or spiral structure, collapses and there is

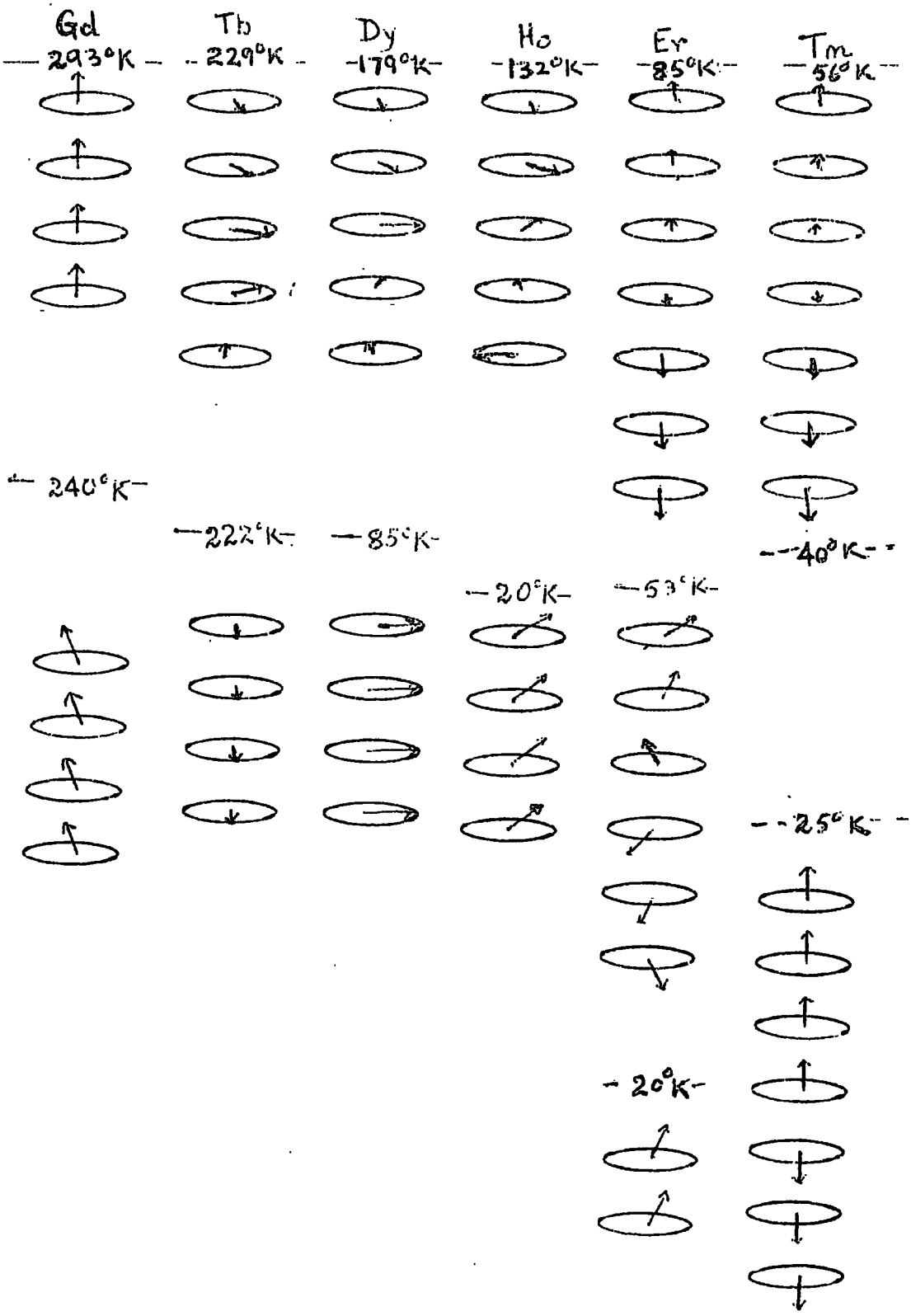
Gd
293°K
Tb
229°K
Dy
179°K
Ho
132°K
Er
85°K
Tm
56°K
240°K
222°K
85°K
20°K
53°K
40°K
25°K
20°K

Fig. 1.2

ferromagnetism with the easy direction in the basal plane. The two characteristic temperatures, T_N and T_C, are known as the Néel and the Curie points respectively. The transition temperatures for Tb are 221°K and 229°K while for Dy they are reported at 179°K and 85°K. The magnetization data of Hegland et al.(20) on Tb and Behrendt et al.(21) on Dy are compatible with the spin structures. Application of a magnetic field above a critical value in the basal plane destroys the helical arrangement and ferromagnetic ordering results. This critical field is a function of temperature. The saturation magnetic moment is in excess of the respective gJ values and the conduction electron polarization is again thought to be the cause.

In Holmium, the helical spin structure is observed between 132°K (T_N) and 20°K (T_C). Below T_C, the moments lie in a cone about the c axis. The magnetization data of Strandburg et al.(22) are in agreement with this structure. Critical field effects are observed as well as an excess moment due to the conduction electron polarization. Recently, Koehler et al.(23) have investigated the spin structure of Ho as a function of temperature and magnetic field in great detail.

Erbium shows a complicated spin structure called by different authors by different names - sinusoidal, linear spin wave type or oscillatory z component structure - in the temperature range 85°K to 53°K. In this arrangement there is no order in the basal plane, while the moment along the c axis varies sinusoidally in magnitude. Below 53°K, Er goes into a quasi-antiphase domain structure. In this arrangement moments order in a helical configuration in the

basal plane but along the c axis there are several spins pointing in one direction followed by an equal number in the opposite direction. There is transformation to a conical arrangement below 20°K. The scheme is in agreement with the single crystal magnetization measurements of Green et al.(24) and high field measurements of Flippen and others (25-27).

Thulium goes into an oscillatory z component structure similar to Erbium below 56°K and after going through a more complicated and as yet unestablished structure between 40°K and 25°K finally forms a quasi antiphase domain structure with a sequence of 4 spins up followed by 3 spins down. The magnetization data of Schieber et al.(28) at 4.2°K and 140 kGauss field points to a decoupling of this 4↑, 3↓ structure.

The high field measurements draw attention to the large anisotropy in these elements and except in the case of Gd, magnetic fields of up to 150 kGauss are not large enough to overcome the anisotropy.

Various electronic properties, e.g. the transport properties, specific heat etc., have been investigated by several workers and comprehensive references are available in the various review articles (29-34) on the rare earths. Table 1.1 lists some of the important parameters for these elements.

1.3. Magnetic Interactions in Rare Earths

The magnetic ordering in rare earths is due to some strong interaction. Because of the localized nature of the 4f electrons, an indirect exchange mechanism has been postulated for the rare earths. The idea was originally proposed by Zener (35) and several

TABLE I

Z	Element	Atomic Weight	Room Temperature Crystal Structure Lattice Spacing in Å	Atomic Radii Å	Density at 20°C gms/c.c	Melting Point °C	Coeff. thermal expansion a_a a_c $10^{-6}/°K$	(High temperature) c poly	T_N	T_c	Sat. $gJ\ \mu_B$	Moment Observed	
21	Sc	44.96	H.C.P. a = 3.308 c = 5.2653	1.64	2.992	1540	9 3 15.2	11.4	-	-			
39	Y	88.92	H.C.P. a = 3.6451 c = 5.7305	1.81	4.478	1510	6.2 19.7	10.8	-	-			
57	La	138.92	D.H.C.P. a = 3.770 c = 12.131	1.87	6.174	920		7.9	-	-			
58	Ce	140.13	F.C.C. a = 5.16	1.81	6.77	795		6.7	12.5°K		2.14		Ferromagnetic in plane but not anti-ferromagnetic
59	Pr	140.92	D.H.C.P. a = 3.6702 c = 11.828	1.82	6.782	935	4.5 11.3	6.8			3.2		No ordering in single crystal
60	Nd	144.27	D.H.C.P. a = 3.6582 c = 11.802	1.82	7.004	1024	6.5 11.7		19°K		3.20		Hexagonal sites order at 19°K and cubic at 75°K.
61	Pm		not known			1080	-	-					
62	Sm	150.35	9 layer Hex a = 3.628 c = 26.230	1.80	7.536	1072	-	-	15°K		0.71		
63	Eu	152.0	B.C.C. a = 4.578	2.04	5.26	826		19.6			0	3	
64	Gd	157.26	H.C.P. a = 3.6315 c = 5.777	1.79	7.895	1312	6.3 13.0	8.9		290°K	7	7.55	
65	Tb	158.93	H.C.P. a = 3.599 c = 5.696	1.77	8.272	1356	9.1 17.9	12.1	<28°K	222°K	9	9.34	
66 66	Dy	162.51	H.C.P. a = 3.5923 c = 5.6545	1.77	8.636	1407	4.7 20.3	9.9	179°K	85°K	10	10.6	
67	Ho	164.94	H.C.P. a = 3.5761 c = 5.6174	1.76	8.803	1461	4.9 18.4	9.5	132°K	20°K	10	10.34	
68	Er	167.27	H.C.P. a = 3.559 c = 5.592	1.75	9.051	1497	7.5 19.5	11.5	85°K	20°K	9	9.0	Quasi antiphase structure between 54° K and 20°K
69	Tm	168.94	H.C.P. a = 3.5372 c = 5.5219	1.74	9.332	1545	7.5 19.7	11.6	56°K	20°K	7.00	7.14	Spin structure uncertain between 40°K + 20°K
70	Yb	173.04	F.C.C. a = 5.481	1.93	6.997	824		30.6			3.00		No order
71	Lu	174.97	H.C.P. a = 3.505 c = 5.549	1.74	9.842	1652	10.2 16.9	12.55	-	-			

review articles deal with the subject. Rudermann and Kittel (36) first used this mechanism for inter nuclear coupling and this has been used for ions in metallic lattices by Kasuya (37) and Yosida (38). It is commonly known as RKKY interaction. The ionic spins are assumed to cause polarization in the conduction electrons which in turn interact with other ionic spins.

In the RKKY interaction, the 4f spins of the rare earth ion set up a conduction electron spin polarization and the polarization couples with the spins of the ions at other sites to produce an effective exchange. Analysis of such a mechanism within the molecular field approximation and free electron model leads to a relation of the form (39)

$$k\Theta = CZ^2 \frac{(g-1)^2 J(J+1)}{V^2 E_f} \sum_{j \neq 0} F(2k_f r_{oj}) \quad ....(1.1)$$

where Θ is the paramagnetic Curie point, k is the Boltzman's constant, C is a constant of proportionality, Z, the number of conduction electron per atom, V, the atomic volume, E_f, the Fermi energy and k_f the Fermi wave vector and F(x) is of the form $\frac{x \cos x - \sin x}{x^4}$. The summation is for atoms at various distances r_{oj} from the atom at r_o. The relationship invcIves the quantity $(g-1)^2 J(J+1)$, which is called the de Gennes function and is physically the square of the projection of S on J.

The RKKY model makes some rather sweeping assumptions and it is rather fortuitous that the experimental observations fit in with the model. The limitations have been discussed by various authors (40-41) and refinements have been made. Nevertheless the simple model is a useful aid to an understanding of the ordering processes

in the rare earths, particularly the heavy ones.

1.4. Intra Rare Earth Alloys

The study of intra rare earth alloys as well as alloys of rare earths with non magnetic diluents, Y and Sc, offers a very wide scope because of the variety in physical properties. The majority of the work on magnetic properties and magnetic structures in these systems has been performed at the Ames, Oak Ridge and I.B.M. laboratories. Experiments have been done on various polycrystalline and single crystal samples.

A considerable amount of data on intra rare earth alloys have been compiled and presented by Rozen and his co-workers (42-44). These are binary systems amongst the heavy rare earths excluding Yb, which does not form a continuous range of solutions. The magnetic ordering follows the same broad pattern as in the elements themselves. The Néel points show a remarkable relation with the average de Gennes function $\bar{G}$. It is found that $T_N \propto \bar{G}^{2/3}$ where

$$\bar{G} = \Sigma c_i G_i \quad \ldots(1.2)$$

c_i being the concentration of the ith component with de Gennes function G_i is followed by many alloys as shown in refs. 42-44. The $^2/_3$rd power law, as this relation is commonly known, is empirical in origin.

1.5. Alloys of Heavy Rare Earths with Yttrium and Scandium

As mentioned before, Y and Sc have similar crystal structure and electron configuration to the heavy rare earths but do not show magnetic ordering, so the study of R-Y and R-Sc systems, where R is a heavy rare earth is of interest in the investigation of the

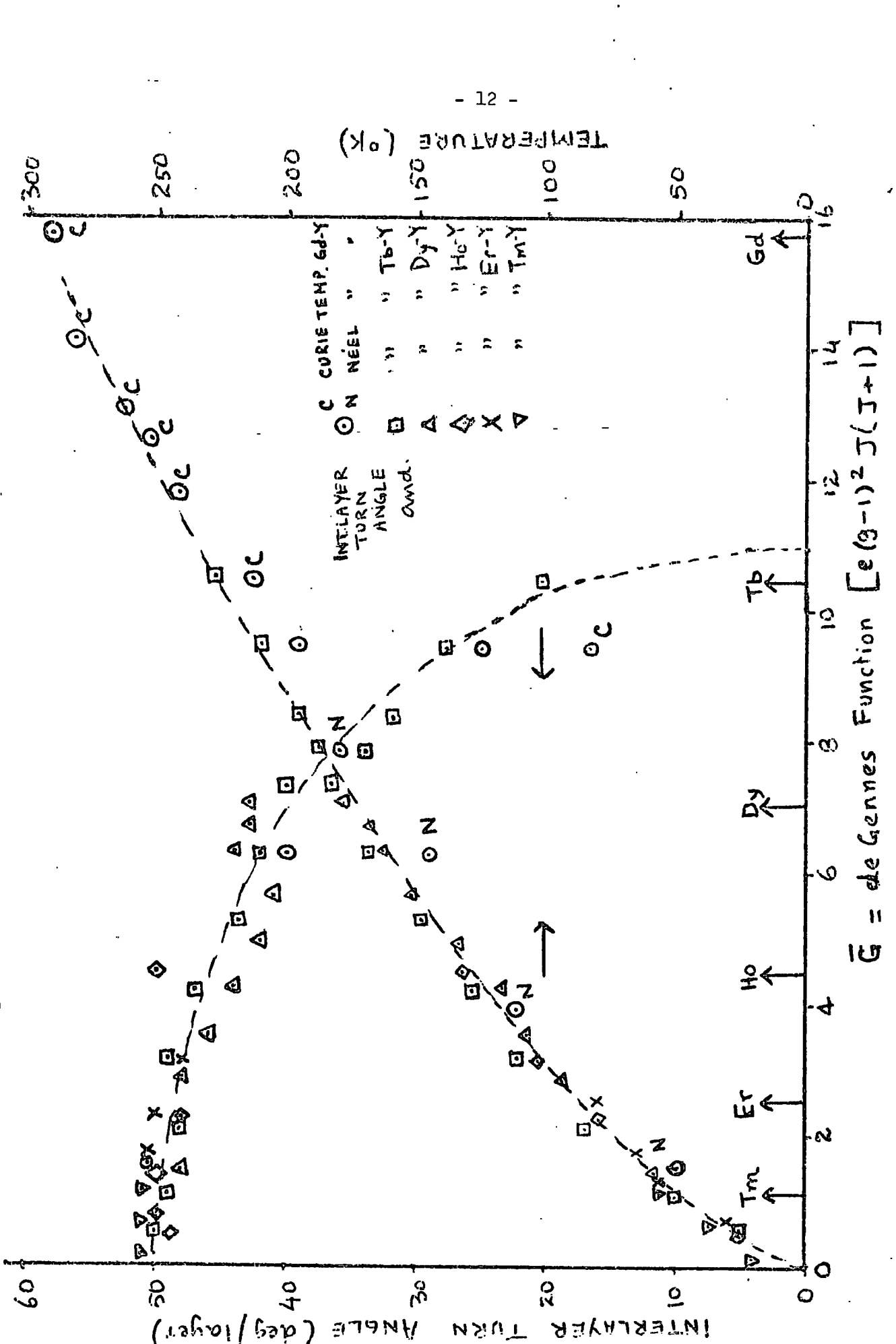
TEMPERATURE (°K)
300
250
200
150
100
50
0
C CURIE TEMP. Gd-Y
N NÉEL " "
" Tb-Y
" Dy-Y
" Ho-Y
" Er-Y
" Tm-Y
INTERLAYER TURN ANGLE cmd.
INTERLAYER TURN ANGLE (deg/layer)
60
50
40
30
20
10
0
Gd
Tb
Dy
Ho
Er
Tm
0
2
4
6
8
10
12
14
16
G = de Gennes Function [e(g-1)² J(J+1)]

Fig. 1.3

ordering processes in the heavy rare earths.

Dilution of heavy rare earths by Y changes the magnetic interaction without much change in the physical size as the lattice parameter of Y is very close to that of Gd. Bulk magnetization(45-47) and neutron diffraction experiments (48) show that dilution with Y stabilises the helical structure at the expense of the collinear structure in the R-Y alloys. The $T_N \propto \bar{G}^{2/3}$ relationship is obeyed and the initial interlayer turn angle (the turn angle between the layers as the system goes into the helical arrangement) is a smooth function of $\bar{G}$ as shown in Fig. 1.3. An examination of the data shows a remarkable independence of the properties of the alloys from the properties of the rare earth constituent. The extrapolation of the available data point to a ferromagnetic structure resulting from a collapse of the helical structure around $\bar{G} = 11.5$. For low $\bar{G}$ values the helical structure stabilises with a limiting interlayer turn angle $\sim 50^{\circ}$.

Nagasawa and Sugawara (49) have reported susceptibility measurements on dilute alloys of the Tb-Y system (low Tb concentration) and the crystal structures of the alloys in the series have been examined over a temperature range $77^{\circ}K$ to $330^{\circ}K$ by Finkel et al.(50). Some high pressure work has been done on the Tb-Y system and some other systems by McWhan et al.(97).

Of the R-Sc alloy systems only Gd-Sc alloys have been investigated magnetically by Nigh et al.(51). Neutron diffraction measurements on Gd-Sc, Tb-Sc, Ho-Sc and Er-Sc alloys have been made at Oak Ridge (51,53). Fig. 1.4(i) and 1.4(ii) summarises the available data on the ordering temperatures and turn angles as functions of $\bar{G}$ and concentration for the different R-Sc alloys. Sc has a smaller

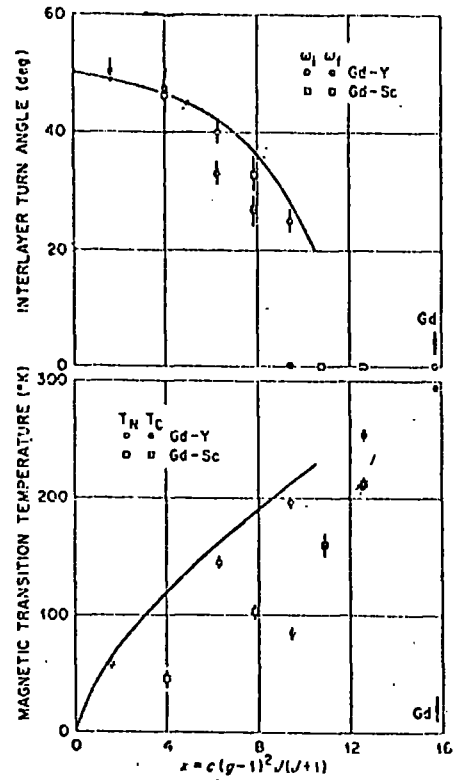
INTERLAYER TURN ANGLE (deg)
60
40
20
0
ω_1 ω_1
Gd-Y
Gd-Sc
Gd
MAGNETIC TRANSITION TEMPERATURE (°K)
300
200
100
0
T_N T_C
Gd-Y
Gd-Sc
Gd
0
4
8
12
16
$x = c(g-1)^2 J(J+1)$

(a)

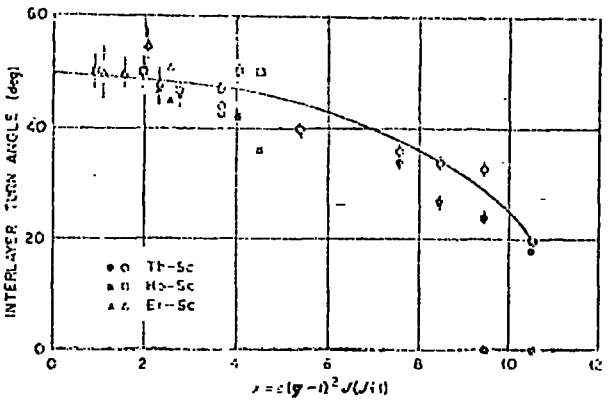
INTERLAYER TURN ANGLE (deg)
60
40
20
0
Tb-Sc
Ho-Sc
Er-Sc
0
2
4
6
8
10
12
$x = c(g-1)^2 J(J+1)$

(b)

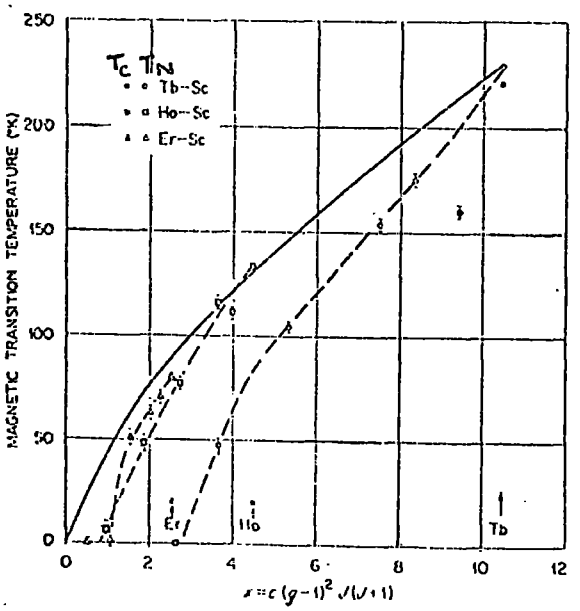
MAGNETIC TRANSITION TEMPERATURE (°K)
250
200
150
100
50
0
T_C T_N
Tb-Sc
Ho-Sc
Er-Sc
Er
Ho
Tb
0
2
4
6
8
10
12
$x = c(g-1)^2 J(J+1)$

(c)

Fig. 1.4

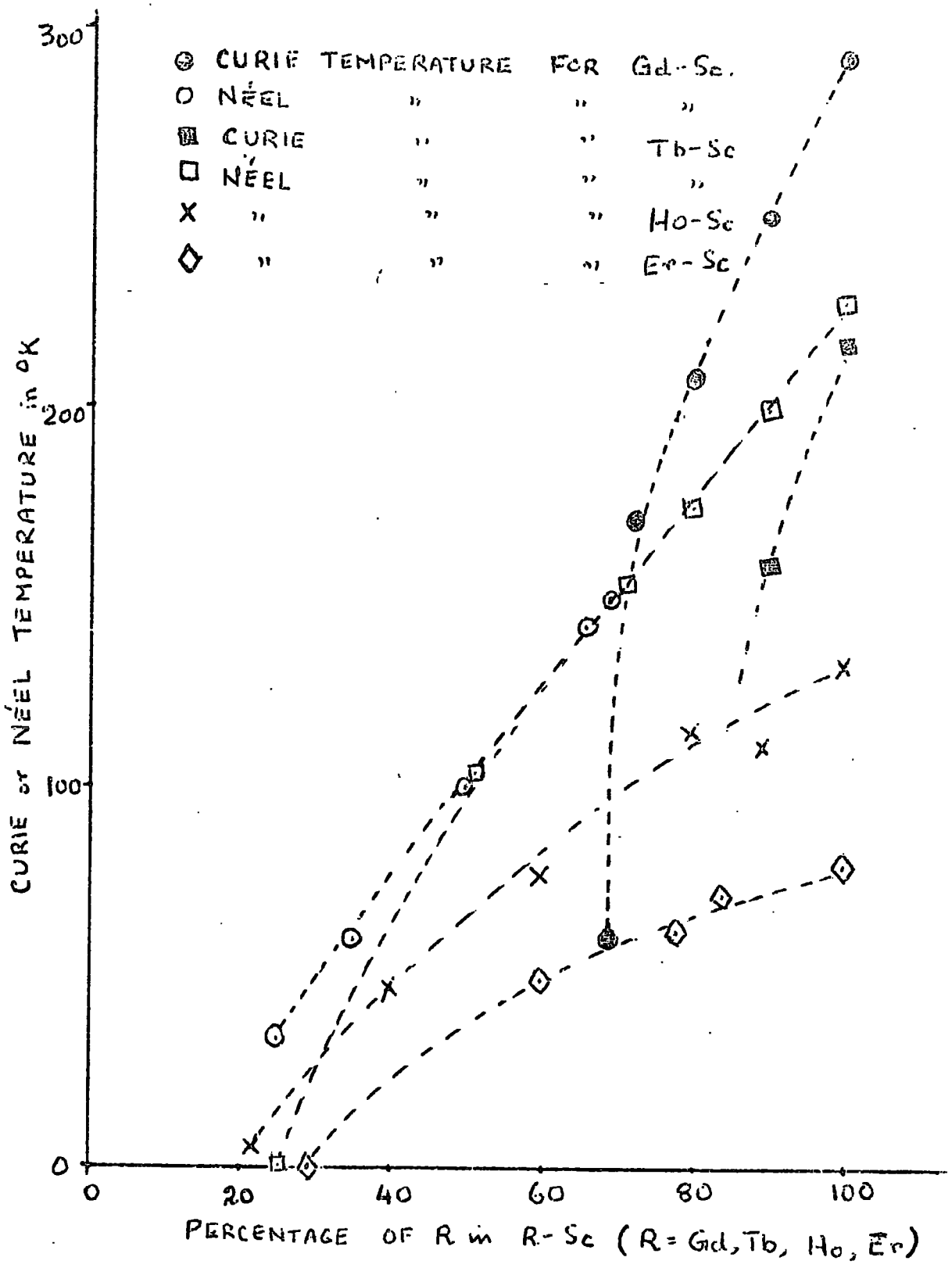
CURIE TEMPERATURE FOR Gd-Sc.
NÉEL " " "
CURIE " " Tb-Sc
NÉEL " " "
" " " Ho-Sc
" " " Er-Sc
CURIE or NÉEL TEMPERATURE in °K
300
200
100
0
0
20
40
60
80
100
PERCENTAGE OF R in R-Sc (R = Gd, Tb, Ho, Er)

Fig. 1.5

atomic size and the alloys in general behave differently to the R-Y alloys. Even for fairly high rare earth concentrations, no ferromagnetic ordering has been observed. The helical antiferromagnetic phase grows at the expense of the ferromagnetic phase but the alloys cease to exhibit the helical structure if the rare earth concentration falls to below about 25% and no ordering is observed.

Wollan (54,55) has discussed the effect of alloying the heavy rare earths with scandium. The smaller size of the scandium, he points out, would have the same sort of effect as bringing the rare earth atoms closer by the application of high pressure. A qualitative agreement has been obtained for the Gd-Sc alloys.

A more detailed investigation of the magnetic ordering of Tb-Sc system is the object of the present investigation.

CHAPTER 2

THEORETICAL BACKGROUND

2.1. Basic Postulates of Ferromagnetism

The behaviour of a ferromagnetic material has been explained on the basis of the interaction of elementary atomic moments with an internal magnetic field. The treatment is amply covered in most books on magnetism (56) and the important features may be summarised in the following way.

Below a characteristic temperature (T_C), known as the Curie Temperature (or point), a ferromagnet exhibits spontaneous magnetization. The temperature dependence of the spontaneous magnetization per gram mole of the substance is obtained by the simultaneous solution of the equations.

$$\frac{M(T)}{M(0)} = B_J(x) \qquad \ldots\ldots \quad (2.1)$$

and

$$\frac{M(T)}{M(0)} = \frac{kT}{N N_W g^2 \mu_B^2 J^2} x \qquad \ldots\ldots \quad (2.2)$$

where $M(T)$ = spontaneous magnetization at temperature T,

$M(0)$ = $Ng \mu_B J$ = spontaneous magnetization at absolute zero

$B_J(x)$ = Brillouin function for total angular momentum J

k = Boltzmann constant

N = Avogadro's Number

N_W = Weiss molecular field constant

g = Landé g factor

and μ_B = Bohr magneton

Above the Curie temperature there is no spontaneous magnetization and the system behaves as a paramagnet obeying the Curie-Weiss relationship at temperatures higher than a few degrees above T_C. The paramagnetic Curie point, obtained by the extrapolation of the

linear region of the $1/\chi$ vs T plot to $1/\chi = 0$, is different from T_C.

The classical molecular field theory explains the experimental observations with reasonable clarity. It does not, however, provide any insight into the origin of the internal magnetic field also known as the Weiss molecular field. The internal field was shown by Heisenberg (57) to be the result of a quantum mechanical exchange interaction. In the Heisenberg formalism, the interaction between two atoms of spins $\underset{\sim}{S}i$ and $\underset{\sim}{S}j$ can be described by a Hamiltonian given by

$$\mathcal{H} = -2\mathcal{J}_{ij}\ \underset{\sim}{S}i \cdot \underset{\sim}{S}j \qquad \ldots\ldots (2.3)$$

For a solid with nearest neighbour exchange only, the Hamiltonian is

$$\mathcal{H} = -2\Sigma_{i,j}\ \mathcal{J}_{ij}\ \underset{\sim}{S}i \cdot \underset{\sim}{S}j \qquad \ldots\ldots (2.4)$$

and the summation is over the nearest neighbours of the i^{th} atom. For a crystal with isotropic interactions, the expression has to be summed up over all atoms and yields

$$\mathcal{H} = -2\mathcal{J}\ \Sigma_{ij}\ \underset{\sim}{S}i \cdot \underset{\sim}{S}j \qquad \ldots\ldots (2.5)$$

In principle, the solution of such a Hamiltonian should lead to the explanation of ferromagnetism. A general solution has not been obtained, but there are special cases where analysis has been made.

The localized moment assumption leading to the Heisenberg formalism is not valid in the case of metals and alloys which are ferromagnetic. Very important results have been obtained on the basis of band theory. The approach of Zener (35) and the consequent extension to RKKY interaction (36-38), which has been discussed briefly in the previous chapter has been used to clarify the rare earth magnetism.

2.2. Basic Postulates of Antiferromagnetism

It is also relevant to discuss briefly the phenomenon of antiferromagnetism. If the exchange integral J in the Heisenberg formulation is negative, the spins will line up antiparallel in the ground state. An antiferromagnet can be classically considered to be made up of two sublattices and the application of the molecular field theory leads to the following conclusions. Above a characteristic temperature called the Néel temperature (T_N), the susceptibility is related to the temperature by

$$\chi = \frac{C}{T + \theta} \qquad \ldots\ldots (2.6)$$

where θ is the paramagnetic Curie point. Below T_N, both sublattices possesses a spontaneous magnetization of equal magnitude. In the absence of any applied magnetic field, the sublattice magnetizations are antiparallel. The magnetic field, in general, will make an arbitrary angle with the spin axis. It is simpler to consider a single crystal to examine the behaviour below T_N. When the magnetic field is parallel to the spin axis, the susceptibility ($\chi_{\parallel}$) is zero at $0^{\circ}K$ and increases to its value at T_N with increasing temperature. For the magnetic field applied perpendicular to the spin axis, the susceptibility ($\chi_{\perp}$) is constant below T_N. For a polycrystalline specimen the susceptibility

$$\chi_p = \frac{1}{3}\chi_{\parallel} + {}^{2}/_{3}\chi_{\perp} \qquad \ldots\ldots (2.7)$$

2.3. Helical Spin Systems

The initial attempt to explain the behaviour of Dysprosium was made by Liu et al.(58) on the basis of sublattice magnetizations. The neutron diffraction experiments of Koehler et al.(10), however,

established the helical spin structure between T_N and T_C for Dysprosium. This was proposed by Enz (59), who considered a long-range interaction covering more than one layer and containing both positive and negative components. The equilibrium between these interactions stabilisesthe helical structure.

The helical spin structure was first postulated for MnO_2 by Yoshimori (60) and was observed in $MnAu_2$ by Herpin et al.(61). The behaviour of a helical spin system in a magnetic field and the effect of anisotropy energy with special reference to the heavy rare earths was discussed by Miwa et al.(62). Nagamiya (63) has recently published a review article on the behaviour of helical spin systems.

The existence of the screw spin system in Tb, Dy and Ho and various rare earth alloys has been reported in great detail. The spins in the basal plane of the h.c.p. structure order ferromagnetically. The spins in the next layer, though parallel to one another, are at an angle to the preceding layer and this is repeated. The interlayer turn angle (θ) can be experimentally determined by neutron diffraction experiments. The simplest experiment is to observe the diffraction pattern for a poly-crystalline sample. Above T_N, the pattern can be indexed on the basis of the various hkℓ reflections compatible with the h.c.p. structure and the lattice spacings. Below T_N, magnetic satellites appear in the diffraction patterns. A pattern typical of the screw or helical spin structure shows a satellite $00\delta^{+}$ about the unscattered direction (origin) and also satellites $00\ell^{\pm}$ about the 00ℓ lines which are displaced from 00ℓ by the same amount as the

displacement of 000^{+} from the origin. $hk\ell^{\pm}$ satellites are also present. From the spacings of the 000^{+} and $00\ell^{\pm}$ satellites, the interlayer turn angle can be calculated. The temperature variation of θ can be studied by observing the positions of the satellites as a function of temperature.

The Heisenberg exchange energy covering the nearest and the next nearest neighbours exchange in the case of a helical spin structure with turn angle θ may be written as

$$E_{ex} = - M_s^2 (J_o + J_1 \cos\theta + J_2 \cos 2\theta) \quad .... (2.8)$$

where J_o is the exchange constant between the spins in a layer

J_1 is the exchange constant between two adjacent planes and

J_2 is the exchange constant for alternate planes and M_s is the spontaneous magnetization. For the stability of such a system the condition

$$\frac{dEx}{d\theta} = 0 \quad ..... (2.9)$$

has to be satisfied. This condition leads to the relation

$$\cos\theta = - \frac{J_1}{4J_2} \quad ..... (2.10)$$

From this relation it follows that the helical structure is stable only when J_1 and J_2 are opposite in nature and also when $J_1 < 4J_2$. If $J_1 > 4J_2$, the interaction between the alternate planes is not strong enough to support the helix and the system collapses to a normal ferromagnet as J_1 is a ferromagnetic exchange constant while J_2 is an antiferromagnetic exchange constant.

2.4. Effect of a Magnetic Field on a Helical Spin System

For an ensemble, as described above, the application of a magnetic field in the basal plane makes the energy take a value E given by the equation

$$E_{ex} = - M_s^2 \left(\mathcal{J}_o + \mathcal{J}_1 \cos \theta + \mathcal{J}_2 \cos 2\theta \right) - M_s H \Sigma \cos \theta \quad \ldots\ldots (2.11)$$

When the magnetic field H reaches a critical value, it is energetically favourable for the system to collapse to a ferromagnetic state. This is manifested as a large increase in the magnetization at a certain value of the magnetic field. Herpin et al.(61) showed that the critical field H_{cr} is given by

$$H_{cr} = - 7.76 M_s \mathcal{J}_2 \sin^4 \theta/2 \quad \ldots\ldots\ldots (2.12)$$

This relation together with (2.10) provides a means for estimating $\mathcal{J}_1$ and $\mathcal{J}_2$. Belov et al.(29) have discussed this in detail for Dy and Ho.

2.5. Anisotropy in Rare Earth Metals and Alloys

In our discussion so far the anisotropy and magnetostrictive energy terms, which are important in case of rare earth metals and alloys, have not been included. Elliot(64) has made the importance of crystal field effects and associated magneto-crystalline anisotropy clear. The electrostatic potential in a hexagonal crystal is of the form

$$V = V_2^o \alpha Y_2^o (J) + V_4^o \beta Y_4^o (J) + V_6^o \gamma Y_6^o (J) + V_6^6 \gamma Y_6^6 (J) \quad \ldots\ldots (2.13)$$

where V_ℓ^m are constants dependent on the structure,

α, β, γ are numerical constants

and Y_l^m (J) are the operator equivalents for the spherical harmonics for the total angular momentum J.

This interaction leads to a large axial and a smaller planar anisotropy and the anisotropy energy has the form

$$W = K_1 \text{Sin}^2 \emptyset + K_2 \text{Sin}^4 \emptyset + K_3 \text{Sin}^6 \emptyset + K_4 \text{Sin}^6 \emptyset \text{Cos } 6\psi \quad \ldots\ldots (2.14)$$

where K_n's are constants and in general functions of magnetic field and temperature, $\emptyset$ and ψ define the direction of magnetization relative to the c-axis and a axis respectively. Experimental determinations of the anisotropy constants for some heavy rare earths have been made (65-67).

2.6. Magnetostriction in Hexagonal Crystals

The expression for the magnetostriction in a hexagonal crystal was derived phenomenologically by Mason (68). Callen and Callen (69-70) formulated a theory of magnetostriction arising from single-ion crystal field effects in cubic crystals and extended it to include two ion interactions and crystals of arbitrary symmetry. They started from a Hamiltonian $\mathcal{H}$ for a system as

$$\mathcal{H} = \mathcal{H}_m + \mathcal{H}_e + \mathcal{H}_{me} + \mathcal{H}_a \quad \ldots\ldots (2.15)$$

where $\mathcal{H}_m$ is the Hamiltonian consisting of isotropic exchange and the Zeeman interaction with an external field, $\mathcal{H}_e$ is the elastic energy associated with homogeneous strain components, $\mathcal{H}_{me}$ is the magnetoelastic interaction, and $\mathcal{H}_a$ is the magnetocrystalline anisotropy. The details of the analysis are avoided but the points important to this investigation retained.

The $\mathcal{H}_{me}$ and $\mathcal{H}_a$ terms are treated as perturbations on the

unperturbed term $\mathcal{H}_m$ and $\mathcal{H}_e$ (which is of the form $\frac{1}{2} C \varepsilon^2$) is treated as an additive term. Clark et al.(71) have used the Callen and Callen formalism for dysprosium and using their symbols, the magnetoelastic interaction Hamiltonian can be written down as

$$\mathcal{H}_{me} = - \sum_{\mu,j} \sum_{\ell} B_j^{\mu,\ell} \sum_i \varepsilon_i^{\mu,j} \sum_f \kappa_i^{\mu,\ell}(S_f) - \sum_{\mu,j} \sum_{\ell,i} \varepsilon_i^{\mu,j} \sum_{f,g} D_j^{\mu,\ell}(f,g) \kappa_i^{\mu,\ell}(S_f,S_g) \quad \ldots\ldots (2.16)$$

In this expression $B_j^{\mu,\ell}$ and $D_j^{\mu,\ell}$ are one-ion and two-ion temperature independent coupling constants, $\varepsilon_i^{\mu,j}$ are irreducible strains, $\kappa_i^{\mu,\ell}(S_f)$ and $\kappa_i^{\mu,\ell}(S_f,S_g)$ are spin functions (one-ion and two-ion) as described in ref. 71. For hexagonal symmetry the symmetry strains are related to the Cartesian strains by

$$\varepsilon^{a,1} = \varepsilon_{xx} + \varepsilon_{yy} + \varepsilon_{zz}$$

$$\varepsilon^{a,2} = \varepsilon_{zz} - \frac{1}{3} \varepsilon^{a,1}$$

$$\varepsilon_1^{\gamma} = \frac{1}{2} (\varepsilon_{xx} - \varepsilon_{yy})$$

$$\varepsilon_2^{\gamma} = \varepsilon_{xy}$$

$$\varepsilon_1^{\varepsilon} = \varepsilon_{yz} \quad \text{and} \quad \varepsilon_z^{\varepsilon} = \varepsilon_{zz} \quad \ldots\ldots (2.17)$$

The expression for magnetostriction is obtained by minimizing the free energy w.r.t. the strains and tranforming the hexagonal strains to Cartesians strains and is given by

$$\lambda = \sum_{i,j} \epsilon_{ij} \beta_i \beta_j$$

$$= \lambda_1^{\alpha,o} (\beta_x^2 + \beta_y^2) + \lambda_2^{\alpha,o} \beta_z^2 + \lambda_1^{\alpha,2} (\beta_x^2 + \beta_y^2)(\alpha_z^2 - \tfrac{1}{3})$$

$$+ \lambda_2^{\alpha,2} \beta_z^2 (\alpha_z^2 - \tfrac{1}{3}) + \lambda_1^{\gamma,2} \left\{ \tfrac{1}{2} (\beta_x^2 - \beta_y^2)(\alpha_x^2 - \alpha_y^2) \right.$$

$$\left. + 2 \beta_x \beta_y \alpha_x \alpha_y \right\} + 2 \lambda^{\epsilon,2} (\beta_x \alpha_x + \beta_y \alpha_y) \beta_z \alpha_z \quad \ldots \quad (2.18)$$

where α_x, α_y and α_z are the direction cosines of the magnetization and β_x, β_y and β_z are the direction cosines for the direction of measurement. The coefficients in (2.18) are explicitly given by

$$\lambda_1^{\alpha,o} = \sum_{f,g} \left[-\tfrac{1}{3} \tilde{D}_1^{\alpha,o}(f,g) - \tfrac{1}{2} \tilde{D}_2^{\alpha,o}(f,g) \right] \langle S_f . S_g \rangle ,$$

$$\lambda_2^{\alpha,o} = \sum_{f,g} \left[\tilde{D}_1^{\alpha,o}(f,g) + \tilde{D}_2^{\alpha,o}(f,g) \right] \langle S_f . S_g \rangle ,$$

$$\lambda_1^{\alpha,2} = \left[\tfrac{1}{3} \tilde{B}_1^{\alpha,2} - \tfrac{1}{2} \tilde{B}_2^{\alpha,2} \right] \langle (S_f^\zeta)^2 - \tfrac{1}{3} S(S+1) \rangle$$

$$+ \sum_{f,g} \left[\tfrac{1}{3} \tilde{D}_1^{\alpha,2}(f,g) - \tfrac{1}{2} \tilde{D}_2^{\alpha,2}(f,g) \right]$$

$$\times \langle S_f^\zeta S_g^\zeta - \tfrac{1}{3} S_f . S_g \rangle ,$$

$$\lambda_2^{\alpha,2} = \left[\tfrac{1}{3} \tilde{B}_1^{\alpha,2} + \tilde{B}_2^{\alpha,2} \right] \langle (S_f^\zeta)^2 - \tfrac{1}{3} S(S+1) \rangle \quad \ldots (2.19)$$

$$+ \sum_{f,g} \left[\tfrac{1}{3} \tilde{D}_1^{\alpha,2}(f,g) + \tilde{D}_2^{\alpha,2}(f,g) \right] \times \langle S_f^\zeta S_g^\zeta - \tfrac{1}{3} S_f . S_g \rangle ,$$

$$\lambda^{\gamma,2} = \tilde{B}^{\gamma,2} \langle (S_f^\zeta)^2 - \tfrac{1}{3} S(S+1) \rangle + \sum_{f,g} \tilde{D}^{\gamma,2}(f,g) \langle S_f^\zeta S_g^\zeta - \tfrac{1}{3} S_f . S_g \rangle ,$$

$$\lambda^{\epsilon,2} = \tilde{B}^{\epsilon,2} \langle (S_f^\zeta)^2 - \tfrac{1}{3} S(S+1) \rangle + \sum_{f,g} \tilde{D}^{\epsilon,2}(f,g) \langle S_f^\zeta S_g^\zeta - \tfrac{1}{3} S_f . S_g \rangle$$

These expressions contain $\tilde{B}$ and $\tilde{D}$ terms which are the B and D terms discussed before with symmetry elastic constants absorbed into them. The symmetry elastic constants are defined by

$$c_1^{\alpha} = \frac{1}{9}(2c_{11} + 2c_{12} + 4c_{13} + c_{33})$$

$$c_2^{\alpha} = \frac{1}{2}(c_{11} + c_{12} - 4c_{13} + 2c_{33})$$

$$c_{12}^{\alpha} = \frac{1}{3}(-c_{11} - c_{12} + c_{13} + c_{33})$$

$$c^{\gamma} = 2(c_{11}-c_{12}) \text{ and } c^{\varepsilon} = 4c_{44} \qquad \ldots. (2.20)$$

relative to the Cartesian constants. The equilibrium energy of magnetostriction can be worked out from the equilibrium strains and leads to the value (ref. 33)

$$E_{ms} = -\frac{1}{8} C^{\gamma}(\lambda^{\gamma,2})^2 \qquad \ldots.(2.21)$$

Experimental evidence in dysprosium has shown that the $\lambda^{\gamma,2}$ coefficient fits single-ion behaviour indicating either $D^{\gamma,2} \ll B^{\gamma,2}$ or the one-ion and two-ion dependences are very similar. Single-ion theory predicts a temperature dependence of $\lambda^{\gamma,2}$ according to

$$\lambda^{\gamma,2}(T) = \lambda^{\gamma,2}(0)\, \hat{I}_{5/2}[\mathcal{L}^{-1}(\sigma)]$$

where $\lambda^{\gamma,2}(0)$ is the value at T = 0 and

$$\hat{I}_{5/2}(X) = \frac{I_{5/2}(X)}{I_{\frac{1}{2}}(X)} \qquad \ldots. (2.22)$$

$I_n(X)$ being the hyperbolic Bessel function of order n. $\mathcal{L}^{-1}(\sigma)$ is the inverse Langevin function of the reduced magnetization at any temperature T. The values of these special functions can be

obtained from 'The Handbook of Mathematical Functions' (72)

An extension of the changes in energies of a system from the helical to the ferromagnetic structure as outlined in eqns. 2.11 and 2.12 along the phenomenological ideas of Elliot (64) allows one to write down an equality of the form.

$$E_{helical} = E_{ferromagnetic} + E_{ms} + E_{anisotropy} \quad ..(2.23)$$

for the transition. It is possible to estimate the difference of energy $E_{ferromagnetic} \sim E_{helical}$ by writing the different components out explicitly. Feron et al(67) have discussed this in detail and the temperature variation of this difference, which has been called the 'driving energy' by Cooper(33) can be investigated. Cooper's estimates for this 'driving energy' shows remarkable correlations with the magnetostrictive energy and the analysis of Feron et al.(67) also shows good agreement.

CHAPTER 3

EXPERIMENTAL DETAILS

3.1 Description of the Single Crystals of Terbium-Scandium Alloy

The single crystals of Terbium-Scandium alloys used in this study were produced by Metals Research Ltd. The starting materials in the case of all the alloys were Terbium and Scandium of best available purity. 2N8 Terbium and 3N5 Scandium were obtained from Rare Earth Products Ltd. Trials with materials of less purity did not produce grain growth in alloys. The alloys of different compositions were prepared by cold crucible casting under high purity Argon atmosphere using water cooled copper boats.

Zone melting techniques using induction heating did not produce any large grains. For each alloy, the castings in the form of rods were annealed at about 1300°C and grains of useful size were obtained. Single crystal discs were cut from these ingots by spark machining. Single crystals of the following specifications and details were obtained:-

TABLE 3.1

Nominal Composition	Disc orientation Plane of disc contains	Diameter mm	Thickness mm
$Tb_{0.9}$ $Sc_{0.1}$	basal plane	4.97±0.05	1.16±0.02
	b and c axes	5.10±0.05	0.91±0.02
$Tb_{0.8}$ $Sc_{0.2}$	basal plane	5.24±0.05	0.64±0.02
	a and c axes	5.23±0.05	1.18±0.03
$Tb_{0.7}$ $Sc_{0.3}$	basal plane	5.15±0.05	1.03±0.02

The offcuts from the ingots were used for the determination of exact composition, lattice parameter measurements and density determination.

3.1(b) Preparation of Polycrystalline Specimens

The polycrystalline materials used in this study were prepared by arc melting appropriate quantities of Terbium and Scandium obtained from Koch-light Laboratories in an atmosphere of pure argon using a non-consumable Tungsten electrode. The alloys were remelted several times to ensure homogeneity. Loss of weight during preparation was negligible indicating that the composition of the alloys obtained were very near to the desired value. The arc melted buttons were annealed for a period of 7 days at 700°c under a vacuum of about 10^{-4} torr.

3.2 X-ray Examination

The single crystals were first examined for their quality and orientation by standard back reflection Laue photographs. The back reflection photographs show a spread in the observed spots indicating a spread due to deviations from the ideal structure. This coupled with the departure from the orientations listed in Table 3.1 amounts to a $\pm 1^{\circ}$ to $\pm 2^{\circ}$ deviation from those mentioned in the Table.

The surfaces for X-ray examination were prepared in the following manner. After polishing with fine grade emery paper (4/0), an etching solution containing 50% concentrated Nitric Acid and 50% glacial Acetic Acid was used. The etching solution was removed by washing the discs in water free Acetone. To examine the surface under a microscope a chemical etching technique due

to Roman (73) was used. A solution containing

	20ml	Lactic Acid
	5ml	Phosphoric Acid
	10ml	Acetic Acid
	1ml	Sulphuric Acid
and	15ml	Nitric Acid

was used to etch the surface after polishing with emery paper and diamond paste. The etching solution was applied with a swab for about 10 seconds and the specimen washed with Ethyl Alcohol. The surfaces, thus prepared, were found to contain very small quantites of a second phase as inclusions most likely to be oxides.

The single crystal discs had to be oriented in various directions for the measurement of directional properties. They were mounted on a goniometer head in a Philips X-ray set. A special attachment was used to facilitate the removal of the discs from the gonimeter to the cryostat preserving the information about the directions. The single crystal disc was stuck onto a specimen holder with 'Durofix' adhesive. The specimen holder had a tapped hole and could be screwed on to a cylindrical brass tube with a thread to take the specimen holder. A brass block attachment was used to hold the cylindrical brass tube in position on the goniometer head. The alignment of the brass block was checked by replacing the cylindrical tube by another one of the same diameter with a hole running down the axis. When aligned properly the pencil of X-radiation went through the hole and the disc face was perpendicular to the direction of the pencil.

Back reflection photographs were used in the usual way to determine the orientation. The specimen holder was aligned so that one of the major axes in the disc was parallel to the base of the

goniometer. In this part of the investigation it was found that stereographic projection for various directions of the incident beam was necessary. As detailed information was not available in any publication a simple computer programme was used to calculate the various interplanar angles in the hexagonal close packed (h.c.p.) structure for an appropriate $^{c}/_{a}$ ratio. These angles were used to plot steographic projections and the Lane patterns were analysed by the usual techniques and the crystal axes identified. Koepke and Scott(74) have published a report on the preparation of stereographic projections for h.c.p. structure. Appendix 1 shows stereographs obtained for the basal plane, ac and bc h.c.p. crystals for $^{c}/_{a} = 1.58$.

3.3. Determinations of Composition of Alloys

The offcuts from the single crystals produced by Metals Research Ltd., were used to establish the composition of the alloys accurately. The nominal compositions were known and several techniques were tried to obtain a better estimate.

An X-ray fluorescence spectrometer in the Geology Department of Durham University was used to compare the intensities of the characteristic emission lines in the alloys with the intensities in pure Terbium. The technique was not very successful in establishing the composition to the desired accuracy but was useful in checking the homogeneity of the specimen and the presence of impurities. The emission from a piece of alloy was checked as it was scanned along the surface. The count rate was reasonably uniform indicating a good homogeneity. The possible existence of impurities such as other rare earths and crucible material was investigated. No evidence of any crucible material was found

even at the most sensitive setting of the instrument.

The method, however, was not capable of estimating the compositions accurately enough for the following reasons. The peaks from the Terbium emission were asymmetric. The probable cause was a non-uniform background and possible presence of very small quantities of other rare earths with peaks very near the Terbium peaks. Also, the correction factors for shielding effects are not precisely known. The estimate of composition was only certain to $\pm$0.5% in the alloy.

A better estimate of the composition was obtained using atomic absorption analysis facilities at International Research and Development laboratories in Newcastle-upon-Tyne. The absorption spectra from solutions prepared by dissolving known amounts of the alloys were compared with standard specimens, and the scandium content established. Spectrographic examinations revealed the presence of iron in small quantities. This was probably added during specimen preparation. The scandium content could be established to $\pm$0.1% and Terbium was supposed to make up the rest. No estimate of the oxygen and other gaseous impurities could be obtained and as such cannot be quoted. It is probably correct to assume that the impurity level was the same as in the parent materials.

3.4. Lattice Parameter Measurements

The offcuts from ingots from which the single crystals were cut and filings from the arc melted buttons were used to measure room temperature lattice parameters. The filing was done in an argon atmosphere in a glove box to minimise the effect of

oxidation. Standard Debye-Scherrer powder diffraction methods were used with CoK_α and CrK_α radiation.

The lattice parameters were obtained by indexing the diffraction pattern with the help of a Bunn chart and then applying the procedure of Cohen(75) to treat systematic errors and obtain the 'a' and 'c' parameters.

3.5. Density Determination

The density determination was done by simple hydrostatic method. The density of the specimen was determined by measuring its loss of weight in monobromobenzene. The liquid chosen was obtainable in water free condition and did not have any chemical reaction with the alloys. Knowing the density of monobromobenzene, the density of the alloys w.r.t. water were calculated.

3.6. Thermal Expansion and Magnetostriction Measurements

(a) Choice of Strain Gauge

Thermal expansion and magnetostriction were measured using strain gauge techniques. The choice of the gauge used was governed by the physical consideration of the size of the specimens, the temperature range of operation, the suitability of adhesives and the effect of magnetic field. Initial tests were made using Budd foil gauges and the recommended two component adhesive. The adhesive was found to be prone to breakdown with temperature cycling and the gauges did not give reproducible results. This was most likely due to the variation in the quality of bonding at different temperatures.

Tests were made with Kyowa strain gauges with the compatible

two-component epoxy adhesive. The KF-1-C 3 gauge with EP-18 adhesive was used in the preliminary studies and produced satisfactory results. These strain gauges were of foil type of 1mm active length, 120 ohms nominal resistance and of gauge factor approximately 2. The gauge backing was trimmed to a size suitable for sticking on a 4.5mm diameter disc. This did not produce any deterioration in performance of these gauges.

(b) Fixing of Gauges

The discs were aligned, as discussed before, and the goniometer assembly was then transferred under a travelling microscope. The cross-wires of the microscope were aligned so as to be in the directions of the principal axes of the disc. The goniometer was held in a fixed position under the microscope by a stand and clamp arrangement. The surface of the specimen was cleaned with trichloroethylene and the adhesive applied. The gauge was positioned on the surface in the desired orientation. The markings on the gauge backing showing the direction of the grid were aligned w.r.t. the cross wires of the microscope. The adhesive was cured at room temperature ($\sim 20^{\circ}C$) for 24 hrs. while the gauge was held under pressure. A pressure of 10 p.s.i. was applied by putting weights on the gauge.

(c) Alignment of Gauges

The smallness of the gauge, the need to transfer the goniometer from the X-ray set to under the microscope and the fact that the width of the grids and the two markings on the gauge were almost of the same size as the cross wires on the microscope reduced the accuracy of the orientation of the gauges

relative to the axes of the crystals. A combination of all the limitations involved will put a reasonable estimate of the error in the gauge orientation and the crystal axes in the $\pm$3-4 degrees range.

(d) Comparator Gauge

The gauge resistance and the insulation to the specimen were checked before transferring the disc into the cryostat for measurements. A fused silica disc was used to mount another strain gauge to be used as a comparator gauge. Fused silica was chosen as the material to support this gauge, also known as a 'dummy gauge', because it has a very small thermal expansion coefficient and a comparison of the gauge stuck on any material with the dummy gauge should reveal the behaviour of the material under examinations.

(e) Calibration of Gauges

The reistance of a strain gauge changes when it expands or contracts and if R and L denote the resistance and length and

ΔR and ΔL, the change in R and L, the ratio

$$\frac{\Delta R/R}{\Delta L/L} = K \qquad \ldots\ldots (3.1)$$

is called the 'gauge factor'. For most of the gauges in common use K has a value around 2. As calculated by Biermasz and Hockstra (76) it can be shown that

$$K = 2 + (C - 1)(1 - 2\sigma) \qquad \ldots\ldots (3.2)$$

where C is a constant independent of the elastic strain and σ is the Poisson's ratio for the gauge material. The second part of the expression provides the deviation from the value of 2.

The gauge factor K varies with temperature. The variation

can be experimentally investigated using an apparatus devised by McClintock(78). Several investigators have looked into the temperature variation of K for different gauges. The results show that the gauge factor is capable of a change from a few per cent to 50% of its room temperature value in a temperature range of about 300 degrees. The KF-1-C3 gauges were tested using an arrangement similar to that of McClintock to check the temperature variation of K. The value of K at 77°K in some of these gauges varied by up to 5% of its room temperature value in some cases. A majority of the gauges, however, showed a variation at 77°K of about 3% of their room temperature value. The testing being destructive, it was not possible to determine this variation in the gauges used for the actual experiments.

To check the accuracy of the value of $\Delta L/L$ measured with a gauge in the experiments, measurements were made on copper. A copper disc cut from 5N pure material was used and the values of $\Delta L/L$ between 77°K and 300°K were compared with those of Nix and McNair (77). It was found that the strains obtained from the gauges were lower than the values of Nix and McNair by 4% to 8%. This difference (average of about 6%) was due to the combination of the effect due to the temperature variation of K and the effect of the layer of adhesive between the specimen and the gauge. The layer of adhesive does not transmit the true strain to the gauge because of its finite thickness and appreciable elasticity.

The specimen in its mount and the dummy gauge on fused silica were fixed in close proximity to one another inside the same enclosure. This placed both the gauges in very similar environment

and the difference in behaviour between the two gauges should result from the alloy under investigation. To verify this assumption an arrangement where the gauge on the specimen is replaced by a gauge on a fused silica disc was used. The differential thermal strain was measured between 77°K and 300°K and was found to be 2 orders of magnitude smaller than the strains due to the specimens under investigation. The effect of magnetic field on the gauges was also investigated. Between 200°K and 300°K, the effect is very small but increases at lower temperatures. At 77°K, the transverse magnetostrain due to the pair of gauges was found to be $\sim 10^{-5}$ while the longitudinal strain was $\sim 5 \times 10^{-5}$.

(f) Cryostat and Electromagnet

The specimen with its attached gauge and the dummy gauge on fused silica were fixed inside an enclosure as shown in Fig. 3.1. The whole assembly was attached to a rigid head with arrangement for suspending the dewars. The specimen chamber could be evacuated and filled with Helium gas for heat exchange. The inner space was then evacuated to any desired pressure up to the limit of the rotary pump. The evacuation provided control on the rate of warming up. Under rotary pump vacuum ($\sim$0.1 mm of Hg) the initial warming up rate was 3°K min and the time taken to cover from 77°K to room temperature was about 4 hrs.

The temperature of the specimen was measured by a copper-constantan thermocouple. One junction of the thermocouple was soldered onto the brass specimen holder and was in good thermal contact with it. It was about 2mm. away from the specimen. The reference junction was held at liquid Nitrogen temperature. The

thermo-e.m.f. was measured with a Pye portable potentiometer in conjunction with an external Scalamp galvanometer. The thermocouple, constructed from "high conductivity" copper and "thermocouple" constantan, gave the same e.m.f. at different fixed points as in the British Standard Tables. Between liquid Nitrogen and the room temperature, the temperature of the specimen could be determined within $\pm\frac{1}{2}^{o}$.

Some measurements were also made between $77^{o}K$ and $4.2^{o}K$. The liquid Helium temperature was attained by standard double dewar techniques. In this case, of course, the accuracy of the temperature determination was lower. This thermocouple has very low thermo-power near liquid Helium temperature and as such the temperature measurement was accurate to within about $3^{o}K$. The gauge behaviour was also erratic at low temperatures, particularly below about $30^{o}K$.

The magnetic field for magnetostriction measurement was provided by an electromagnet. This has been described in detail by Roe (78). The electromagnet was made up of two coils in series. Each of the coil cases had resin insulated copper strip wound about a 10cm diameter soft iron core in 34 layers, with 17 turns per layer. Tufnol spacers provided space for cooling water flow between the layers. The soft iron cores acted as pole pieces and the separation was 4.84 cm. The soft iron cores were mounted on a base which could be rotated about the axis of the magnet and the whole assembly was on a rail and could be moved in and out of its location. The magnet was cooled by distilled water circulated by a pump. This was a closed system, the distilled water being cooled by passing it through a multiple tube heat exchanger with continuously flowing mains water. The magnet had

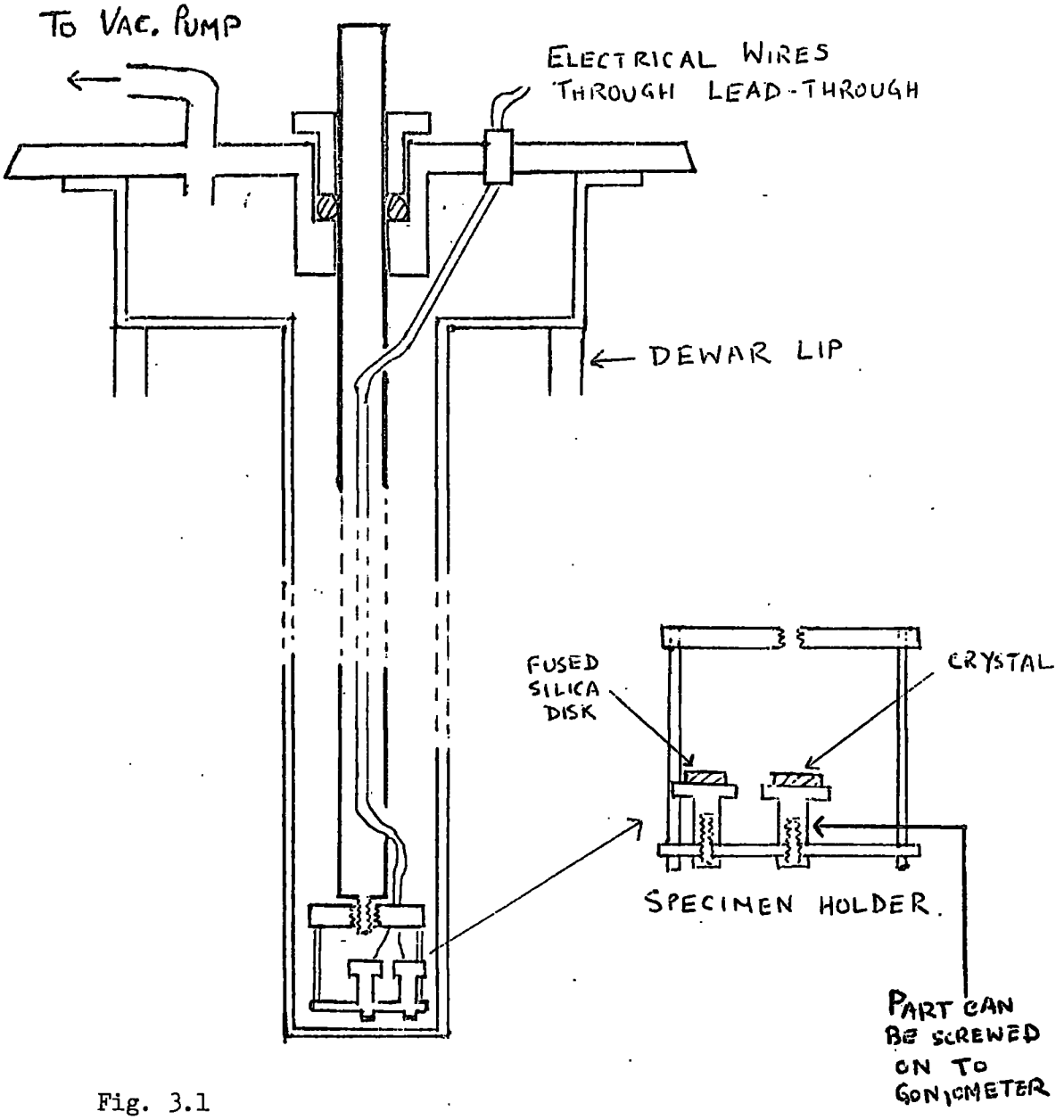
TO VAC. PUMP
ELECTRICAL WIRES THROUGH LEAD-THROUGH
DEWAR LIP
FUSED SILICA DISK
CRYSTAL
SPECIMEN HOLDER
PART CAN BE SCREWED ON TO GONIOMETER

Fig. 3.1

a resistance of just over 1Ω and the current was supplied by a 50kW, 200 amps D.C. supply. The ripple in the voltage output did not have any serious effect on the measurement.

The space available between the pole pieces was not enough to accommodate a double dewar system for work below 77°K, so all the magnetostriction measurements were limited to liquid Nitrogen temperature and above. The magnetic field as a function of the current was measured with a Hall probe. It was found to be uniform within $\pm\frac{1}{2}\%$ over a volume of about $3\,cm^3$ and this was sufficient for the requirements of the experiment.

The specimen was centred in the magnetic field by using a cathetometer. The magnet could be rotated through 360° and alignment in two perpendicular directions as well as adjustment of height placed the specimen in the middle of the field.

The deformation of the specimen (i.e. the strain $\Delta L/L$) was measured by measuring $\Delta R/R$ for the strain gauge. This variation in resistance can be measured by using either an a.c. or a d.c. arrangement. In view of the fact that the specimen was magnetic in certain circumstances, the d.c. method was preferred. The two strain gauges (active and passive) made up two arms of a Wheatstone bridge network. The electrical leads from the gauges were brought out of the cryostat using conventional vacuum lead throughs. Two wire-wound resistors of 120Ω made up the ratio arms of the bridge. A 1.2Ω sliding resistor was used between the 120Ω resistors to provide for matching slight difference in the resistances of different gauges. Two 100kΩ helipots were used in parallel with the gauges. At

room temperature the helipots were set at the same value. The sliding resistor was adjusted to give a null reading in the output.

The bridge was energised by a Mallory mercury cell and the current was adjusted by a potentiometer and monitored by a milliammeter. The output of the bridge was amplified by a Pye photoelectric galvanometer amplifier. Fig. 3.2. shows the circuit details for the bridge.

The current through the gauges was kept at 5ma. Though the gauges are capable of handling higher currents according to the specification, it was found that there were instabilities at higher currents. This was due to inhomogeneous heating in the gauges; operation at 5ma gave stable and reproducible results.

(g) Measurement of Strain

The change in the length of the active gauge due to magnetostriction or thermal expansion changed the resistance of the gauge. The helipot in parallel with the active gauge or the other one was changed to bring the output back to zero. The reading on the helipot required to restore the balance in the bridge can be used to obtain the strain $\Delta L/L$ directly through the relation.

$$\Delta L/L = S/K \quad \frac{R - R'}{R' R} \qquad \ldots\ldots \quad (3.2)$$

where S = gauge resistance,

K = gauge factor,

R = initial helipot reading in ohms

and R' = final helipot reading

For a typical set of data if $S = 120\Omega$

$K = 2$ $R = 90 \times 10^{3}\Omega$

and $R' = 60 \times 10^{3}\Omega$, then $\frac{\Delta L}{L} = 3.33 \times 10^{-4}$

For the circuit used with the galvanometer amplifier and Scalamp galvanometer a strain of 5×10^{-7} could be detected.

The problem of thermal e.m.f's was faced during the course of these experiments. Even with careful matching of the lead wires to the gauges, thermal e.m.f's could not be eliminated completely. A multiway switch was used to sample the thermal e.m.f. detector at the Scalamp galvanometer, as well as to monitor the drift of the galvanometer amplifier. The switch was also used to energise the bridge and reverse the direction of current through the bridge. A simple method was tried to overcome the thermal e.m.f. A small e.m.f. was fed on to the amplifier input in opposition to the thermal e.m.f. to balance it out. The small e.m.f. was delivered from a copper-constantan thermocouple maintained between $77^{\circ}K$ and $273^{\circ}K$ with a suitable potential divider. The thermal e.m.f. at its maximum was equivalent to a pseudo-strain of 10^{-5} at the gauge temperature of $77^{\circ}K$. There was no observable thermal effect above a cryostat temperature of about $150^{\circ}K$.

As discussed before, the accuracy of the strains measured in these experiments was checked by comparing the result against copper. The strain measured by this system was always less than that obtained by interferometric data by $(5 \pm 2)\%$ between $77^{\circ}K$ and room temperature, so the experimental method provided a means of measuring the deformation with a high point to point reproducibility and relative accuracy, but low absolute accuracy. The comparison against the copper data is shown in Fig. 3.3.

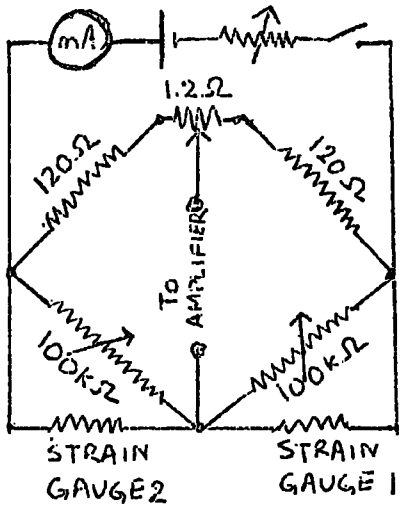

BRIDGE

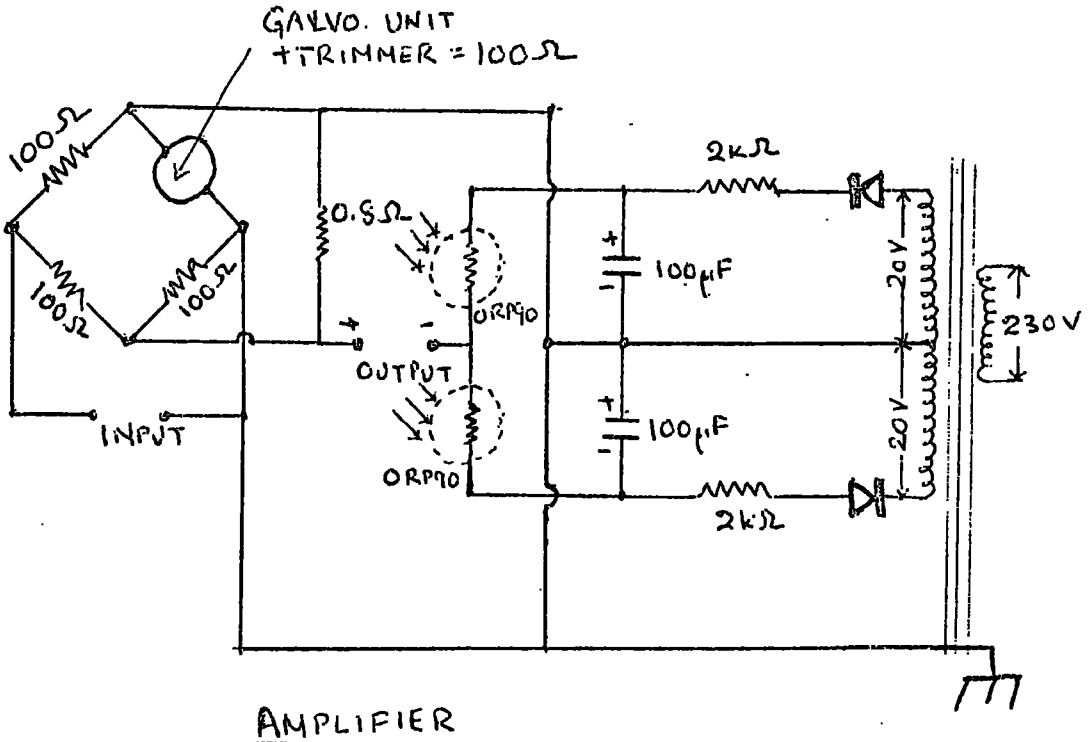

AMPLIFIER

Fig. 3.2

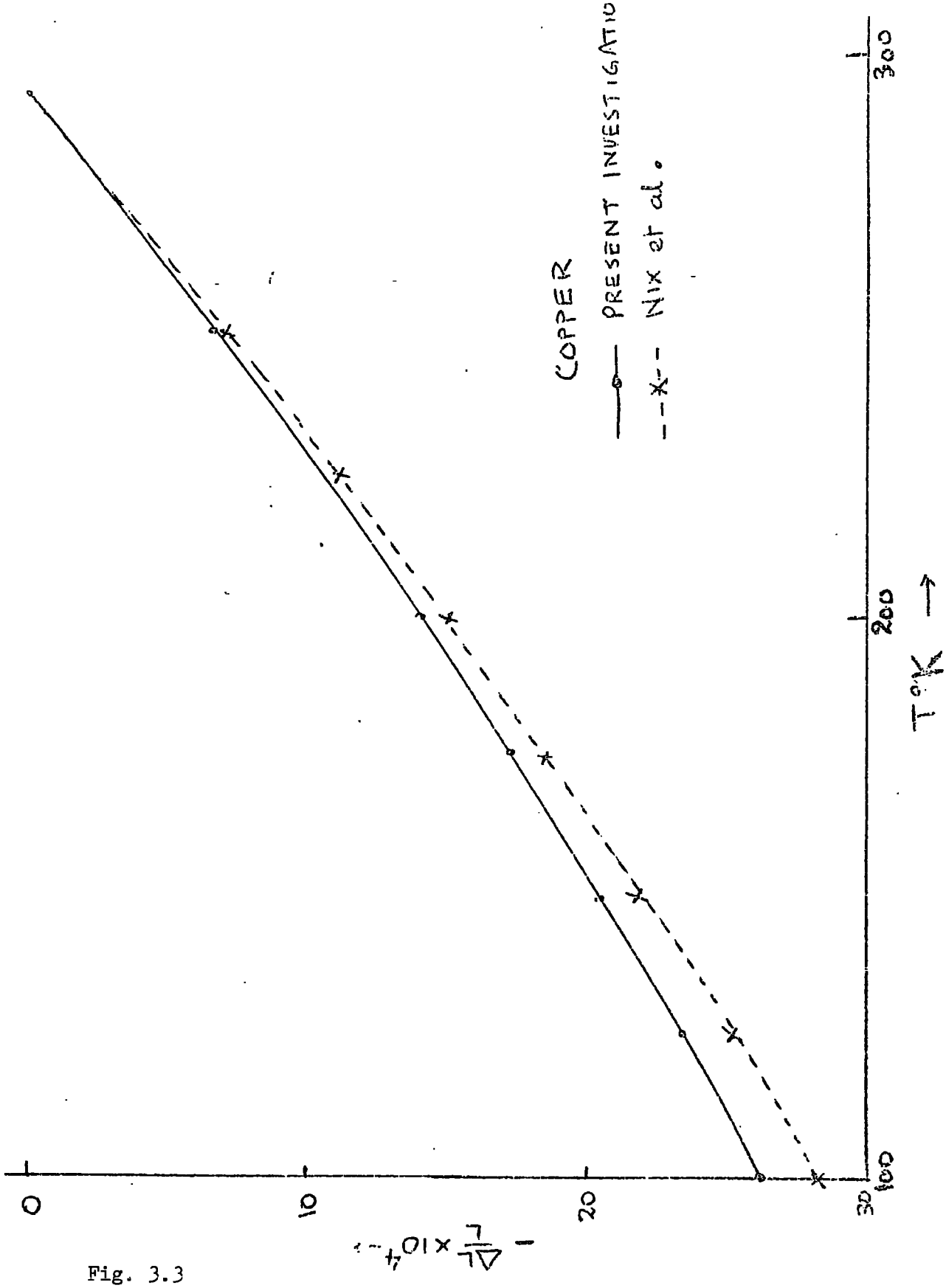
COPPER
PRESENT INVESTIGATION
Nix et al.
0
10
20
30
100
200
300
T°K →
$-\frac{\Delta L}{L} \times 10^{4}$ →

Fig. 3.3

3.7 Magnetization Measurement

A vibrating sample magnetometer of Foner type was used to determine magnetization of the alloys. The details of the apparatus have been described by Piercy(79).

(a) Vibrating Specimen Magnetometer

The apparatus was a null output instrument and the block diagram is shown in Fig. 3.4. The single crystals as well as polycrystalline materials vibrated in a magnetic field provided by a water cooled solenoid. A 'sample' coil around the specimen and a 'monitor' coil were individually twin coils connected in series opposition. An electrical signal could be observed depending on the magnitude of the magnetization. This was amplified and passed to the phase sensitive detector and meter. This signal could be balanced by passing a suitable current to the d.c. coil from a 6 volt battery. The magnitude of this current, measured by a milliammeter was a measure of the magnetization. As the signal from the 'sample' pickup coil could in some cases be too large to be balanced by the 'monitor' coil, a potential divider using a 250 kΩ helipot was used. Coherent noise in the 'monitor' coil was backed off using a phase shift network and an attenuator.

The disc shaped specimen were stuck by 'Durofix' in a groove cut in a quartz tube as shown in the inset in Fig. 3.5. The apparatus was suitable for handling a 5.5mm. long specimen and in the configuration used the magnetic field was along the diameter of the disc and along the axis of the quartz tube. The diameter of disc chosen to be along the quartz tube axis was one of the principal crystal axes. The strain gauges stuck on the discs

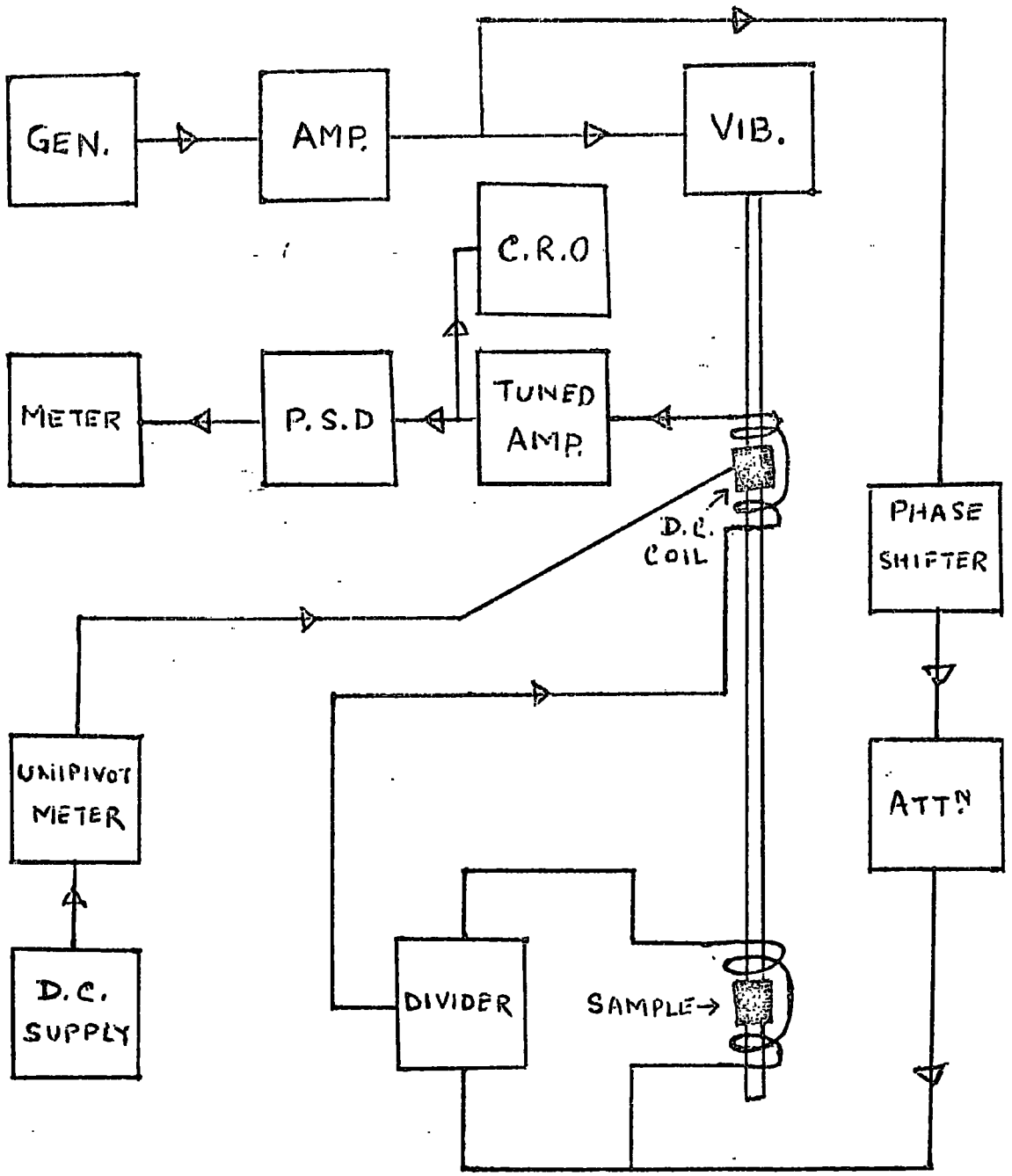
GEN.
AMP.
VIB.
C.R.O
METER
P.S.D
TUNED AMP.
D.C. COIL
PHASE SHIFTER
UNIPIVOT METER
ATTN
D.C. SUPPLY
DIVIDER
SAMPLE→

Fig. 3.4

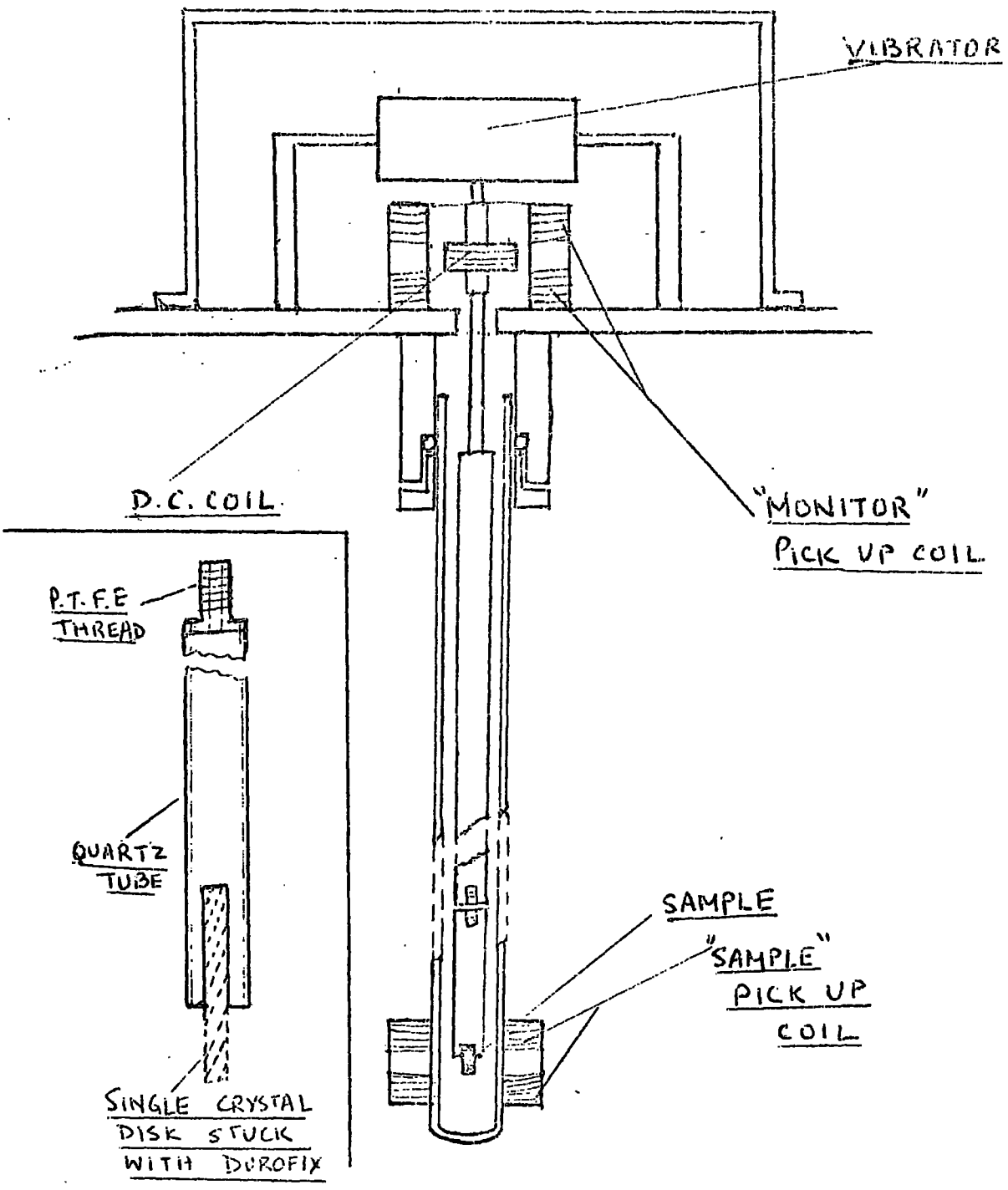
VIBRATOR
D.C. COIL
"MONITOR"
PICK UP COIL
P.T.F.E
THREAD
QUARTZ
TUBE
SAMPLE
"SAMPLE"
PICK UP
COIL
SINGLE CRYSTAL
DISK STUCK
WITH DUROFIX

Fig. 3.5

served as a useful secondary standard to check the alignment. Taking all the factors into account, the accuracy in the direction of alignment was about $\pm 4^{\circ}$. The centre of the disc and the centre of the 'sample' coil were made coincident by measuring the positions w.r.t. fixed points as well as by checking the output of the 'sample' coil as a function of position. The temperatures of the specimens were measured by a copper-constantan thermocouple passing through the specimen holder tube and the junction of the thermocouple was in close proximity of the specimen. The thermo-e.m.f. was measured by a portable potentiometer and Scalamp galvanometer. For polycrystalline specimens a lump of the material was stuck at the end of a quartz specimen tube, the direction not being of any importance in these cases.

(b) Data and its Treatment

The current measured by the milliammeter could be converted to magnetization by calibrating the instrument. Samples of pure Iron and Nickel of known mass were used and the data of Weiss and Forrer(80) was used. If σ is the magnetization per unit mass and ω is the mass of specimen used and a current I is required to balance the signal from the 'sample' coil, then

$$\sigma = A\, I/\omega \qquad \ldots\ldots (3.3)$$

where A is a constant. To obtain the magnetization per atom (μ) in an alloy 'AB', containing a fraction x of element A, the relation

$$\mu = \frac{\sigma M}{5586} \qquad \ldots\ldots (3.4)$$

where M is the effective atomic weight of the alloy given by

$$M = x\, M_A + (1 - x)\, M_B \qquad \ldots\ldots (3.5)$$

where M_A and M_B are the atomic weights of the elements A and B. The equipment could measure a minimum magnetization of 5×10^{-3} e.m.u. corresponding to I of 0.1 mA. The overall accuracy in σ was estimated to be $\pm 3\%$.

Standard double dewar techniques were used for liquid Helium temperature work and a single dewar was used between 77°K and room temperature. The specimen was surrounded by a helium gas atmosphere during the measurements.

The magnetization measurements yielded information about the paramagnetic Curie point, effective paramagnetic moment, the Néel point, the ferromagnetic Curie point, the saturation magnetization at different temperatures and the behaviour of the critical field required to trigger a transition from the antiferromagnetic to the ferromagnetic state.

For the determination of the paramagnetic Curie point (θ_p) and the effective moment in the paramagnetic state (μ_{eff}), a graph of $1/\sigma$ against the temperature T was plotted. The intercept on the T axis for the linear portion gave the value of θ_p. The gradient of the graph was used to obtain the Curie constant C. If C is expressed in e.m.u. °K gm mole^{-1} Oe^{-1}, then

$$\mu_{eff} = 2.83 \sqrt{C} \qquad \ldots\ (3.6)$$

gives the value of μ_{eff} in Bohrmagnetons/ion. In case of the alloy 'AB' described by the eqn.(3.5), the effective paramagnetic moments of the alloy and the constituents are related by

$$\mu_{AB} = \left[\mu_A^2 x + \mu_B^2 (1 - x) \right]^{\frac{1}{2}} \qquad \ldots.(3.7)$$

where μ_{AB} = effective paramagnetic moment per ion of AB,

μ_A = effective paramagnetic moment per ion of A,

and μ_B = effective paramagnetic moment per ion of B.

When B is a non-magnetic constituent,

$$\mu_{AB} = \mu_A \sqrt{x} \qquad \ldots\ldots (3.8)$$

This relation was used to obtain the paramagnetic moment per terbium ion.

There are several methods for the determination of ferromagnetic Curie point from the experimental data. In this investigation σ^2 was plotted as a function of temperature (T) in a given magnetic field of strength H. The extrapolation to $\sigma^2 = 0$ gave a set of values of T as a function of H, from different sets of experiments. The extrapolation to H = 0 gave a temperature T_c, which was considered to be the ferromagnetic Curie point. The data connecting H and T gave the variation of critical field with temperature, σ - T plots showed characteristic peaks at the Néel point, which disappeared at magnetic fields higher than the critical value. The position of the Néel point was a function of the magnetic field and the extrapolation to zero field was taken to be the Néel point (T_N). To obtain the saturation moment, the σ vs. $1/H$ plot was extrapolated to $H = \infty$. The resultant value of σ was taken to be the saturation moment. To obtain the saturation moment per terbium atom from the alloy, it was assumed that the scandium atom does not carry any moment. Under these circumstances

$$\mu_{Tb}/\text{ion} = \frac{\mu\text{alloy/ion}}{x} \qquad \ldots\ldots (3.9)$$

where $\mu_{Tb/ion}$ is the saturation moment per terbium ion,

μ alloy/ion is the saturation moment per ion of the alloy and x is the fractional concentration of terbium. The majority of the data were taken in isofield condition and the saturation magnetization at any temperature T was obtained by the extraction of information from several σ - T (isofield) curves. This was not altogether satisfactory but the apparatus was not suitable for use at temperatures intermediate between the various fixed temperature baths (liq. Ne, liq. N_2, dry ice, pentane slush etc.).

The specimens used in all the experiments performed on single crystals were disc shaped. The shape is not conducive to the calculation of the effect of the demagnetizing field. Any estimation of the demagnetizing factor for non-ellipsoidal bodies is open to errors as pointed out by Zijlstra(81). The value of the demagnetizing factor for an oblate ellipsoid is perhaps the nearest to that of the discs used in the experiments. For a ratio of 5:1 for the length of the axes the value of the demagnetizing factor is approximately 0.12. For a disc magnetized along the diameter, this is small and so all the results are quoted in terms of the applied magnetic field.

CHAPTER 4

EXPERIMENTAL RESULTS

4.1 X-ray Lattice Parameter and Density Measurements

The 'a' and 'c' parameters at room temperature of the alloys are shown in Fig. 4.1. The powder diffraction patterns obtained consisted of sharp lines and analysis of the data yielded estimates of the lattice parameters to ± 0.005 Å. The 'a' axis parameter lies on a straight line joining the terminal values within experimental accuracy while the 'c' axis parameters at intermediate compositions fall below this line. Vegards' Law is not obeyed for this parameter. Deviations have been noted in other rare earth alloy systems. The X-ray densities (ρ x-ray) of the alloys were estimated from the lattice parameters and compositions using the relationship

$$\rho \text{ x-ray} = \frac{ZA}{VN} \qquad \ldots\ldots (4.1)$$

where Z = No. of atoms per unit cell (= 2)

A = Formula weight,

V = Cell volume ($= \frac{a^2 c \sqrt{3}}{2}$)

and N = Avogadro's number

Independent measurements of the densities were made using pycnometric methods as described in the previous chapter. The results of the X-ray density and the pycnometric density measurements are shown in Fig. 4.2. Within experimental errors involved the two agree well, with the pycnometric density always giving a slightly higher value. The corresponding values for the terminal elements also show the same characteristic, the pycnometric density being slightly higher than the X-ray density. The densities and the lattice parameters for the various alloy compositions are listed in Table 4.1.

TABLE 4.1

Alloy	Lattice Parameter a ± 0.005 Å	c ± 0.005 Å	Density Gms/c.c. X-ray ± 1%	Pycnometric ± 1%
$Tb_{0.89}Sc_{0.11}$	3.57	5.646	7.8	7.85
$Tb_{0.825}Sc_{0.175}$	3.551	5.592	7.55	7.64
$Tb_{0.695}Sc_{0.305}$	3.514	5.568	6.96	7.07
$Tb_{0.5}Sc_{0.5}$	3.456	5.455	6.01	6.08
$Tb_{0.35}Sc_{0.65}$	3.408	5.395	5.21	5.25
$Tb_{0.25}Sc_{0.75}$	3.383	5.353	4.58	4.67

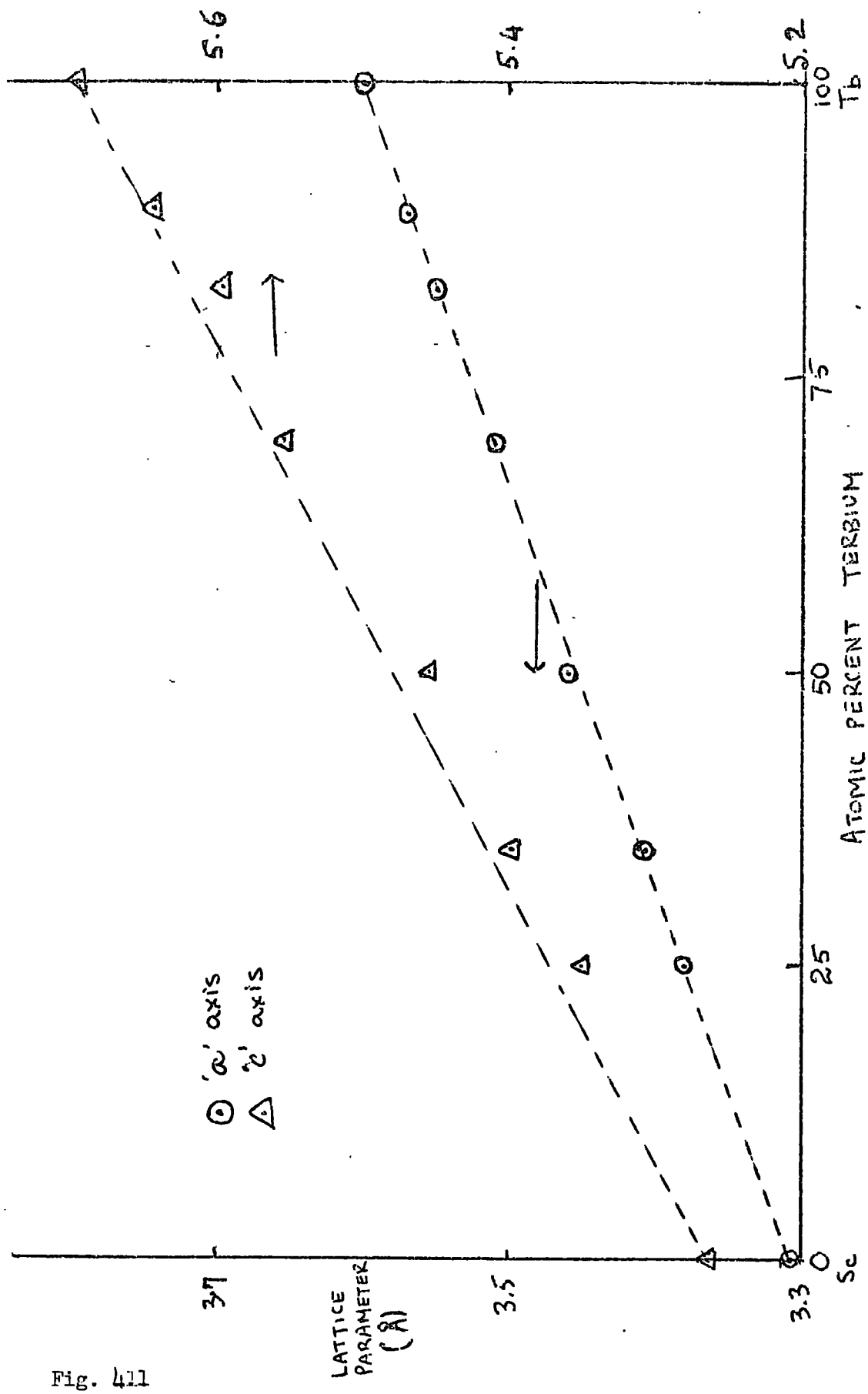
5.6
5.4
5.2
100
Tb
75
50
25
0
Sc
ATOMIC PERCENT TERBIUM
3.7
3.5
3.3
LATTICE PARAMETER (Å)
'a' axis
'c' axis

Fig. 411

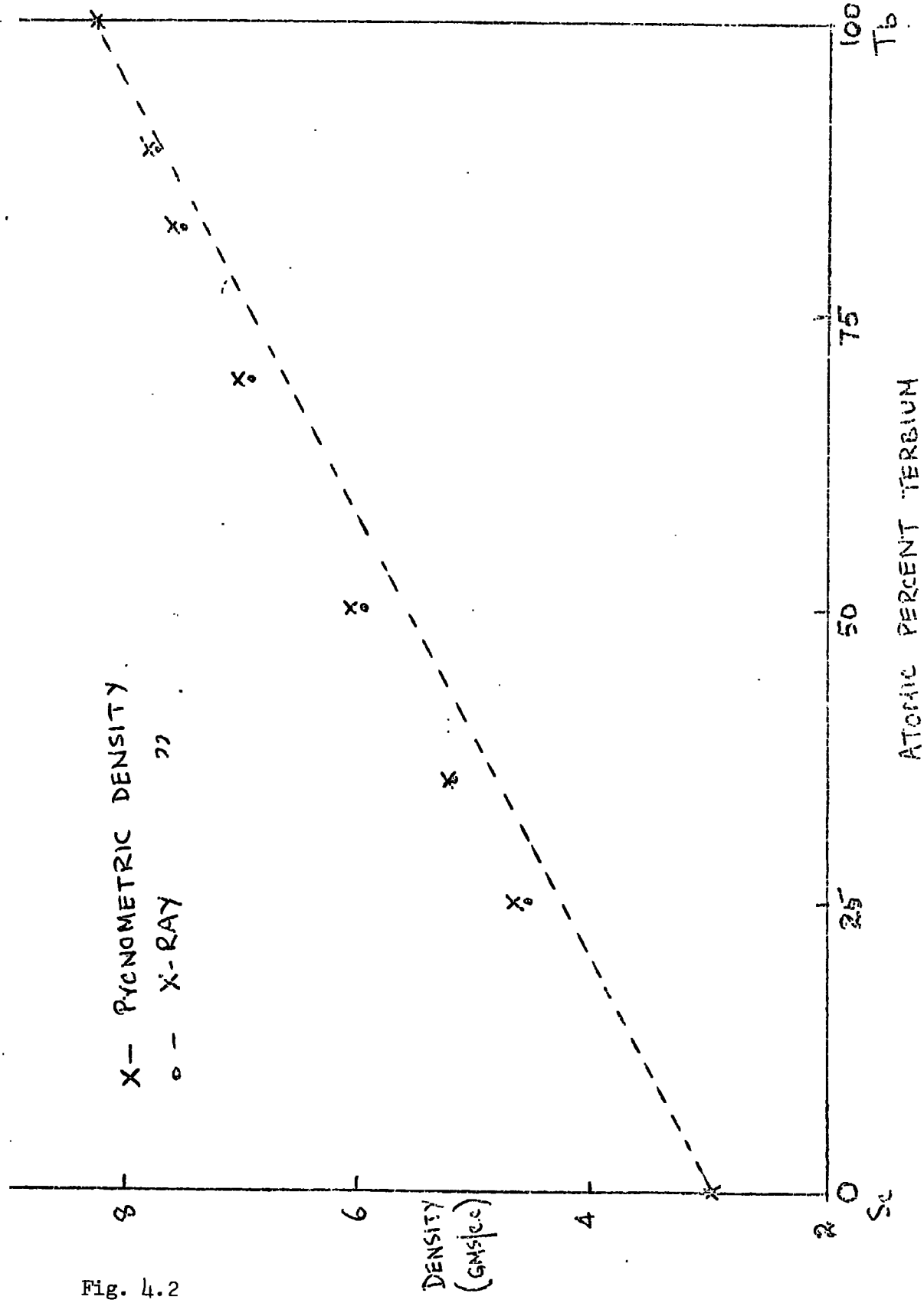
X— PYCNOMETRIC DENSITY
o — X-RAY
"
DENSITY (GMS/C.C)
8
6
4
2
0
Sc
25
50
75
100
Tb
ATOMIC PERCENT TERBIUM

Fig. 4.2

4.2 Magnetization Measurement

Magnetization was measured along the principal directions of the alloy discs and on polycrystalline lumps. The results are given in the sequence of increasing scandium concentrations.

(a) $Tb_{0.89}\ Sc_{0.11}$

Figs. 4.3 and 4.4 show the magnetization against field (σ -H) plots at three different temperatures for the a and b directions. The c axis is magnetically very hard and the σ -H plots are linear. The a axis is the easy direction of magnetization and shows a good degree of saturation while the b axis σ - H curve at 4.2°K shows a gradient even at a field of 10 kOe. The saturation moment along the a axis has been estimated and the moment on each terbium atom calculated.

Fig. 4.5 shows the variation of σ against T for some values of the magnetic field for the a direction. There is very little change in σ between 4.2°K and about 100°K when it shows a fall. The transition from the helical antiferromagnetic state to the ferromagnetic state is associated with this change in magnetization. As discussed in the previous chapter, the variation of the critical field with temperature and the ferromagnetic Curie point can be estimated. A cusp in the σ -T curve just below 200°K is observed in lower magnetic fields. The cusp is swamped at higher fields and only a trace is present. The cusp is associated with the Néel point and T_N is obtained by extrapolation to zero magnetic field. Fig. 4.6 shows the temperature variation of the critical field in this alloy. It is linear up to about 190°K above which the data is not clear enough to say whether there

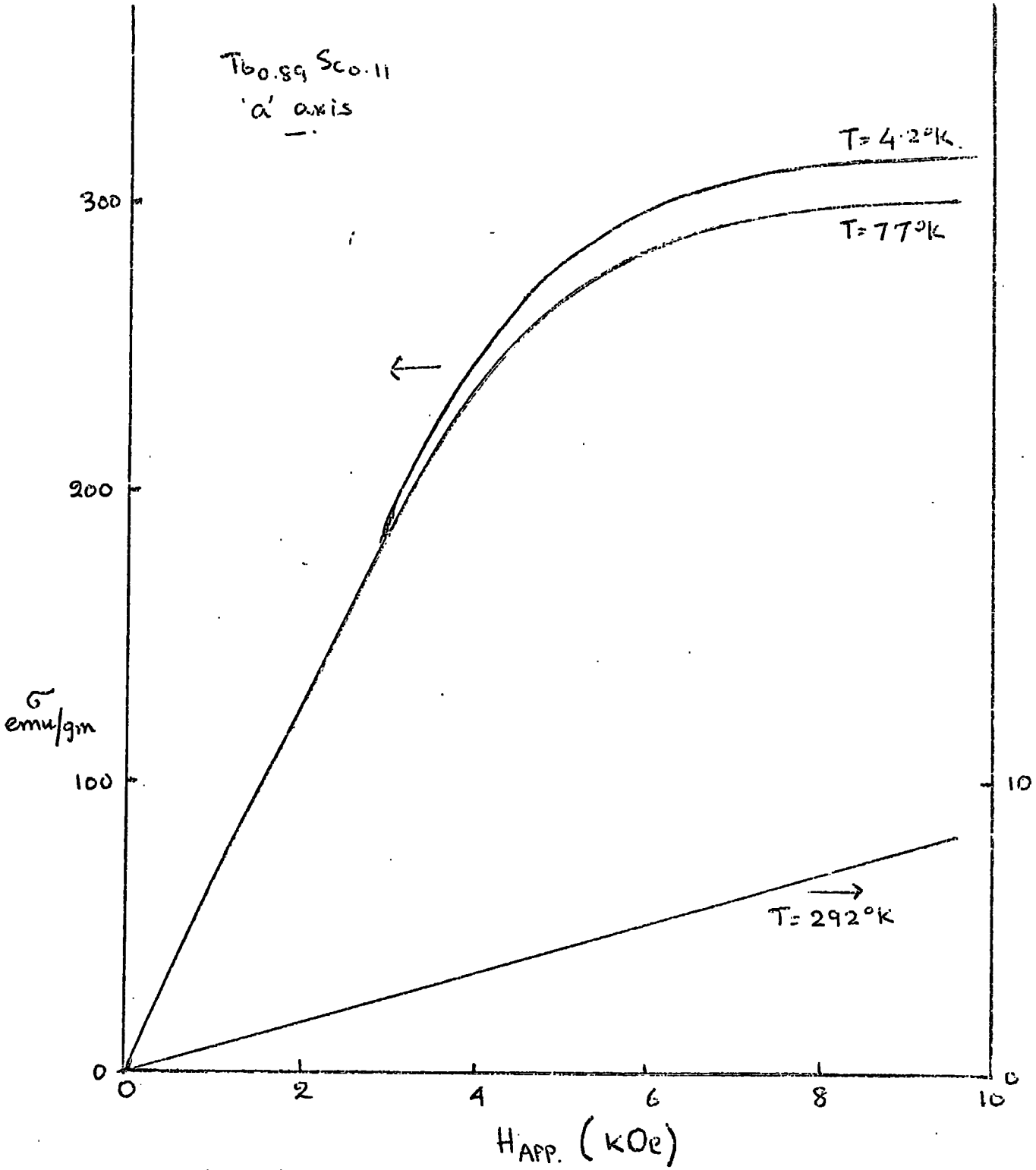
Tb0.89 Sc0.11
'a' axis
T= 4·2°K.
T= 77°K
T= 292°K
300
200
100
0
σ
emu/gm
10
0
0
2
4
6
8
10
H APP. (kOe)

Fig. 4.3

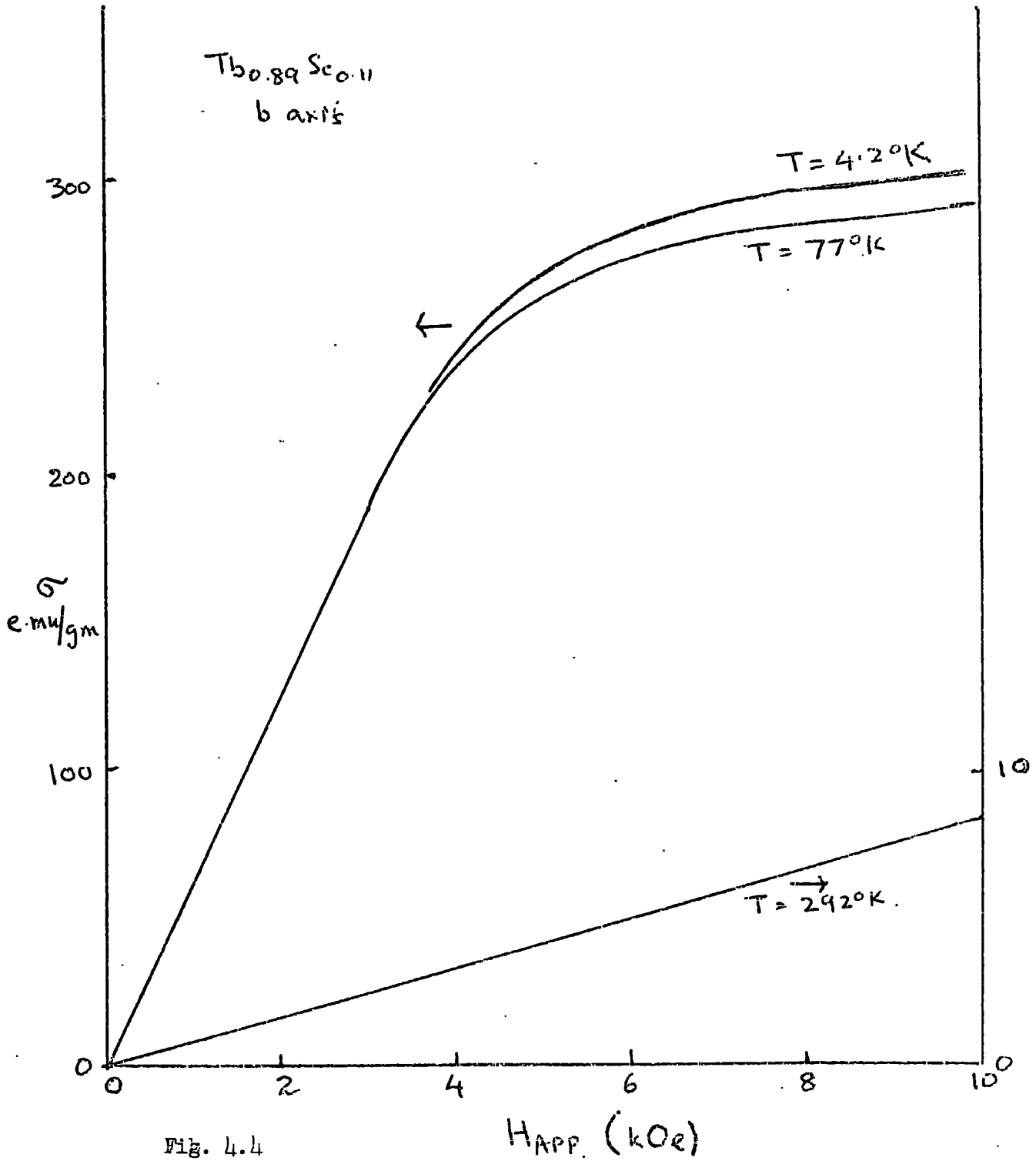
$Tb_{0.89}Sc_{0.11}$
b axis
T = 4.2°K
T = 77°K
T = 292°K.
300
200
100
0
σ
e.mu/gm
0
2
4
6
8
10
10
0
$H_{APP.}$ (kOe)

Fig. 4.4

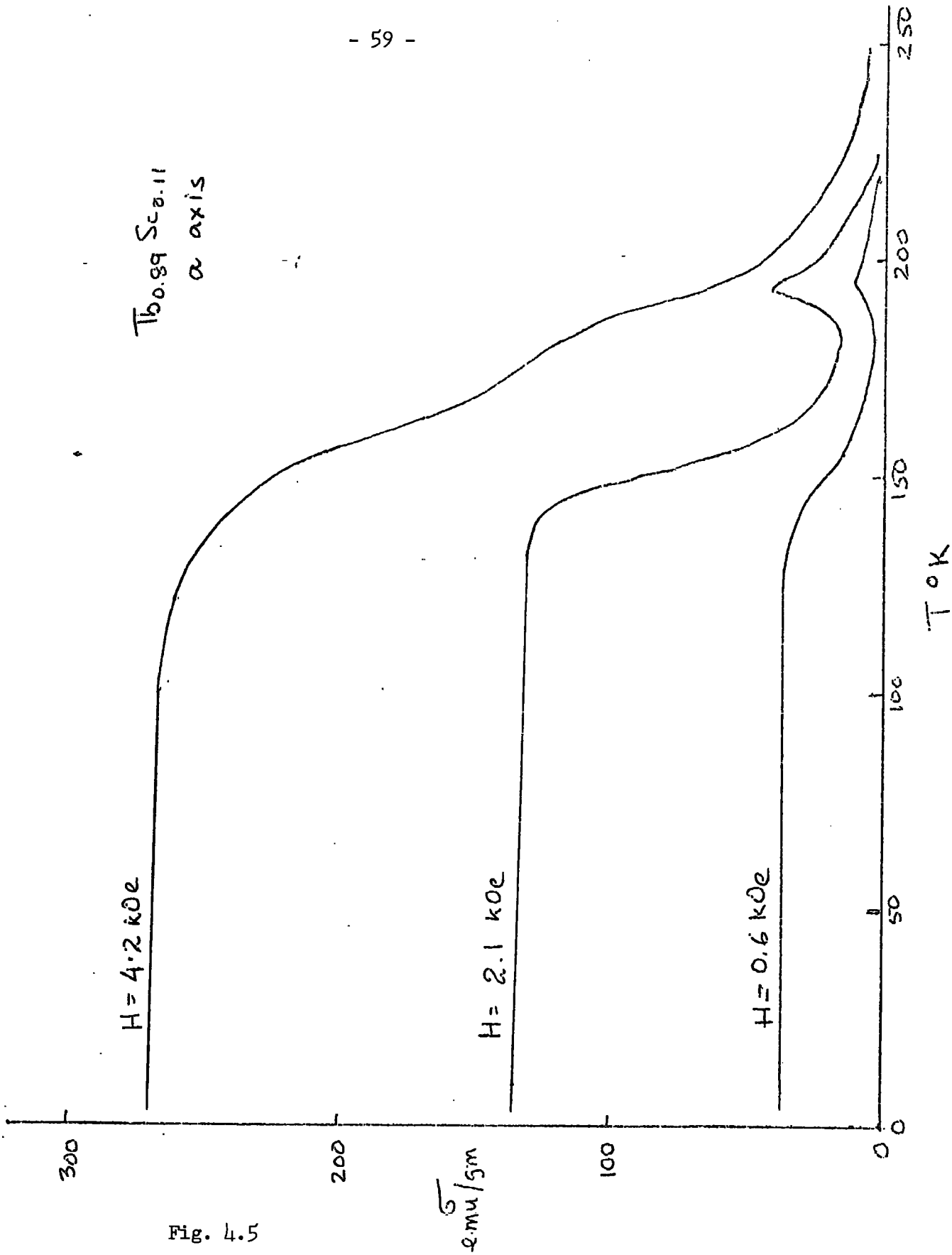
$Tb_{0.89}Sc_{0.11}$
a axis
H = 4·2 kOe
H = 2.1 kOe
H = 0.6 kOe
σ e.mu/gm
T °K
0
50
100
150
200
250
100
200
300

Fig. 4.5

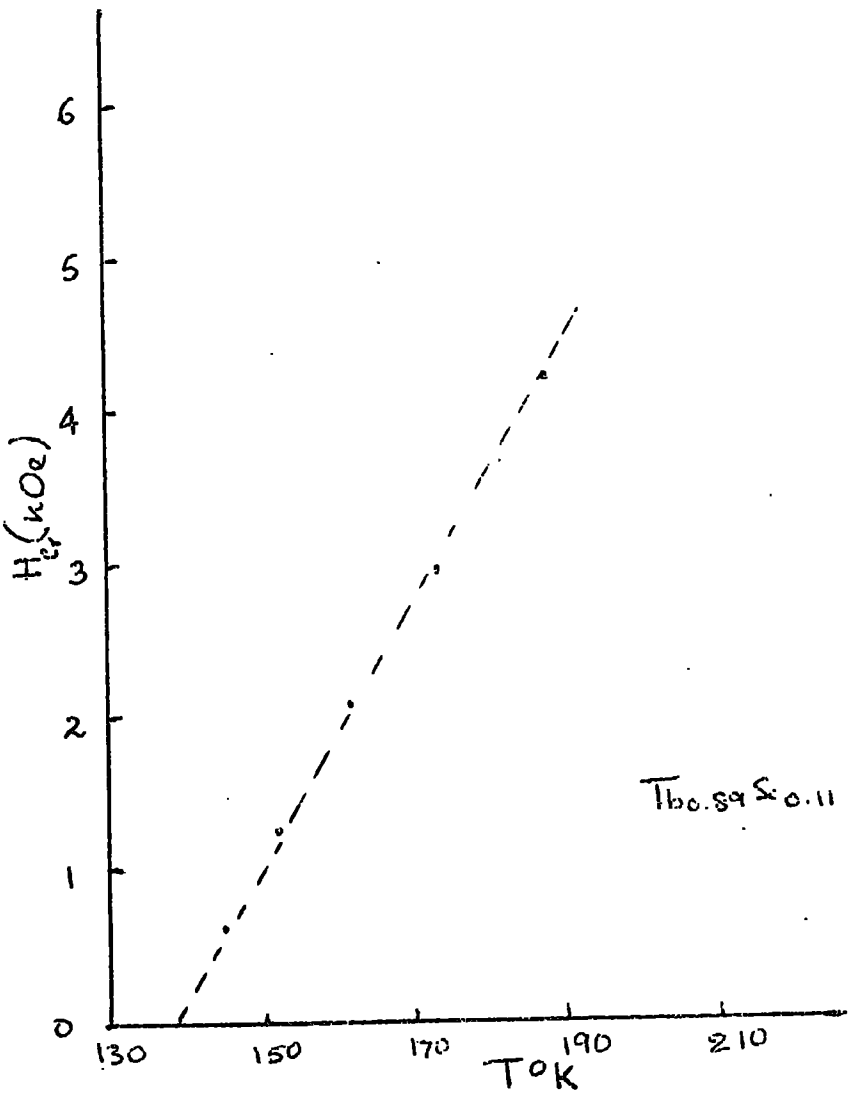

Fig. 4.6

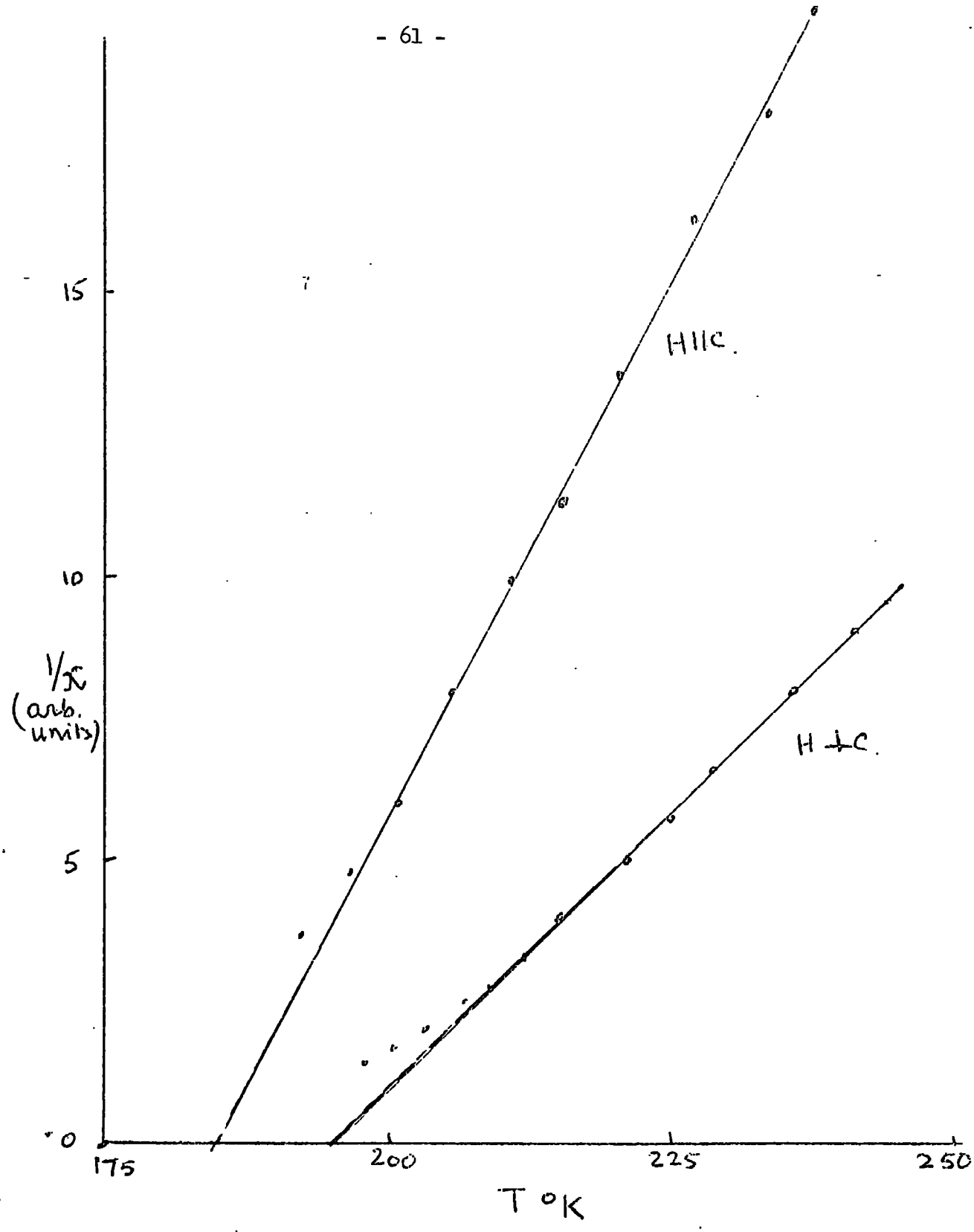

Fig. 4.7

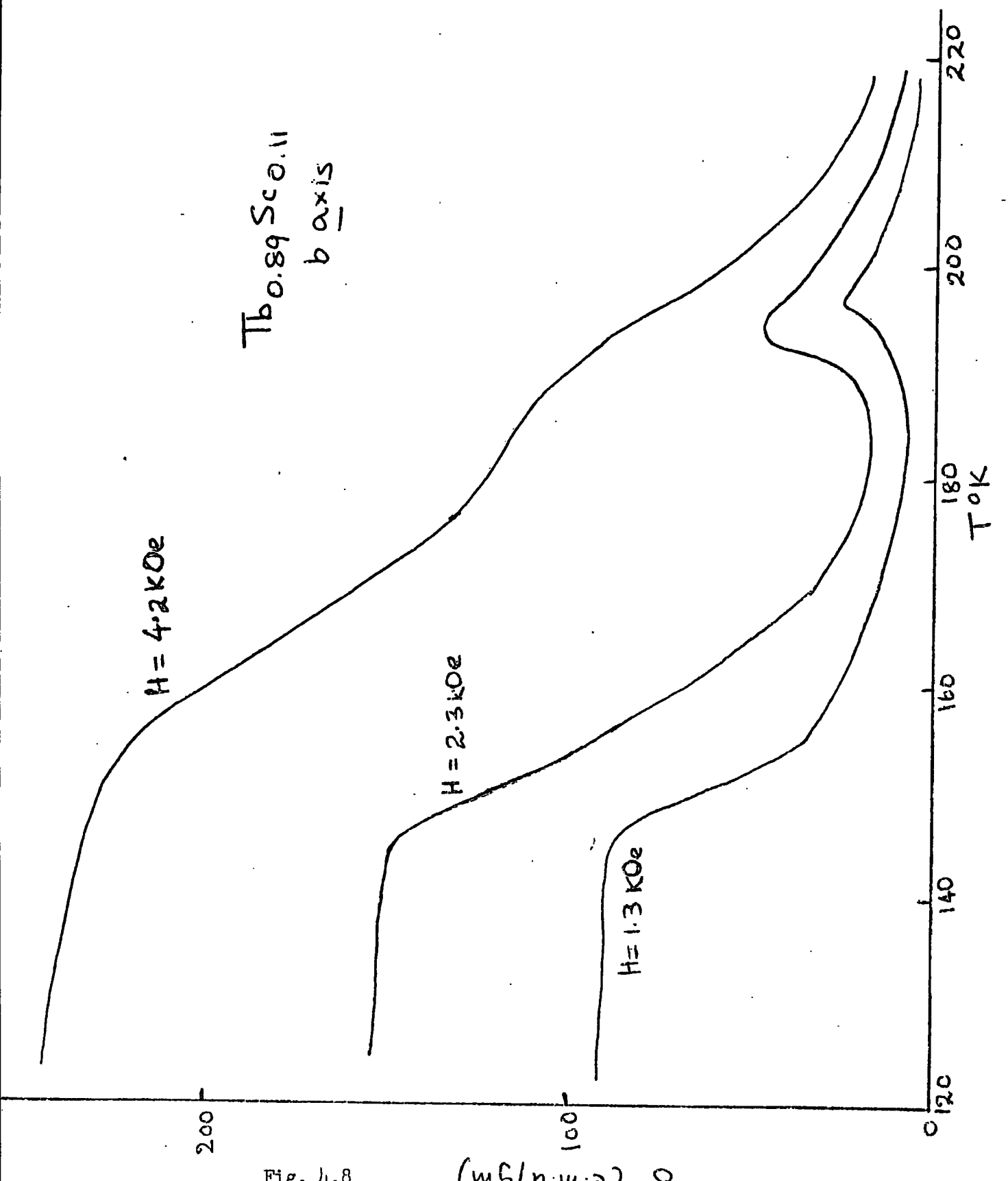
$Tb_{0.89}Sc_{0.11}$
b axis
H = 4.2 kOe
H = 2.3 kOe
H = 1.3 kOe
σ (e.m.u/gm)
200
100
0
120
140
160
180
200
220
T °K

Fig. 4.8

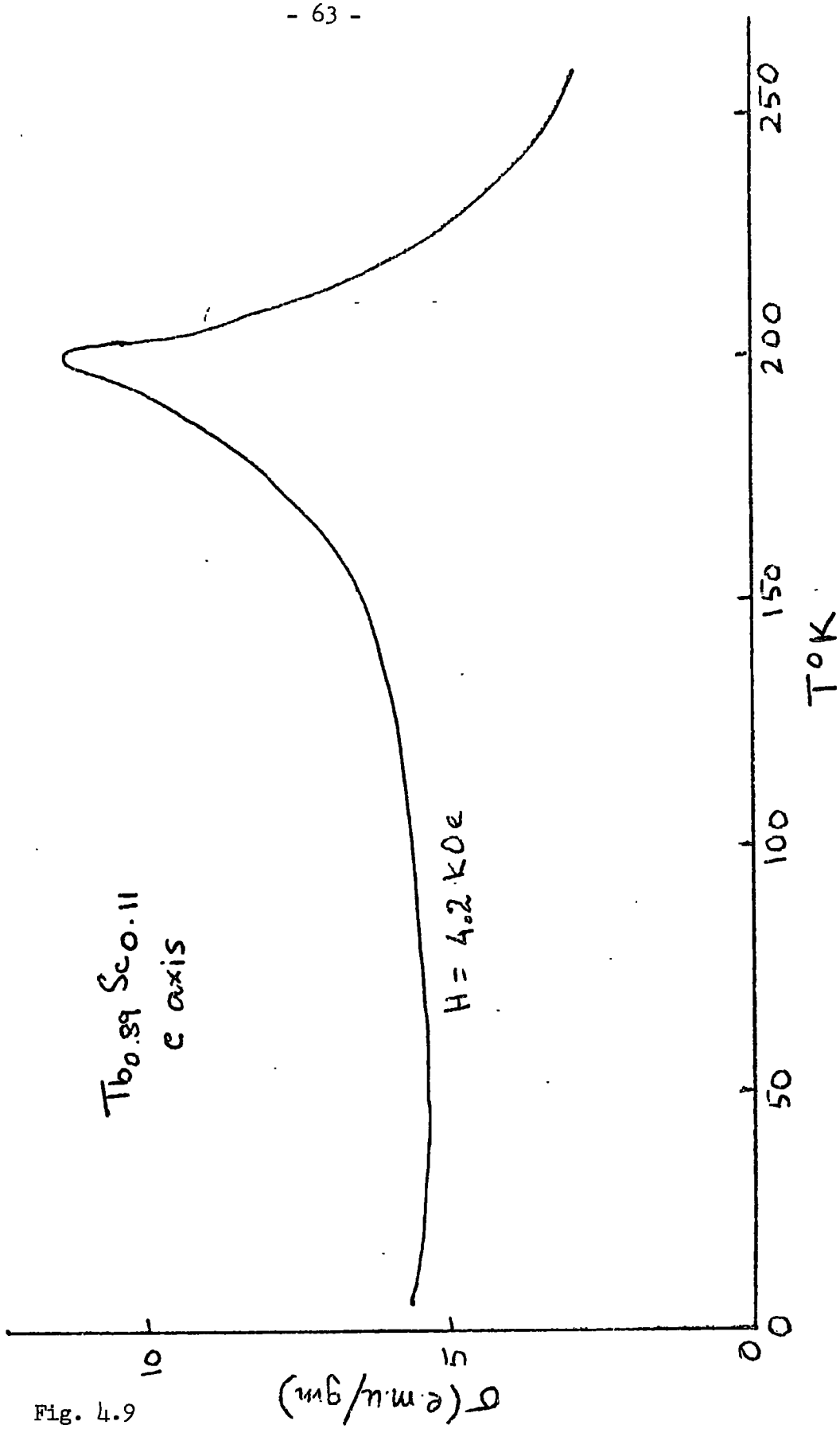

Fig. 4.9

is a fall off, as observed in some heavy rare earth metals and some alloys. Above the Néel point, the magnetization results were used to obtain $^1/\chi$ against T plots. It is observed that $^1/\chi$ shows a Curie-Weiss type of behaviour, but deviation is observed as the Néel temperature is approached. From the $^1/\chi$ vs T plots, the paramagnetic Curie points along the different axes and the effective paramagnetic moments were calculated. Fig. 4.7 shows the $^1/\chi$ vs T plots along the different axes. Figs. 4.8 and 4.9 show the σ-T plots for the alloy along the b and c axes. The details along the b axis are essentially the same as those for the a axis, whereas the c axis data only show the cusp at the Néel point and do not show the increase corresponding to the antiferromagnetic to ferromagnetic ordering. The polycrystalline Curie point may be well represented by a weighted average of the basal plane and the c axis θ_p values according to

$$\theta_p(\text{poly}) = {}^2/3\ \theta_p(\text{basal}) + {}^1/3\ \theta_p(\text{c-axis}) \qquad \ldots\ldots (4.1)$$

(b) $Tb_{0.825}Sc_{0.175}$

The magnetization characteristics of this alloy are similar to those of $Tb_{0.89}\ Sc_{0.11}$ and the results are shown in Figs. 4.10-4.12. The details are so similar to those of $Tb_{0.89}\ Sc_{0.11}$ that it is not of great importance to explain the figures.

(c) Other Compositions

Magnetization was measured for the alloys of composition $Tb_{0.695}\ Sc_{0.305}$, $Tb_{0.5}\ Sc_{0.5}$, $Tb_{0.35}\ Sc_{0.65}$ and $Tb_{0.25}\ Sc_{0.75}$. With the exception of $Tb_{0.25}\ Sc_{0.75}$ which does not show magnetic ordering, the alloys showed an antiferromagnetic ordering. The

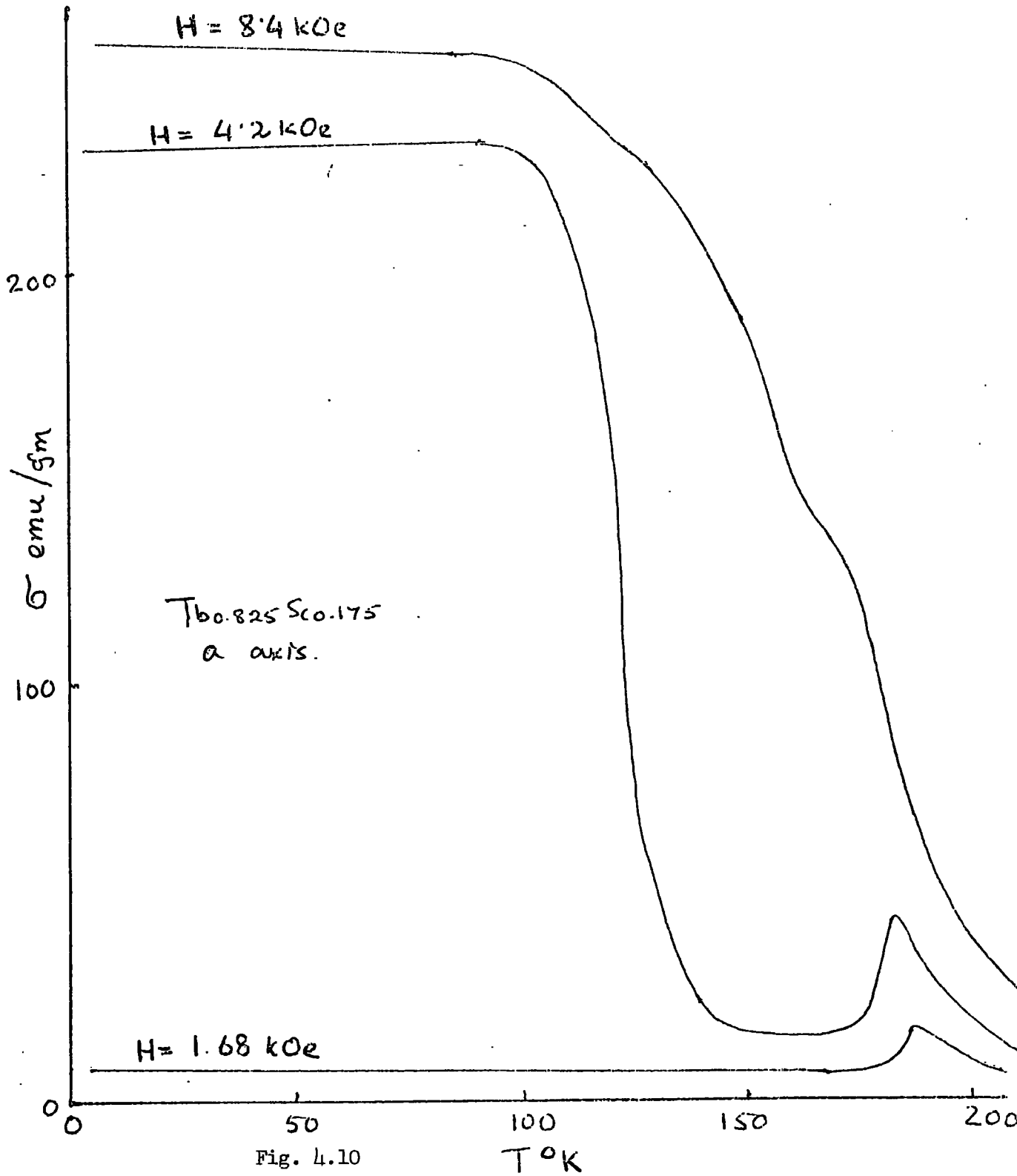
H = 8·4 kOe
H = 4·2 kOe
H = 1·68 kOe
Tb0.825 Sc0.175
a axis.
σ emu/gm
200
100
0
0
50
100
150
200
T °K

Fig. 4.10

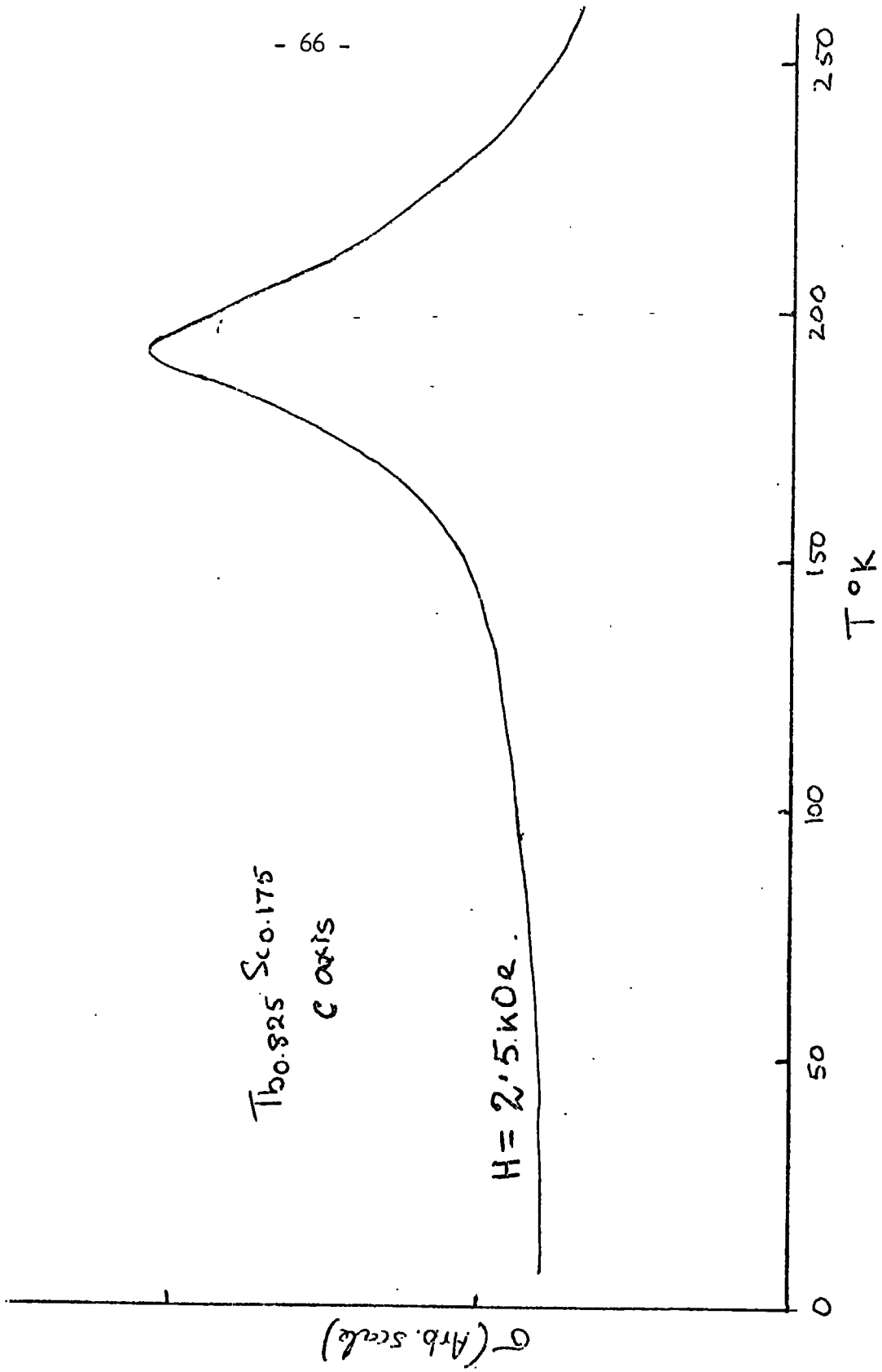

Fig. 4.11

TABLE 4.2

Alloy	θ_p °K basal, ± 1	θ_p °K c axis ± 2	θ_p °K polycrystaline ± 2	T_N ±2	θ_5 ±1	μ_{eff}/Tb ion Bohr ±0.2	μ_{sat}/Tb atom Magnetons ± 2
$Tb_{0.89}$ $Sc_{0.11}$	195	180	190	197	136	10.2	9.6
$Tb_{0.825}$ $Sc_{0.175}$	186	138	170	188	75	9.9	9.4
$Tb_{0.695}$ $Sc_{0.305}$	-	-	130	152	-	9.7	-
$Tb_{0.5}$ $Sc_{0.5}$	-	-	63	95	-	10.3	-
$Tb_{0.35}Sc_{0.65}$	-	-	40	60	-	10.2	-
$Tb_{0.25}$ $Sc_{0.75}$	-	-	15	-	-	10.1	-

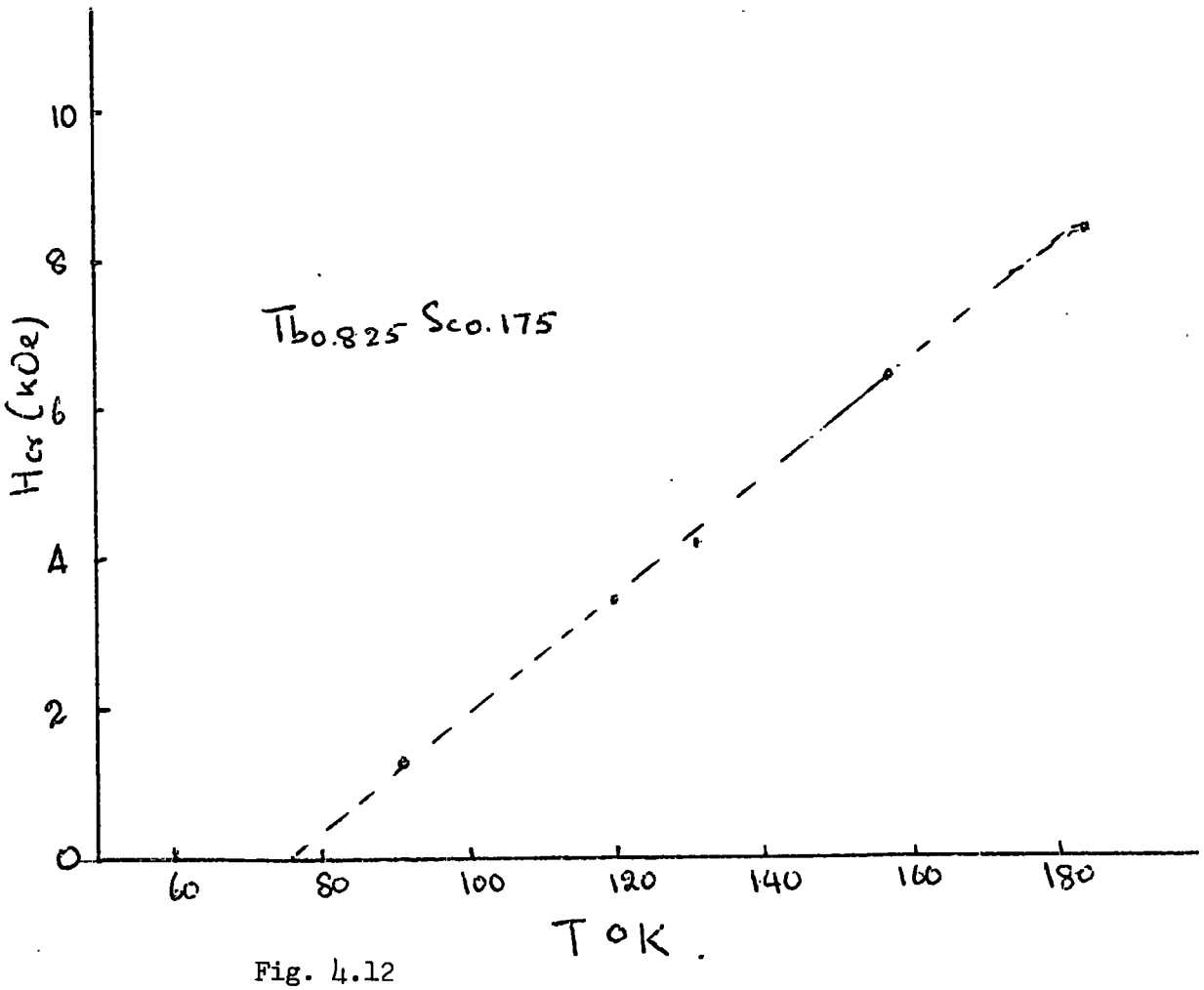

Fig. 4.12

results for the alloys which show antiferromagnetic ordering may be characteristically represented by the behaviour of $Tb_{0.5}Sc_{0.5}$ and shown in Fig. 4.13.

The magnetic data is summarised in Table 4.2.

4.3 Magnetostriction and Thermal Expansion Measurement

The prime object of these measurements was to obtain the $\lambda^{\gamma,2}$ term of the Callen and Callen expression (eqn. 2.18) to evaluate the magnetostrictive energy and thus obtain an estimate for the driving force to ferromagnetism and so magnetostriction measurements were made on the two alloys which show ferromagnetism.

Preliminary measurements were made on single crystals of terbium, dysprosium and holmium as an exercise in evaluating the performance of the experimental apparatus. Fig. 4.14 shows the thermal expansion for the b and c directions of a terbium single crystal.

Thermal expansion was measured between 77°K and 292°K along the a,b and c directions of the $Tb_{0.89}Sc_{0.11}$ alloy single crystal and the results are shown in Fig. 4.15-4.16. Along the basal plane directions, a change in the gradients of the $\Delta L/L$ vs T curves is observed around the Néel temperature and a discontinuity at the Curie point is observed. Along the c axis, there is contraction as the specimen is cooled down from the room temperature. Below the Néel temperature, the axis expands with decreasing temperature. There is a sharp contraction at the Curie point and at lower temperatures a small contraction is observed. The $\Delta L/L$ vs T curves are used to calculate the values of the expansion coefficients and these are shown in Fig. 4.17.

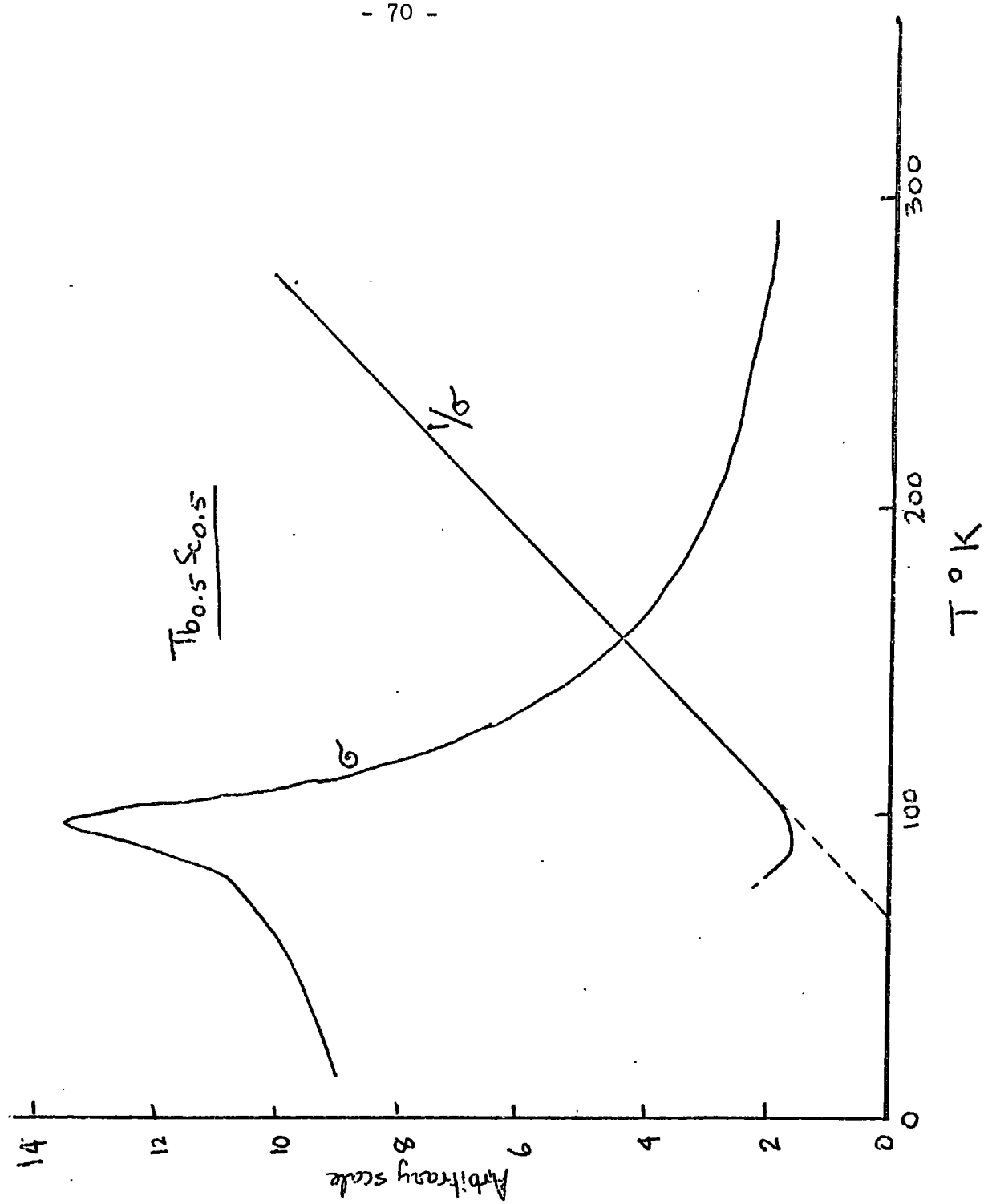

Fig. 4.13

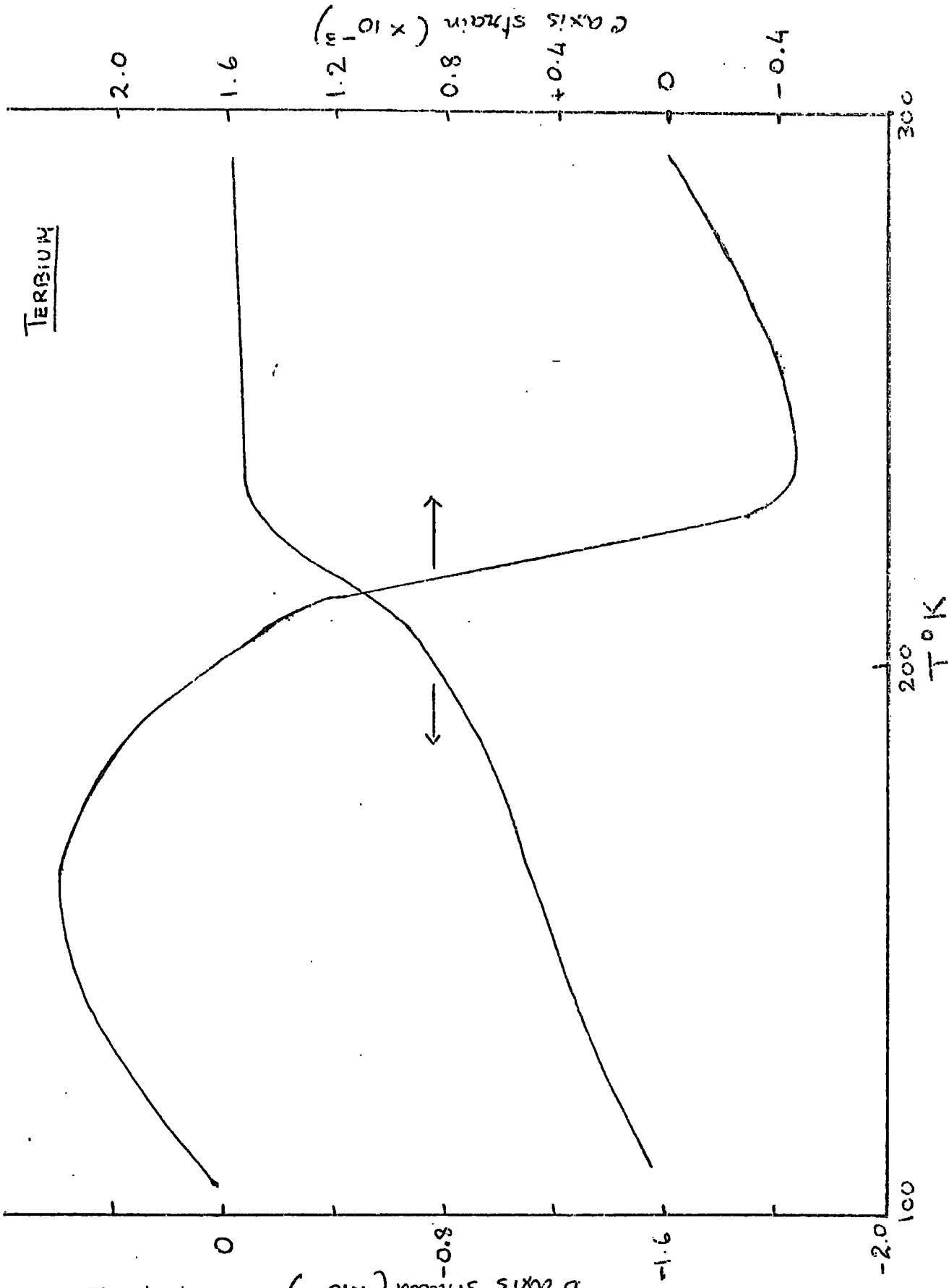
TERBIUM
b axis stress ($\times 10^{-3}$)
c axis strain ($\times 10^{-3}$)
T °K
100
200
300
-2.0
-1.6
-0.8
0
2.0
1.6
1.2
0.8
+0.4
0
-0.4

Fig. 4.14

The magnetostriction along the basal plane 'a' direction and along the 'c' direction was measured at room temperature. The magnetostriction for the paramagnetic range $\propto H^2$ and this behaviour was observed as shown in Fig. 4.18 for the c axis.

Experiments were performed on the basal plane specimen to observe the strain along the a axis as the field was rotated and also to observe the strains as the field was applied along the a and b directions. Fig. 4.19 (p.79) shows the a axis magnetostrain as a function of the angle of the magnetic field with the b direction at 77°K and 194°K for H = 10.25kOe. Fig. 4.20 (p.80) shows the variation of the magnetostrictive strain along the a direction when a field of 10.25kOe is applied along the a and b directions. The measurement of this is relevant to the estimation of the $\lambda^{\gamma,2}$ coefficient in the Callen and Callen expression. Measurements of the thermal strain for H = 0 are also included in Fig. 4.20. The measurement of the strain along the b direction with fields along the a and b direction also yields the value of $\lambda^{\gamma,2}$ and within experimental errors this was not different from those obtained for the a axis measurements. c axis measurements could not be made to yield reproducible results. The specimen, because of its large anisotropy, could not be held satisfactorily in position. Use of strong adhesives produced erratic results, possibly due to the strain induced by the adhesive.

Measurements on the $Tb_{0.825}$ $Sc_{0.175}$ alloy discs were also made along the scheme outlined for $Tb_{0.89}$ $Sc_{0.11}$ alloy discs. Fig. 4.21 (p.81) and 4.22 (p.83) shows the a and c axis thermal expansion ($\Delta L/L$) over the temperature range 80°K-290°K for the alloy.

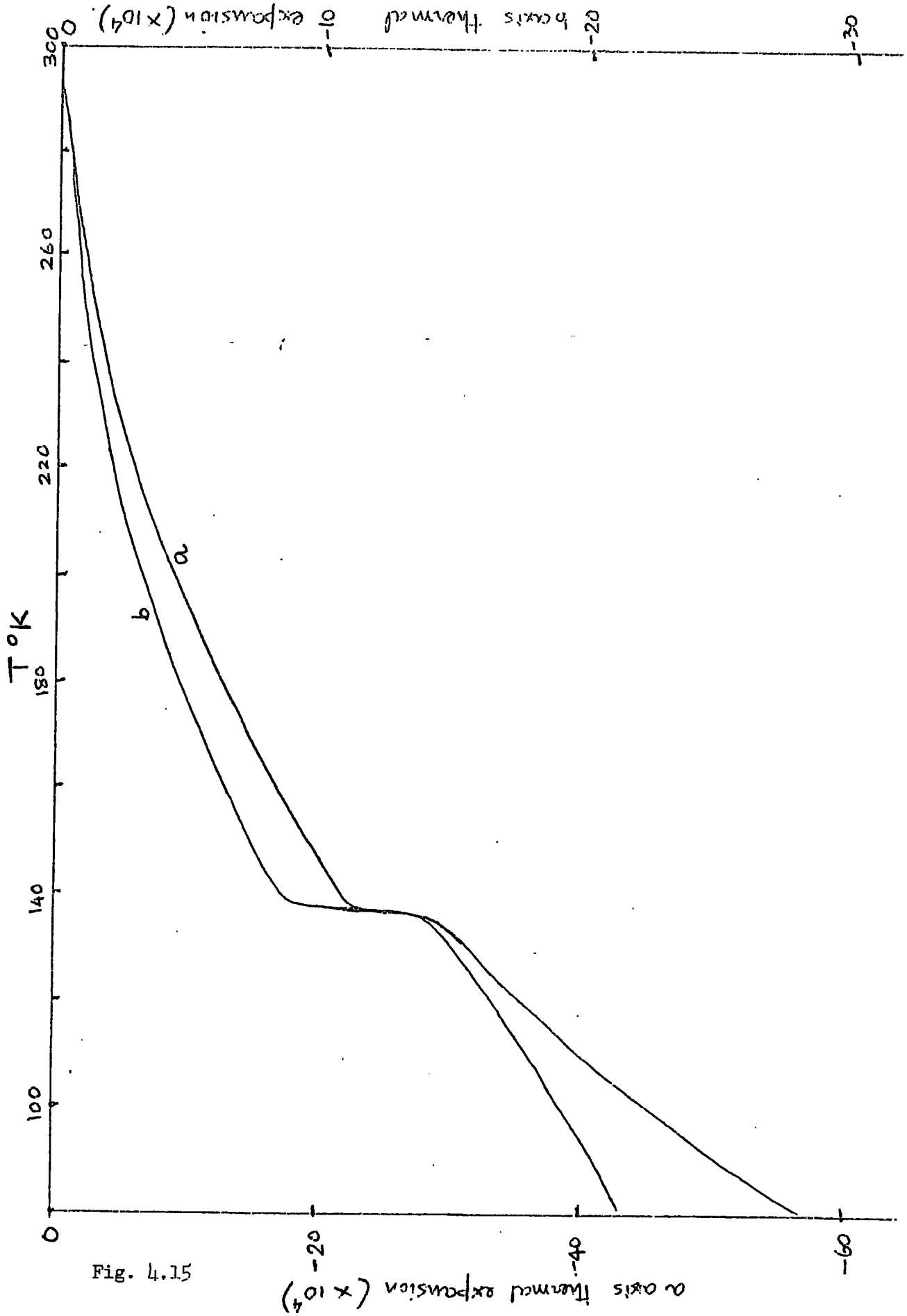
T °K
300
260
220
180
140
100
a
b
0
-20
-40
-60
a axis thermal expansion (× 10⁴)
0
-10
-20
-30
b axis thermal expansion (× 10⁴)

Fig. 4.15

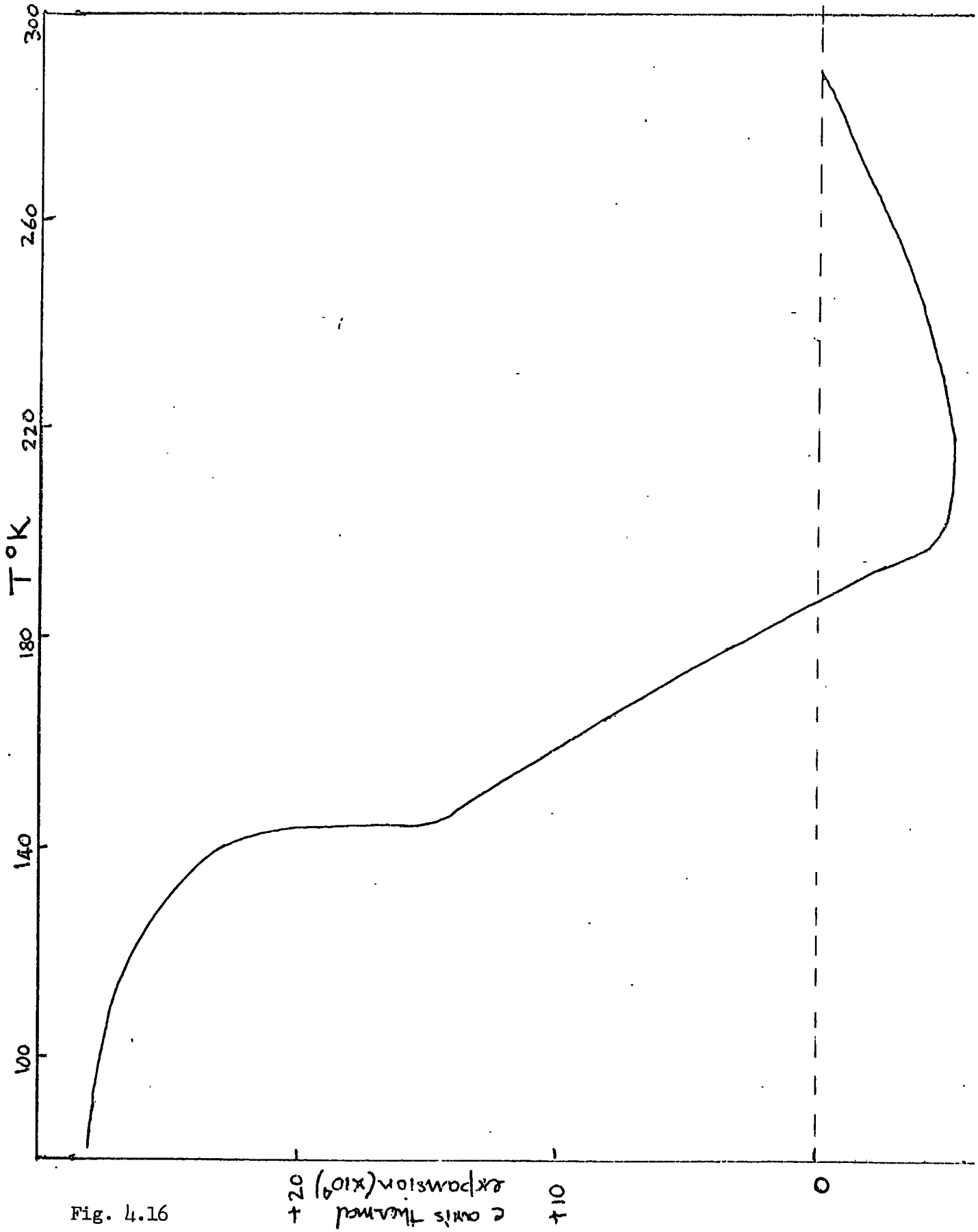
300
260
220
180
140
100
T°K
0
+10
+20
c axis Thermal Expansion (x10⁹)

Fig. 4.16

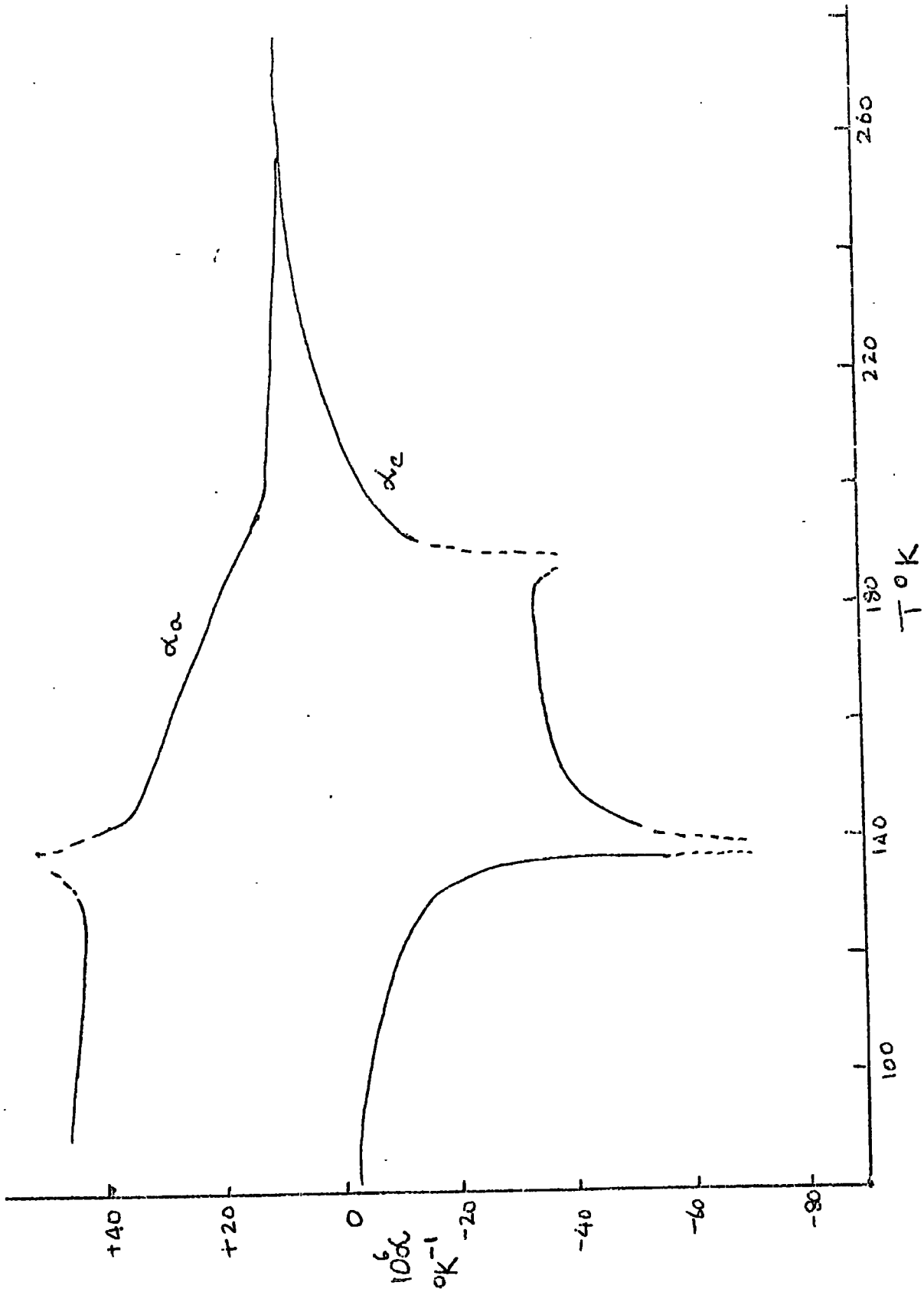
α_a
α_c
+40
+20
0
-20
-40
-60
-80
$10^6\alpha$
$^oK^{-1}$
100
140
180
220
260
T °K

Fig. 4.17

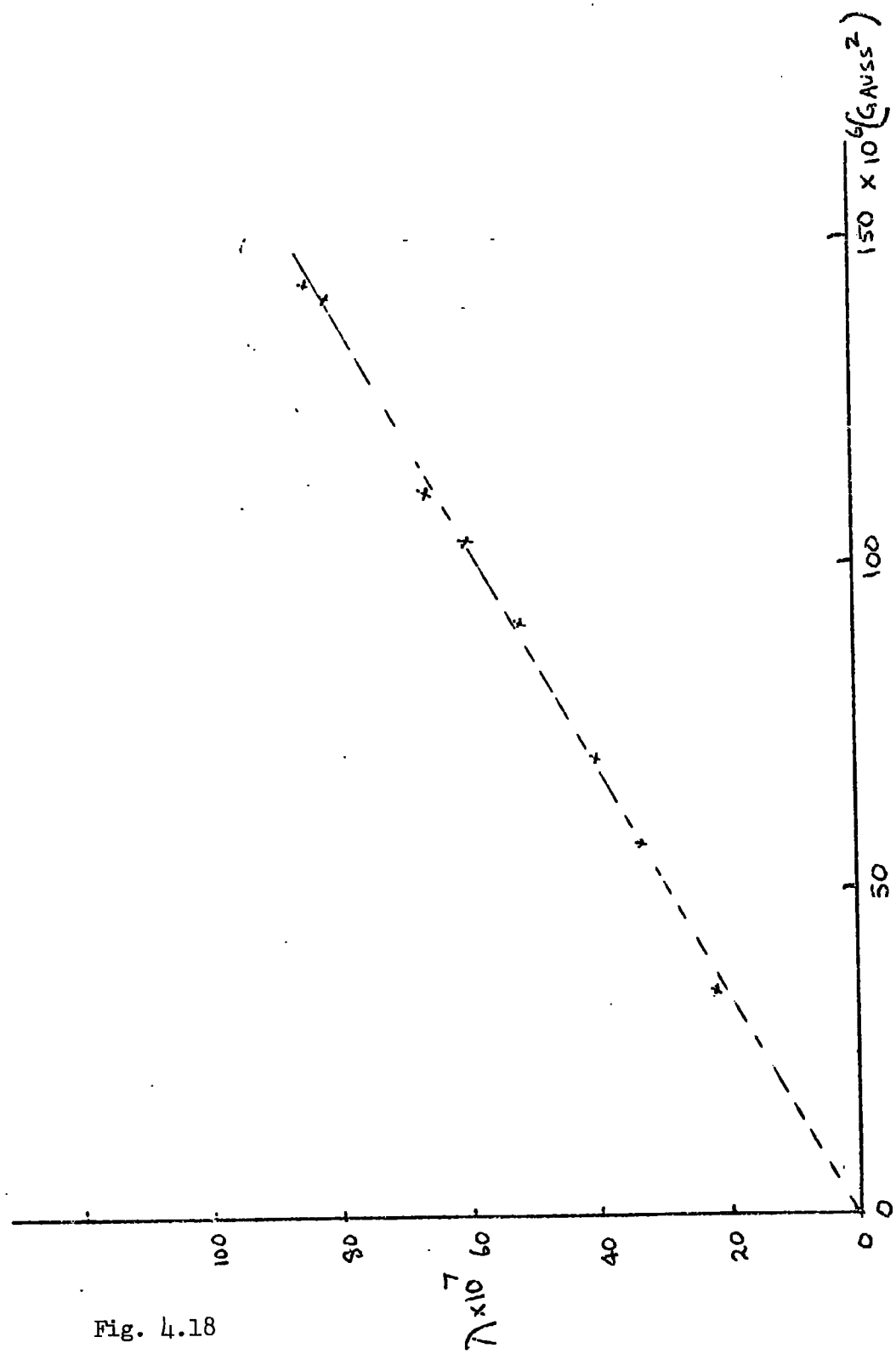

Fig. 4.18

Fig. 4.21 also shows the magnetostrain induced when the field is applied along the a direction as well as perpendicular to it.

Only one single crystal disc for $Tb_{0.695}$ $Sc_{0.395}$ could be obtained containing the basal plane. A check on the thermal expansion along the a axis was made.

CHAPTER 5

DISCUSSION

5.1 Magnetic Phase Diagram

The neutron diffraction experiments on terbium-scandium alloys conducted by Child et al.(52,53) were used to produce a magnetic phase diagram. Fig. 5.1 (p.87) shows the magnetic phase diagram of the system as deduced from the magnetic measurements. There are three regions. In the region 1 the system is paramagnetic, in the region 2 there is antiferromagnetism with the spins forming a helical system and in the region 3 the system behaves as a normal ferromagnet. As the boundary between region 2 and 3 falls sharply with composition it is not easy to define the boundary line accurately.

5.2 Variation of Ordering Temperature with de Gennes Function

The magnetic measurements have also been used to observe any correlation between the ordering temperatures and the de Gennes function for the alloys. The paramagnetic Curie points of the alloys are plotted against the effective de Gennes functions ($\bar{G}$) for the alloys on a logarithmic plot in Fig. 5.2. It is found that the paramagnetic Curie points approximately obey a $\theta_p \propto \bar{G}^{2 \pm 0.2}$ law. The heavy rare earths obey a $\theta_p \propto \bar{G}$ law and this is also approximately followed for the alloys of the heavy rare earths with yttrium. The only information available about the scandium alloys is for the Gd-Sc system as measured by Nigh et al.(51) and an inspection of their data shows that a $\theta_p \propto \bar{G}^{1.75}$ representation approximately fits the results.

As pointed out in the introductory remarks the Néel points

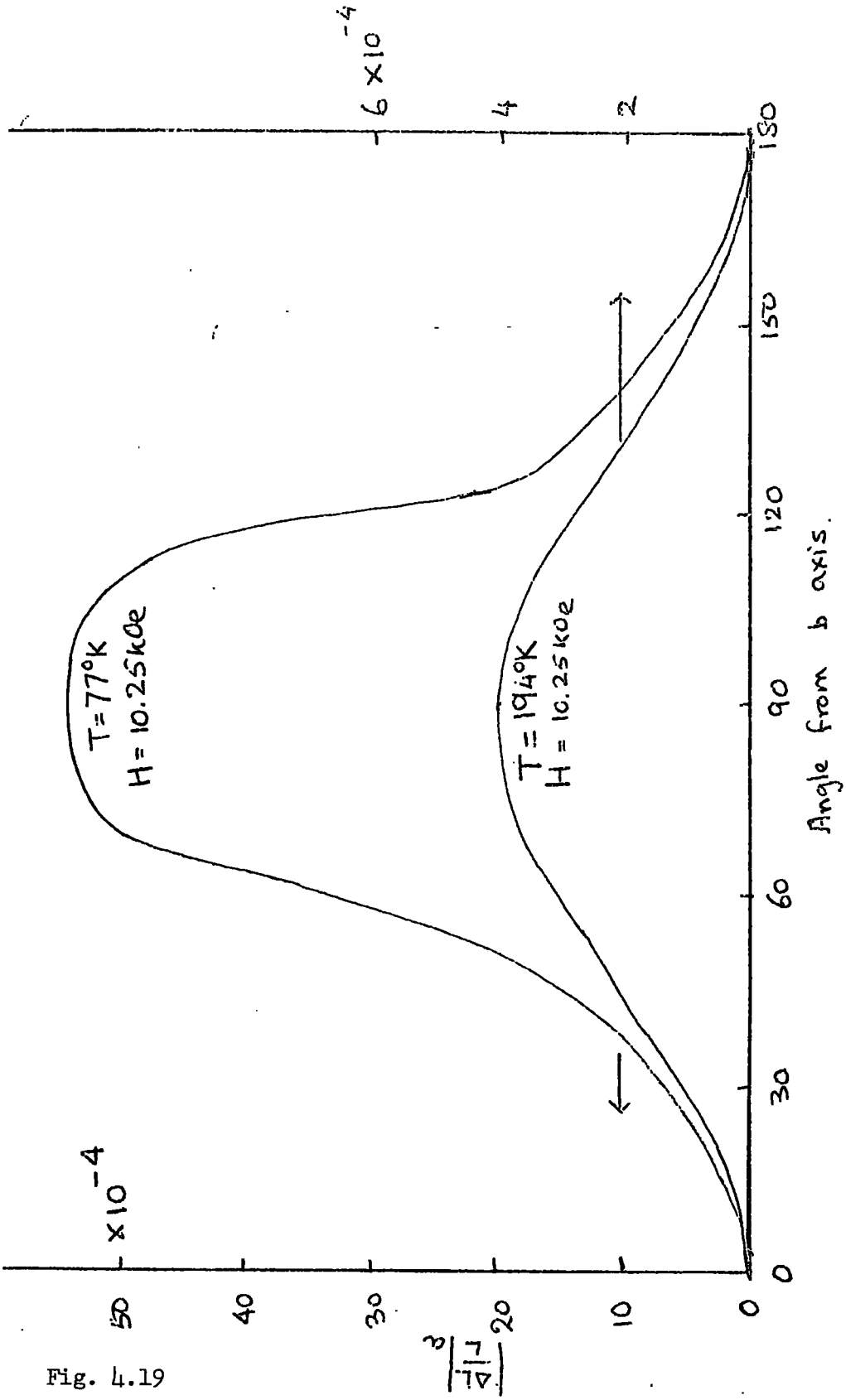
T=77°K
H=10.25kOe
T=194°K
H=10.25kOe
Angle from b axis
0
30
60
90
120
150
180
0
10
20
30
40
50
x10^-4
2
4
6
x10^-4

Fig. 4.19

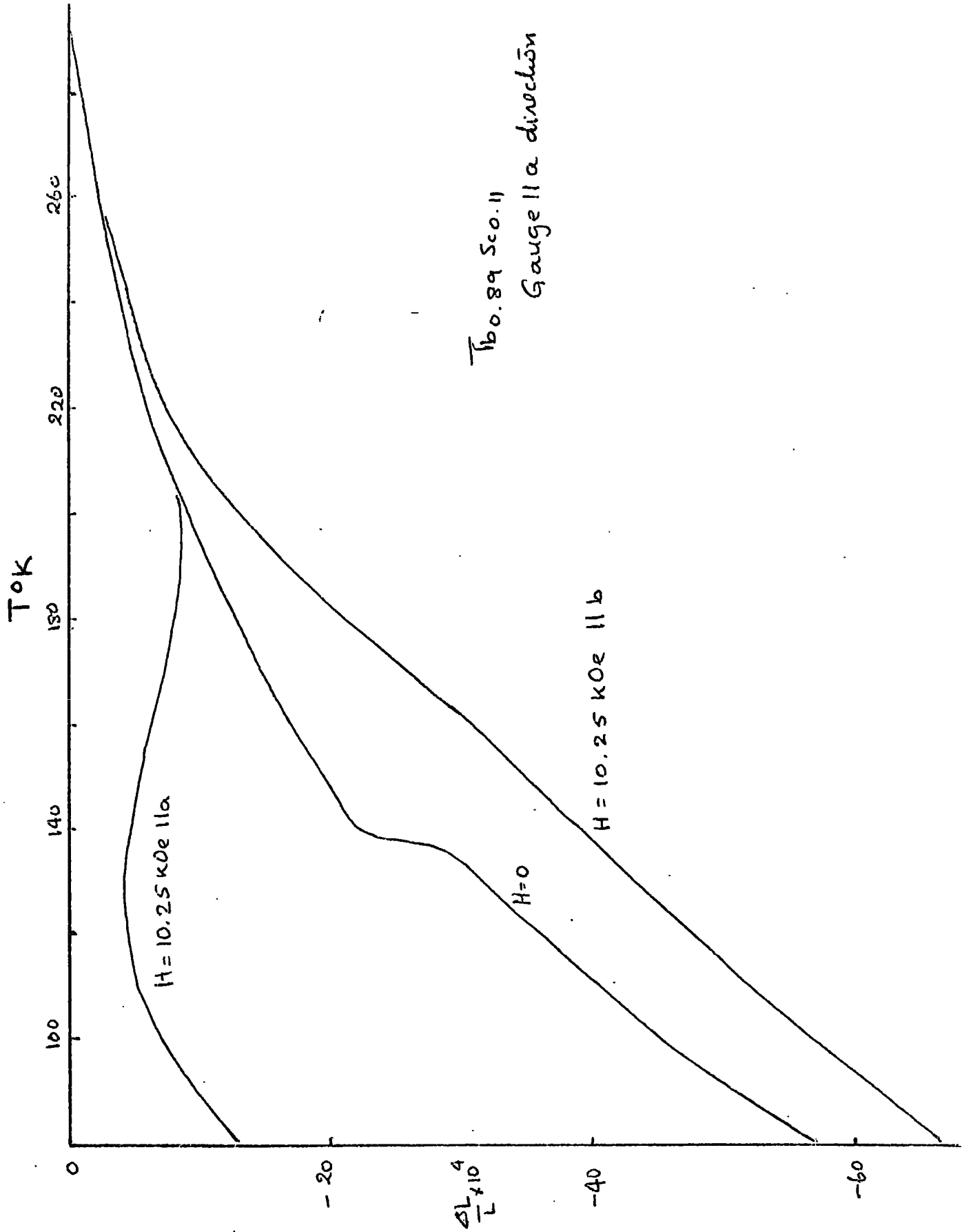
T°K
260
220
180
140
100
0
-20
-40
-60
$\frac{\Delta L}{L} \times 10^4$
H = 10.25 kOe ⊥ a
H = 10.25 kOe ⊥ b
H = 0
Tb0.89 Sc0.11
Gauge ⊥ a direction

Fig. 4.20

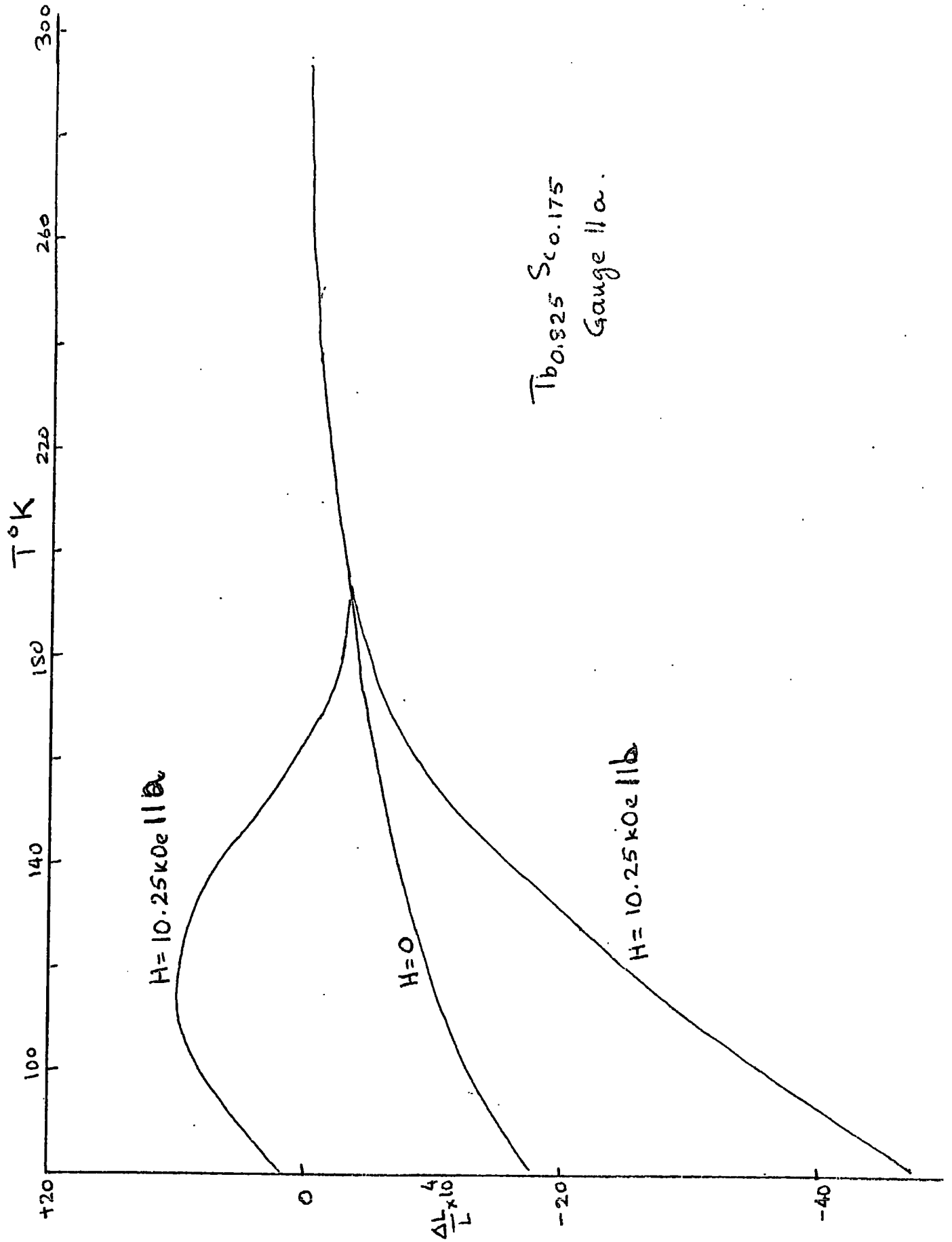
T°K
300
260
220
180
140
100
+20
0
-20
-40
$\frac{\Delta L}{L} \times 10^4$
$Tb_{0.825}Sc_{0.175}$
Gauge 11a.
H= 10.25kOe ⊥ a
H=0
H= 10.25kOe ⊥ b

Fig. 4.21

of the heavy rare earths, intra rare earth alloys and alloys between yttrium and the heavy rare earths follow a universal $T_N \propto \bar{G}^{2/3}$ law. This law is also obeyed for the Curie temperatures of some Gadolinium alloys which do not show an antiferromagnetic phase as well as for the Curie temperature of gadolinium metal itself. The Néel points of the terbium-scandium alloys are plotted against the de Gennes function in Fig. 5.3. The data can be approximately represented by a $T_N \propto \bar{G}^{1.33\pm0.05}$ law. The available data on the other rare earth-scandium systems were inspected and it was found that the $^2/_3$rd power law is not obeyed for these systems. The exponents in the $T_N \propto \bar{G}^n$ representation are found to have the values n = 1.5 for Gd-Sc, n = 1.33 for Tb-Sc and n = 1 for Ho-Sc and Er-Sc alloys. The values of n are not to be given a great deal if importance as regards their accuracies. What is important, however, is that the power law shows a monotonic variation as the heavy rare earth component is changed. The $^2/_3$rd power law is not a natural consequence of the RKKY theory. In all previous investigations of alloys containing appreciable proportions of rare earths this law has been found to be obeyed. The experiments of Nagasarra et al.(48) on the Tb-Y system containing small amounts of Tb pointed out that the $^2/_3$rd power law breaks down for the alloys containing less than 10 atomic percent Terbium and there is a limiting concentration of Tb for magnetic ordering. Similar effects are also observed in the measurements of Nelson and Legvold(82) on Dy-Y alloys.

5.3 Moments in the Alloys

From the table 4.2 we observe that the saturation magnetic moment per terbium atom in the ordered state for the two alloys

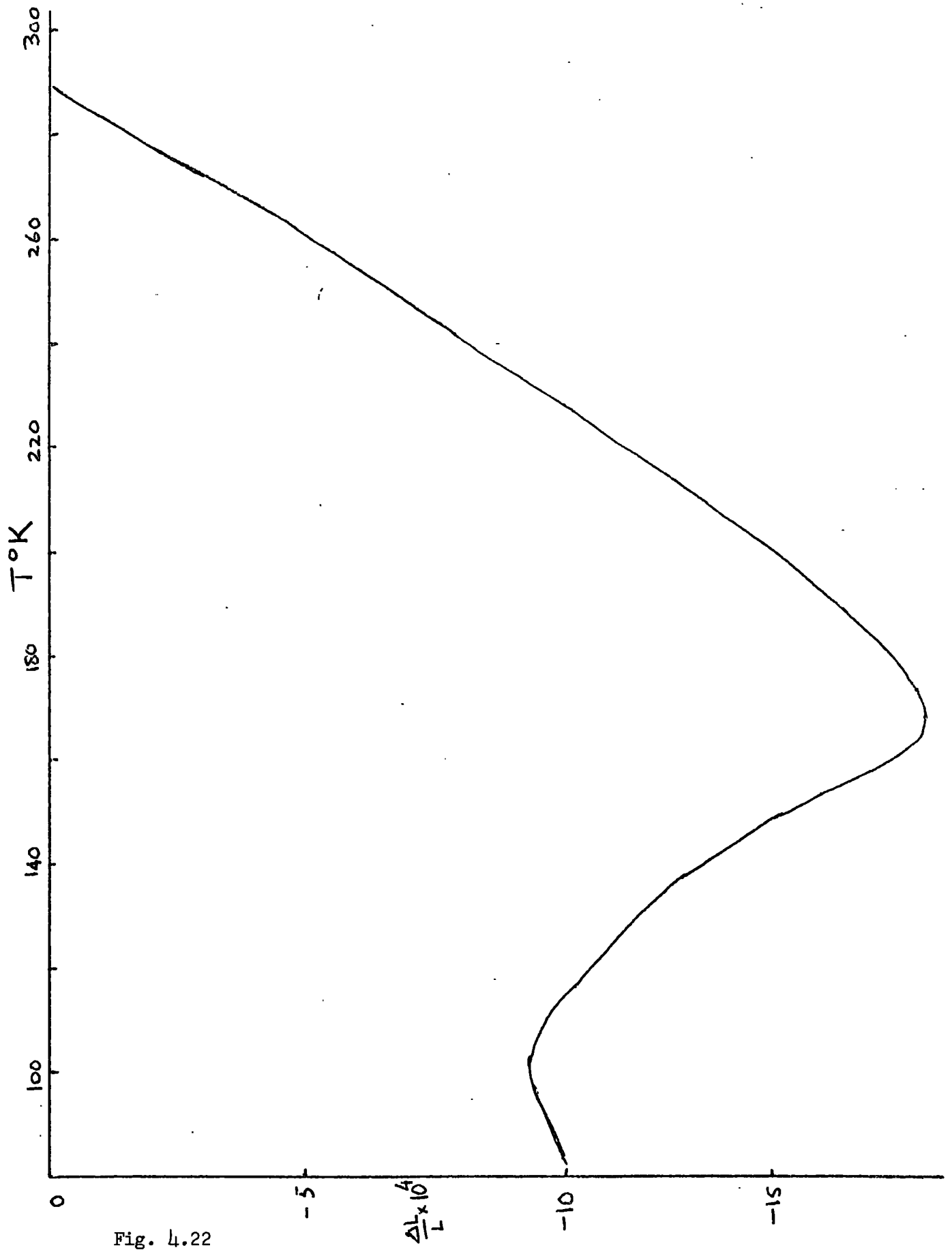

Fig. 4.22

which show the ferromagnetic phase is higher than that predicted by the gJ value. This can be attributed to a contribution by the conduction electron polarization. The effective moment per terbium ion in the paramagnetic state is also found to be higher than that predicted for the free ion. Following Weinstein's(47) treatment the room temperature values of the susceptibility may be used to obtain the value of the effective moment per terbium ion at infinite dilution. This also leads to a value of

$\mu_{eff} = (10.2 \pm 0.2)\mu_B$.

5.4 Comments on the Interaction in the Terbium-Scandium System

Wollan (55), as mentioned before, treated the observed properties of the Gd-Sc and Tb-Sc alloys with an approach based on the postulate that alloying with scandium reduces the spacing of the rare earth ions and this has the same effect as applying pressure to the system. This effectively reduces the ordering temperature. The trend in the properties of the terbium-scandium alloy is observed as this volume contraction effect would predict. McWhan et al.(83) and Milstein et al.(84) have discussed the results of high pressure experiments in terms of the RKKY model. In the molecular field model, the RKKY model does not allow for any dependence on the size of the lattice but is only a function of $^{c}/a$. The $^{c}/a$ values in these alloys do not change a great deal. So the free electron model, in a first order picture, cannot account for the observed properties in these alloys. It was also pointed out by McWhan et al.(83) that the $^{2}/3$rd power law for the Néel points is not a universal one and in their investigations dT_N/dP scaled with G. In these results,

the observed $^{4}/_{3}$rd power law and the various power laws in the other scandium alloys point to the fact that these power laws may be related to the contraction of the lattice. To show that the exponents have a monotonic dependence on the rare earth component, we plot the exponents as a function of the atomic No. as shown in Fig. 5.4. Specht(41) pointed out that a change in the free electron Fermi wave number causes appreciable changes in the ordering characteristics. From a free electron model, the Fermi wave number will change appreciably as scandium is alloyed with terbium. This may be the reason why the ordered structure is not observed even for high terbium concentrations. There have been suggestions as well that the absence of ordering may be due to the fact that each terbium ion may not have two nearest neighbour terbium ions to maintain long range order. But at 25% terbium concentration the probability of the nearest neighbour terbium ions is high. Alternately as Nagasawa et al.(49) suggested it may be due to a mean free path effect. In this scheme the conduction electron polarization may for some reason lose its memory before it gets to the next terbium ion to sustain the ordering and thus reduce the interaction. But it is unlikely to be the reason for the absence of long range interaction in the alloys with a high proportion of terbium. The interaction between the ions in these alloys, in the RKKY model, depends on the conduction electron susceptibility which is referred to as $\chi(q)$ in the literature. Appropriate theories have not yet been developed to take care of the variations in $\chi(q)$ due to the complex band structures and the effect which will be produced by

compression. The addition of scandium may produce changes in $\chi(q)$ which will cause the absence of ordering in the alloys. The Fermi surface should also show complicated changes over the sequence and this will be reflected in the $\chi(q)$ and thus in the ordering of these alloys.

5.5 Exchange Constants and their Variation

The magnetization measurements for the two alloys which showed ferromagnetic phases were used to obtain the data on the variation of critical field with temperature as shown in Figs. 4.6 and 4.12. This data in conjunction with the data on turn angle variation with temperature for a $Tb_{0.9}Sc_{0.1}$ alloy supplied by Dr. H.R. Child(85) of Oak Ridge laboratories were used to evaluate the exchange constants J_1 and J_2 for the $Tb_{0.89}Sc_{0.11}$ alloy. It must be emphasised that importance must be laid on the trend rather than the precise values of J_1 and J_2. Fig. 5.5 shows a plot of the exchange constants J_1 and J_2 derived using formulae (2.10) and (2.12) for the $Tb_{0.89}Sc_{0.11}$ alloy. The thermal expansion measurement on the same alloy along the c axis can be used to evaluate the lattice parameter at these temperatures and plot the exchange constants as functions of the c axis spacing as shown in Fig. 5.6. A comparison of these results with those in ref. 2.9 shows the similarity of the effects. This shows the strong dependence of the exchange constant on the details of the helix.

The above treatment following the simplest model obviously has the scope for improvement. In itself the simple model has got no way of catering for the variation of

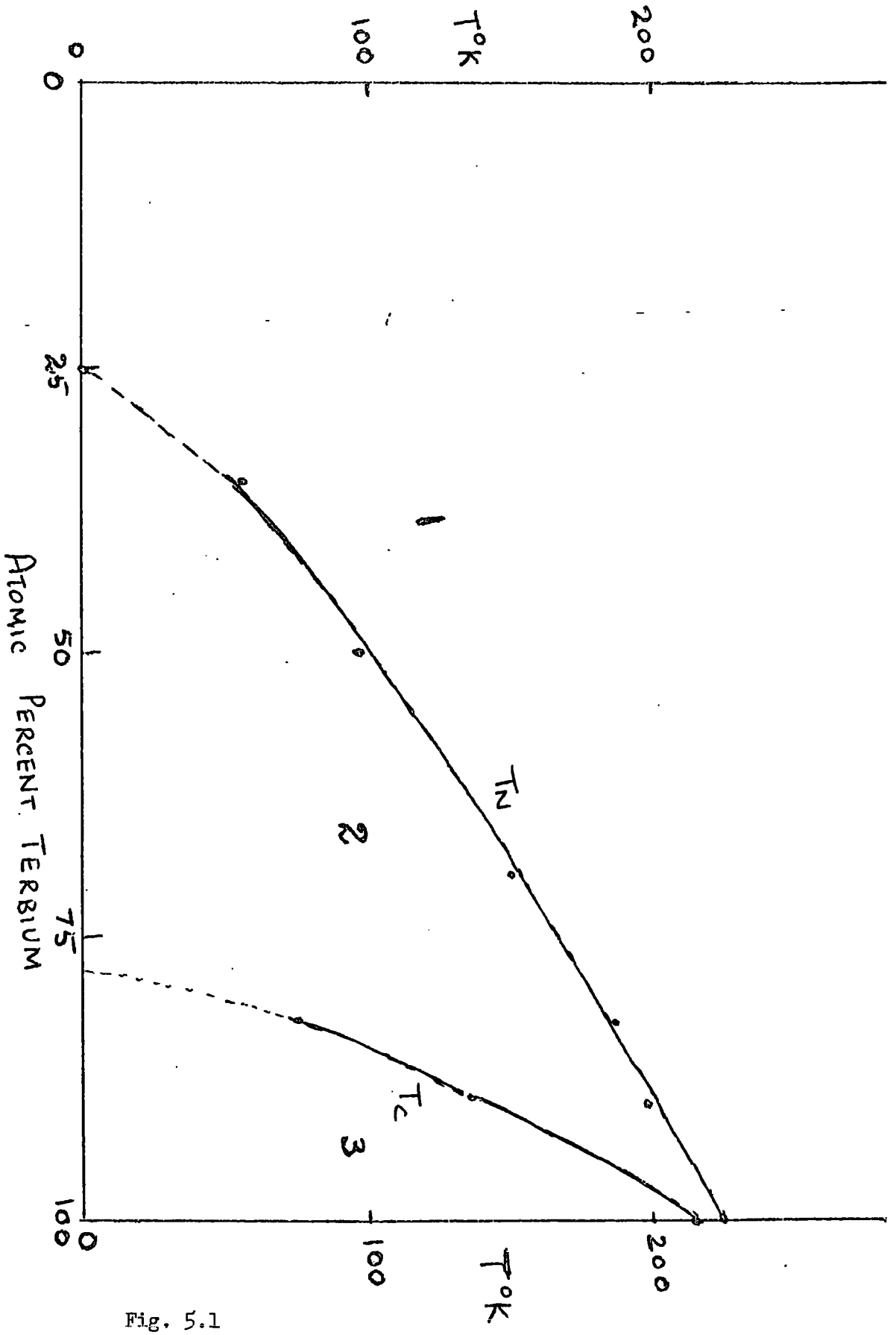
0
100
T°K
200
0
25
50
75
100
ATOMIC PERCENT TERBIUM
1
2
3
TN
TC
0
100
200
T°K

Fig. 5.1

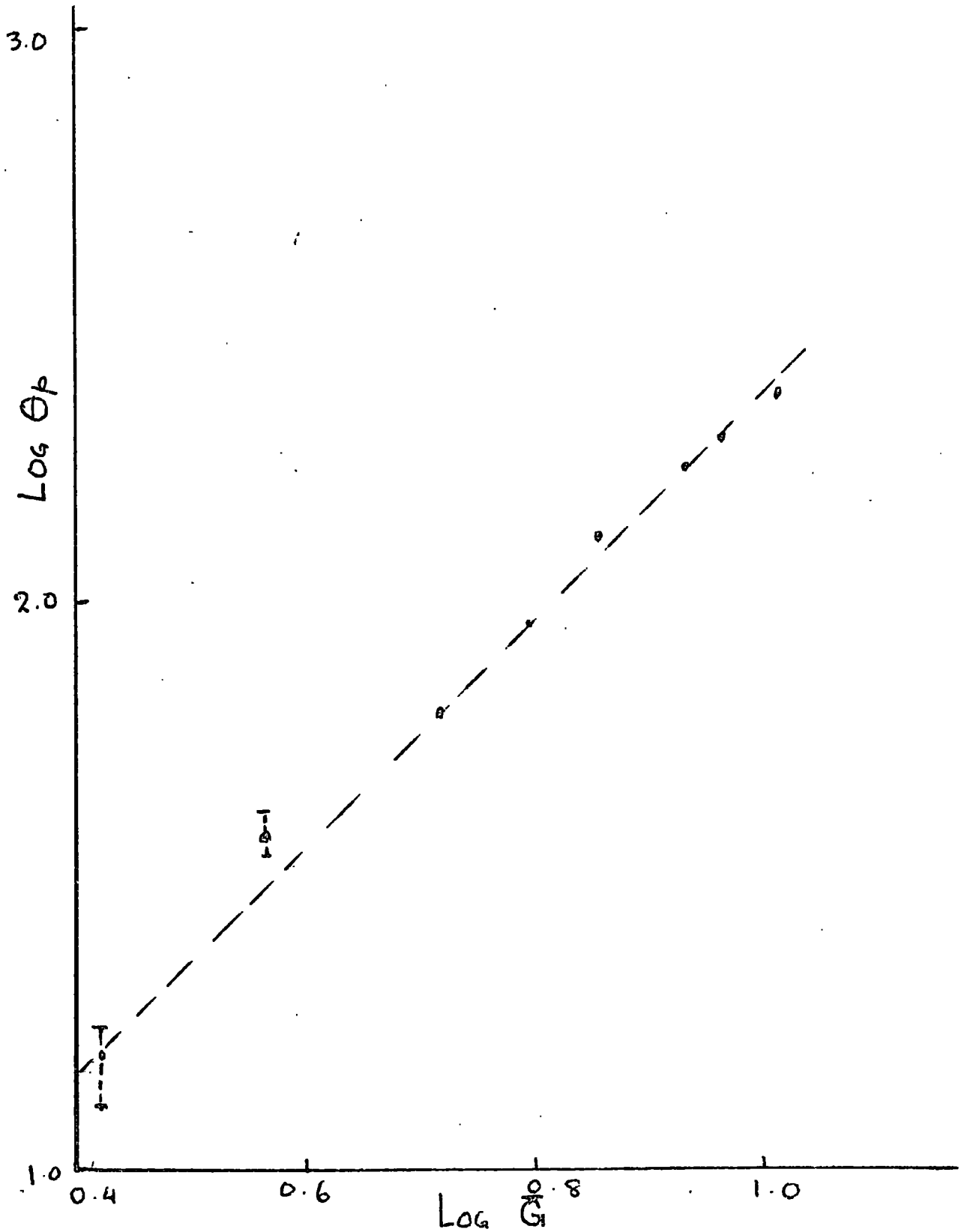

Fig. 5.2

the exchange constants J_1 and J_2 with temperature intrinsically. It is obvious that J_1 and J_2 which arise from the RKKY interaction will have a dependence on the interplanar spacing along the axis of the hexagon. Darnell et al (86) used this concept following the discussion in Jarrett et al. (87).

Landry and Stevenson (88) used a similar term in their analysis of their attempt to account for the temperature variation of the turn angle. Lee (89) included the variation of both J_1 and J_2 with the c axis parameter. Following Lee's analysis the energy of a helical spin system as expressed in eqn.(2.8) is modified to

$$E_{ex} = \tfrac{1}{2} \frac{(c - c_o)^2}{c_o^2} Y - M_s^2 \left(J_1(0) + \frac{dJ_1}{dc}(c-c_o) \right) \cos\theta$$

$$- M_s^2 \left(J_2(0) + \frac{dJ_2}{dc}(c-c_o) \right) \cos 2\theta \qquad \ldots (5.1)$$

where c_o is the equilibrium interlayer separation, Y the Young's modulus and the other symbols have the same significance as in eqn.(2.8). On minimization of the energy, i.e. applying the condition $\frac{\partial E_{ex}}{\partial c} = 0$, the equilibrium c axis strain can be represented by

$$\left.\frac{\Delta L}{L}\right|_c = \frac{c M_s^2}{Y} \left(\frac{dJ_1}{dc} \cos\theta + \frac{dJ_2}{dc} \cos 2\theta \right). \qquad - (5.2)$$

From the experimental data on $Tb_{0.89}Sc_{0.11}$, the c axis magnetostrain in conjunction with the magnetization and turn angle values have been used to estimate $1/Y \frac{dJ_1}{dc}$ and $1/Y \frac{dJ_2}{dc}$.

These have the values

$$1/Y \frac{dJ_1}{dc} = 0.023 \ \text{cm}^2/\text{erg}$$

and $^{1}/_{Y}\ \frac{d\beta_2}{dc} = -0.010$ cm^2/erg

Similar analyses have been made by Rhyne et al.(90) for holmium and Landry's(91) treatment of dysprosium is based on a model which is a modification of Lee's model. It is to be stressed that the importance of this analysis is to provide an indication of the relative magnitudes of $\frac{d\beta_1}{dc}$ and $\frac{d\beta_2}{dc}$ and the numbers are not precise. No parameter for Y is used as the relative magnitudes are of interest. The ratio $\alpha = \frac{d\beta_1/dc}{d\beta_2/dc}$ has been estimated by Palmer (92) for dysprosium and holmium from elasticity measurements and he obtained values not widely different from those given by this model. The value of α for $Tb_{0.89}Sc_{0.11}$ falls between those of dysprosium and holmium.

From the values of β_1 and β_2 as functions of the c axis lattice parameter an estimate of α may be made. The value obtained is ~3 as compared to 2.3 from the above analysis.

Lee also pointed out that the basal plane strain induced when a system is in the helical state may be due to the effect of the c axis strain. The c axis expands in the antiferromagnetic region and this magnetostrain may cause a contraction in the basal plane. This would cause the c and a axis strains to be related through a 'magnetic Posson's ratio' as defined by

$$\lambda_a = -\rho\lambda_c$$

An estimate of the value of ρ has been made for $Tb_{0.89}Sc_{0.11}$ between the two transition temperatures T_C and T_N. In Fig. 5.7 the value of ρ is plotted against T and it is observed

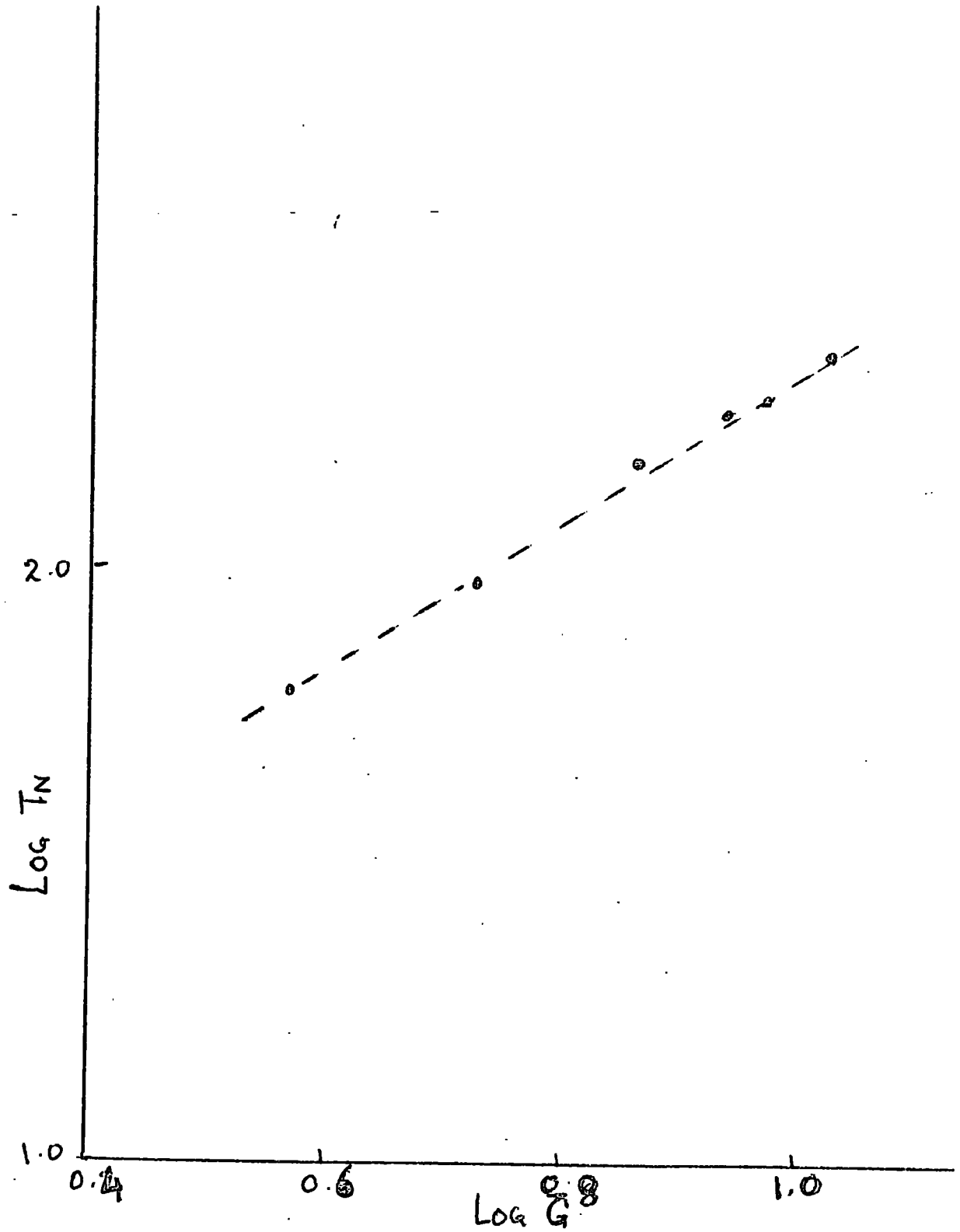

Fig. 5.3

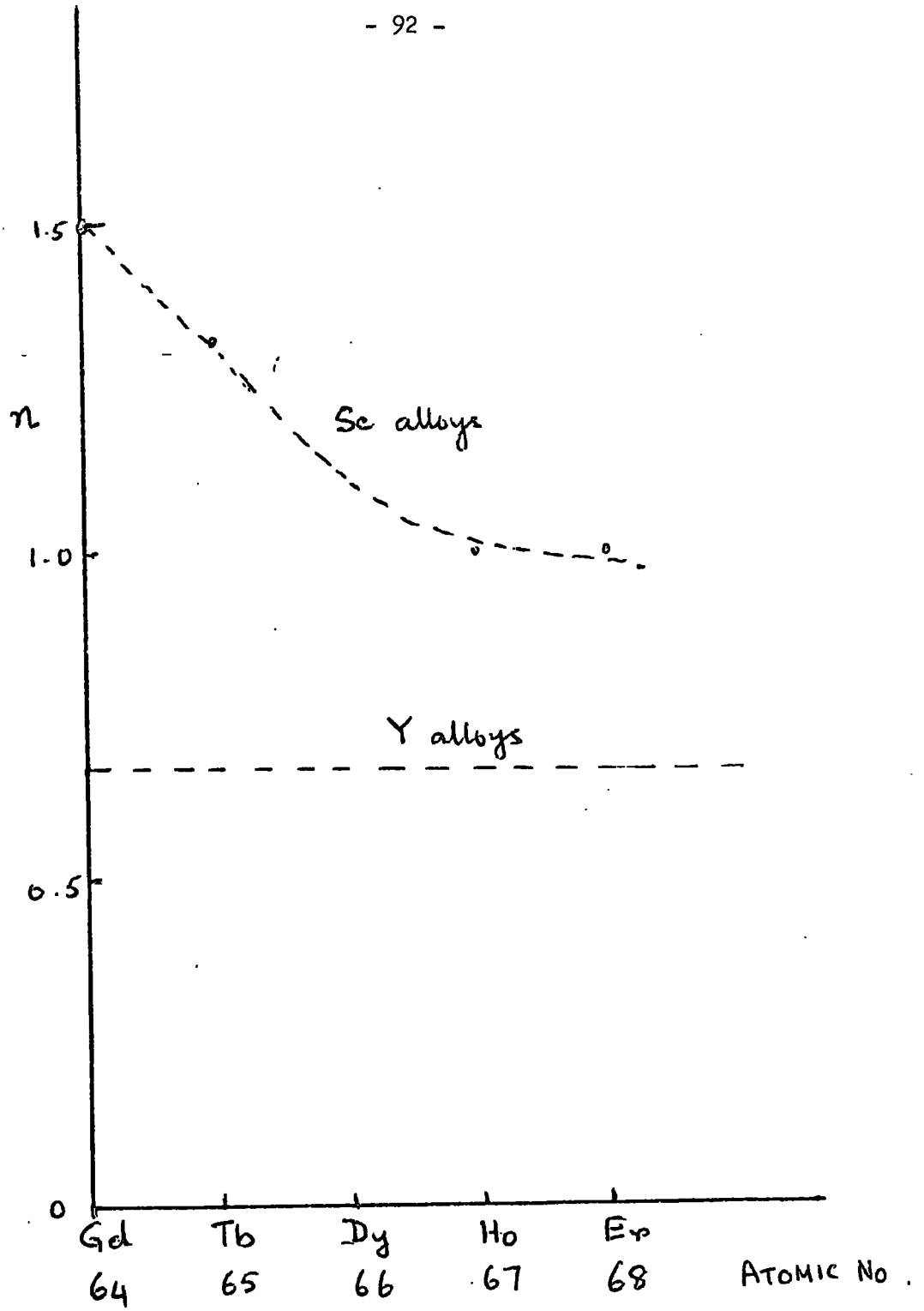
1.5
n
1.0
Sc alloys
Y alloys
0.5
0
Gd
Tb
Dy
Ho
Er
64
65
66
67
68
ATOMIC No.

Fig. 5.4

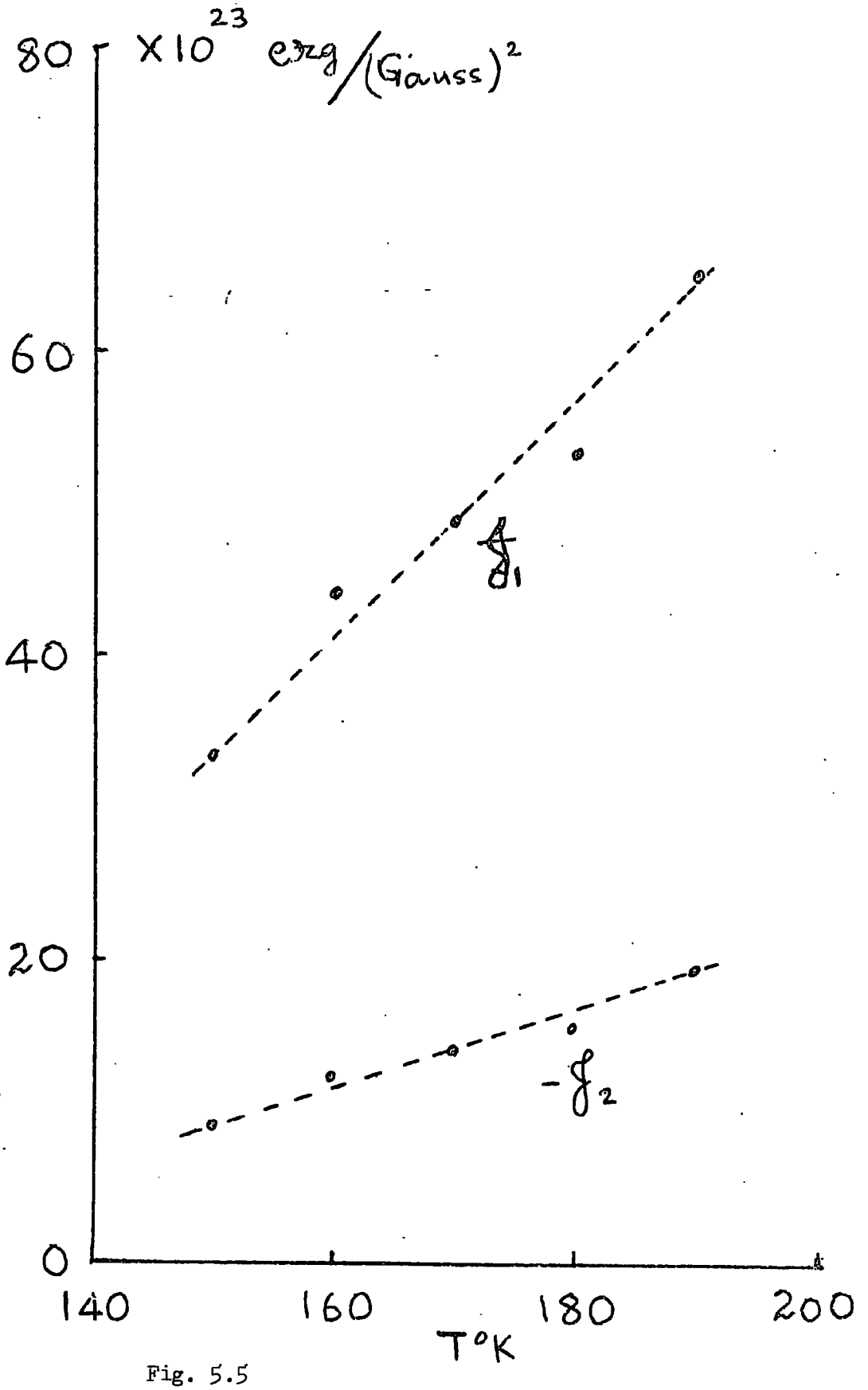

Fig. 5.5

that ρ stays reasonably constant between 150°K and 180°K and only departs from this character near T_N. So it seems that the basal plane strain is due to the axial stresses in the helical region.

The two constant model for the helical spin structure has been used in this analysis following the treatment of similar systems. Bjerrum Møller et al.(93), however, have used a four constant model to fit inelastic neutron scattering experiment results on the ferromagnetic phase of terbium. A four constant model is obviously far more complicated and does not lead to immediate simple solutions as does the two constant model. More experimental results on the spin wave dispersion curves in different systems would provide us with further information about the limitations of the two constant model.

5.6 Estimate of the Magnetostrictive Energy

It was pointed out in the introduction to the magnetostriction measurements that it was of interest to estimate the contribution of the magnetoelastic energy in these alloys. Figs. 5.8 and 5.9 show the variations of the $\lambda^{\gamma,2}$ parameter for $Tb_{0.89}Sc_{0.11}$ and $Tb_{0.825}Sc_{0.175}$ alloys with temperature. The experimental curves fit in reasonably well with the single ion expression of Callen and Callen. From the extrapolation of the $\lambda^{\gamma,2}(T)$ curve a value of $\lambda^{\gamma,2}$ at T = 0°K can be estimated. The magnetoelastic energy can be derived from the $\lambda^{\gamma,2}$ term with the use of the symmetry elastic constant c^{γ}. There is no experimental data for c^{γ} available for these alloys.

An attempt has been made to estimate the value of c^{γ} from the available data on the heavy rare earths. The single crystal elastic constants for some rare earths (Dy, Ho, Gd and Er) have been measured by various workers (92,94-95). The attempt to derive the values for the terbium-scandium alloys from these measurements is obviously open to criticism. In the absence of any other means the de Gennes function and the ordering temperatures of the alloys have been considered as two criteria to correlate them with the heavy rare earths. A plot of c_{11} and c_{12}, the elastic constants which give the value of c^{γ}, against the atomic number of the rare earths was made. The ordering temperatures of the heavy rare earths were also plotted as a function of the atomic number and an appropriate effective atomic number was alloted to each of terbium-scandium alloys compatible to their ordering temperatures. This effective atomic number was then used to obtain a value of c_{11} and c_{12} and consequently c^{γ}. In view of the simplicity of this approach no account of the temperature dependence of the elastic constants was taken (up to 20% in case of Palmer's data). The estimated values of the c^{γ} constant for the alloys were

$$c^{\gamma}(Tb_{0.89}Sc_{0.11}) = 20 \times 10^{4}\ {}^{o}K/atom$$

and $$c^{\gamma}(Tb_{0.825}Sc_{0.175}) = 22 \times 10^{4}\ {}^{o}K/atom$$

and the values of the energy obtained for the two alloys were

$$E_{ms}(T = 0^{o}K) = 1.25^{o}K/atom \quad \text{for } Tb_{0.89}Sc_{0.11}$$

and $$E_{ms}(T = 0^{o}K) = 0.8^{o}K/atom \quad \text{for } Tb_{0.825}Sc_{0.175}$$

From Cooper's(33) analysis of the terbium results it is found that the corresponding energy for pure terbium is $2^{o}K/atom$. Comparing these values, it can be seen that the magnetoelastic energy is falling rapidly with the addition of scandium to

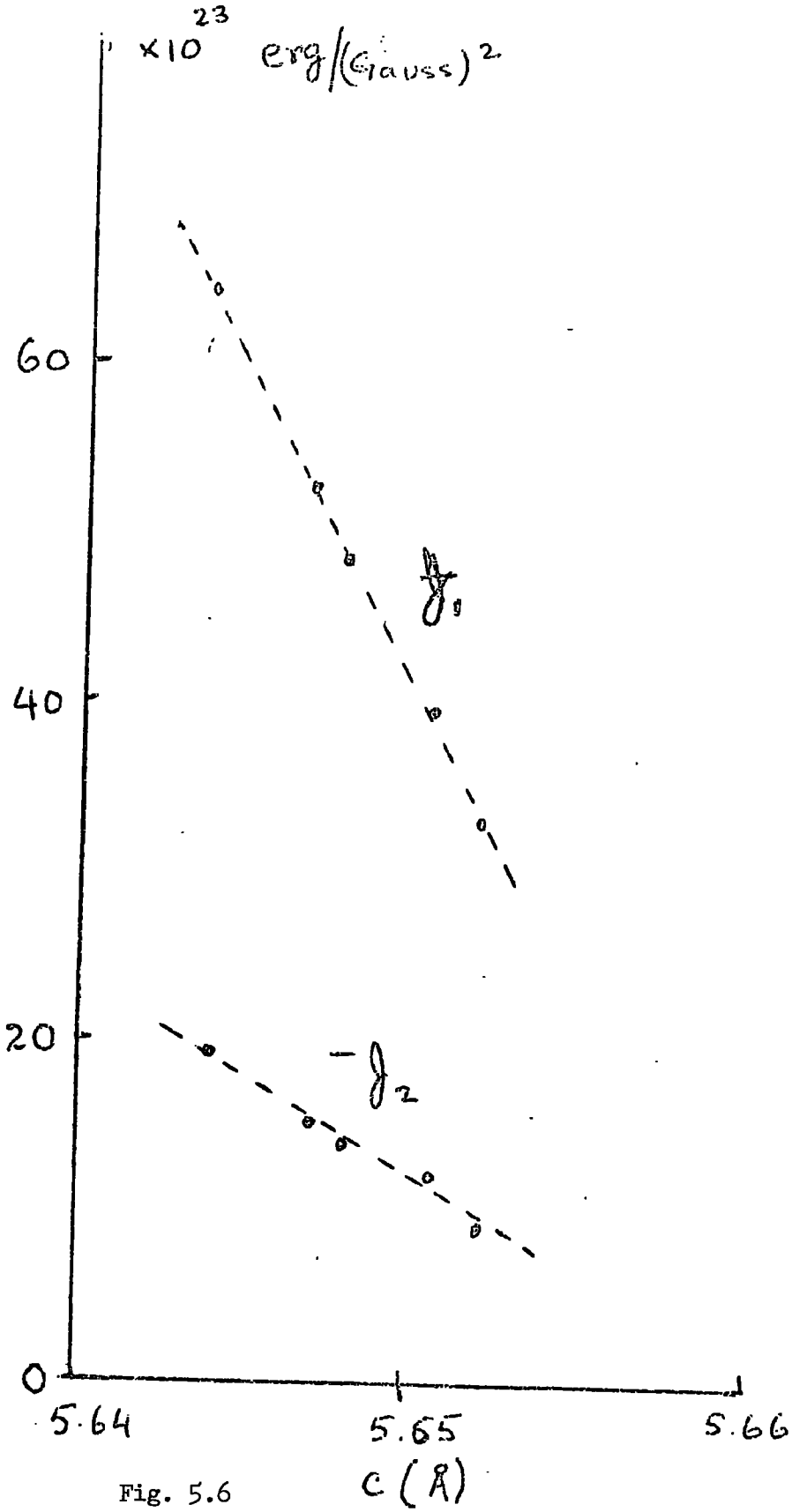

Fig. 5.6

terbium as shown in Fig. 5.10. If we assume that the driving force from the helical antiferromagnetic state to the conventional ferromagnetic state is provided by the magnetostriction, then the ferromagnetic phase will be absent in alloys with quite high concentrations of terbium as the extrapolation of the line in Fig. 5.10 goes to zero for an alloy containing about 75 atomic percent terbium.

In order to find out whether the variation of the driving energy as defined in eqn.(2.23) by

$$\Delta = E_{helical} \sim E_{ferromagnetic}$$

followed the same dependence on temperature as the magnetostrictive energy over the helical spin arrangement range, a plot for Δ against the reduced magnetization on a logarithmic scale was made for the $Tb_{0.89}Sc_{0.11}$ alloy. It is found that the function

$$\frac{\mathcal{J}_1(1 - \cos\theta)^2}{M_o \cos\theta} - \frac{H_c}{M}$$ follows a

M^4 dependence within the accuracy of this scheme as shown in Fig. 5.10. The magnetostrictive energy derived from the $\lambda^{\gamma,2}$ values plotted in Fig. 5.11 shows an approximate M^6 dependence as the temperature is raised. Since Δ is related to the driving energy as $E_{driving} = M^2 \Delta$, it can be concluded that the M^6 dependence is also obeyed in the case of the driving energy. As discussed by Feron et al(67) anisotropy energy and elastic energy terms should also be considered for their contributions to the Δ term. But in the temperature range where the antiferromagnetic arrangement occurs the contribution due to anisotropy can be considered to be small and the change in the elastic

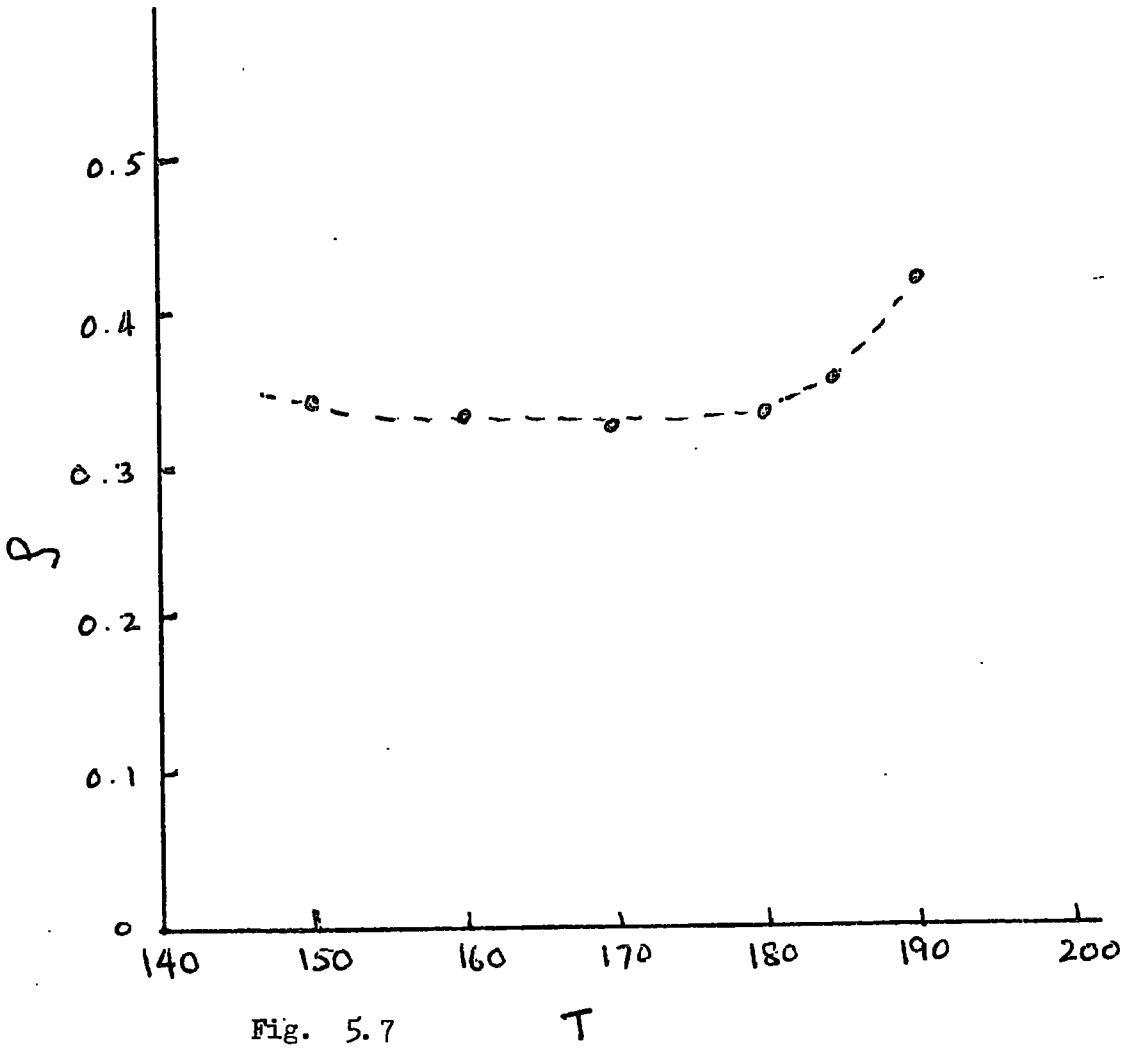

Fig. 5.7

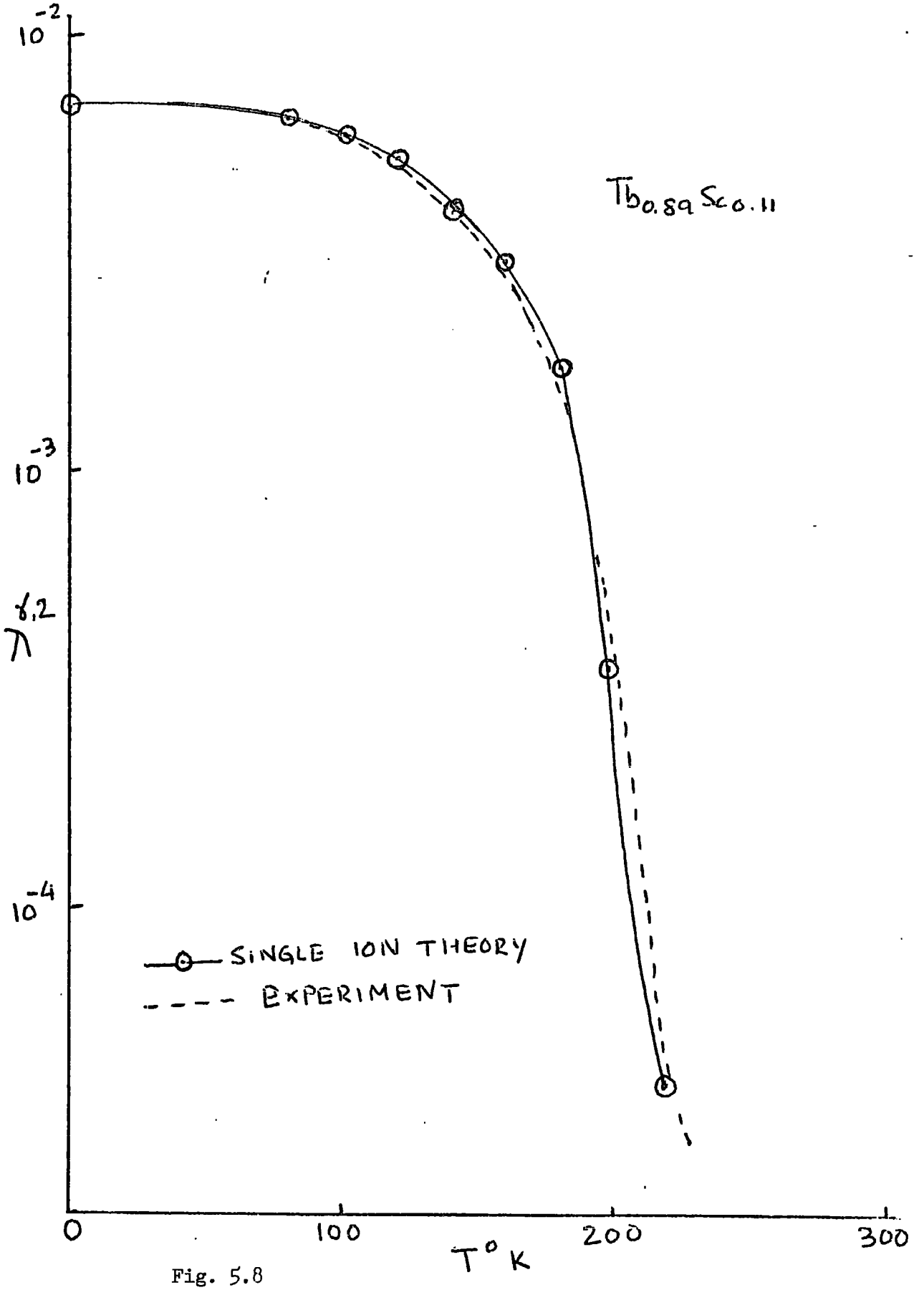
10^{-2}
10^{-3}
10^{-4}
$\lambda_{1,2}$
$Tb_{0.89}Sc_{0.11}$
SINGLE ION THEORY
EXPERIMENT
0
100
200
300
T°K

Fig. 5.8

energy will also be small from the inspection of the available data on the heavy rare earths.

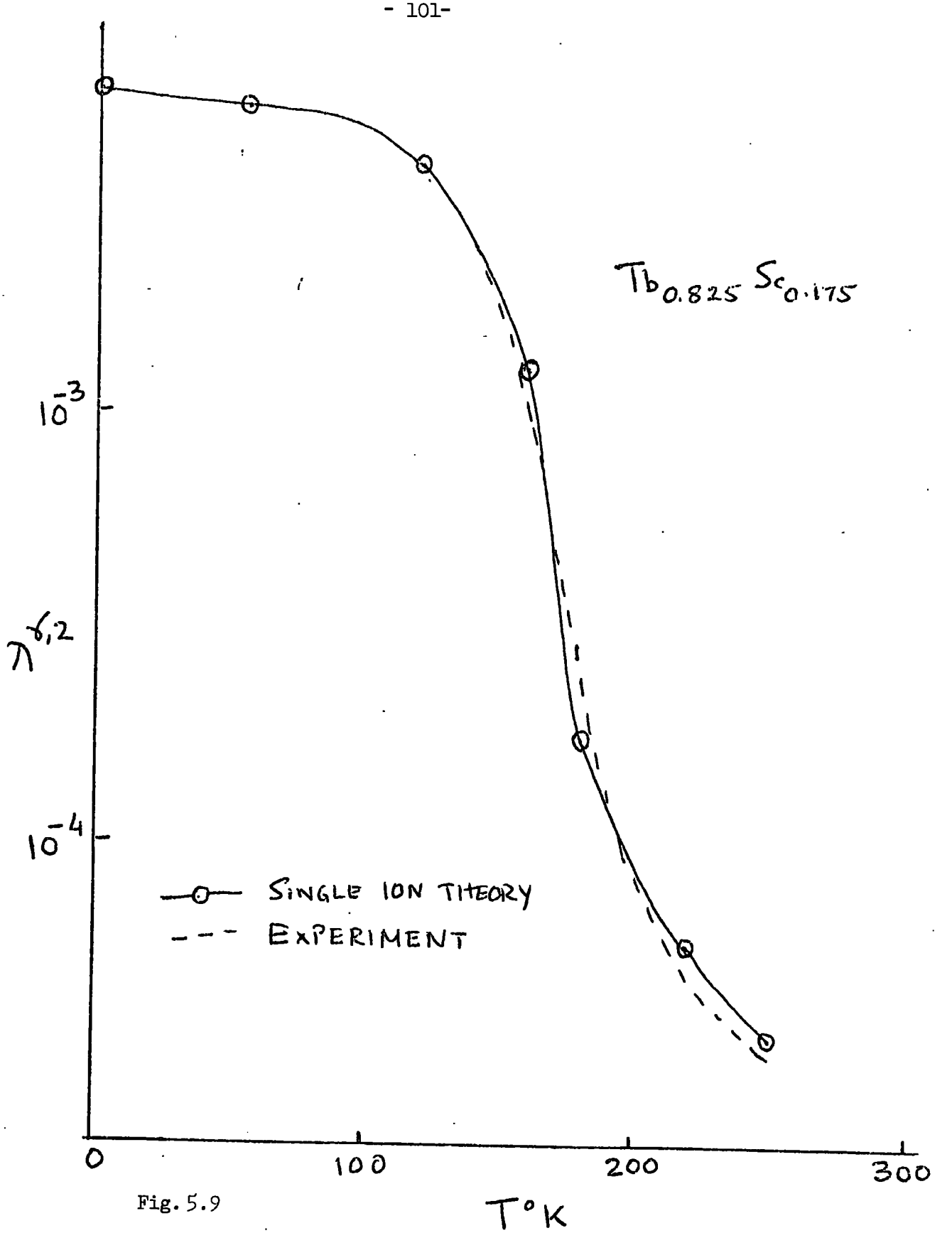
$Tb_{0.825}Sc_{0.175}$
10^{-3}
$\lambda^{6,2}$
10^{-4}
SINGLE ION TITEORY
EXPERIMENT
0
100
200
300
T°K

Fig. 5.9

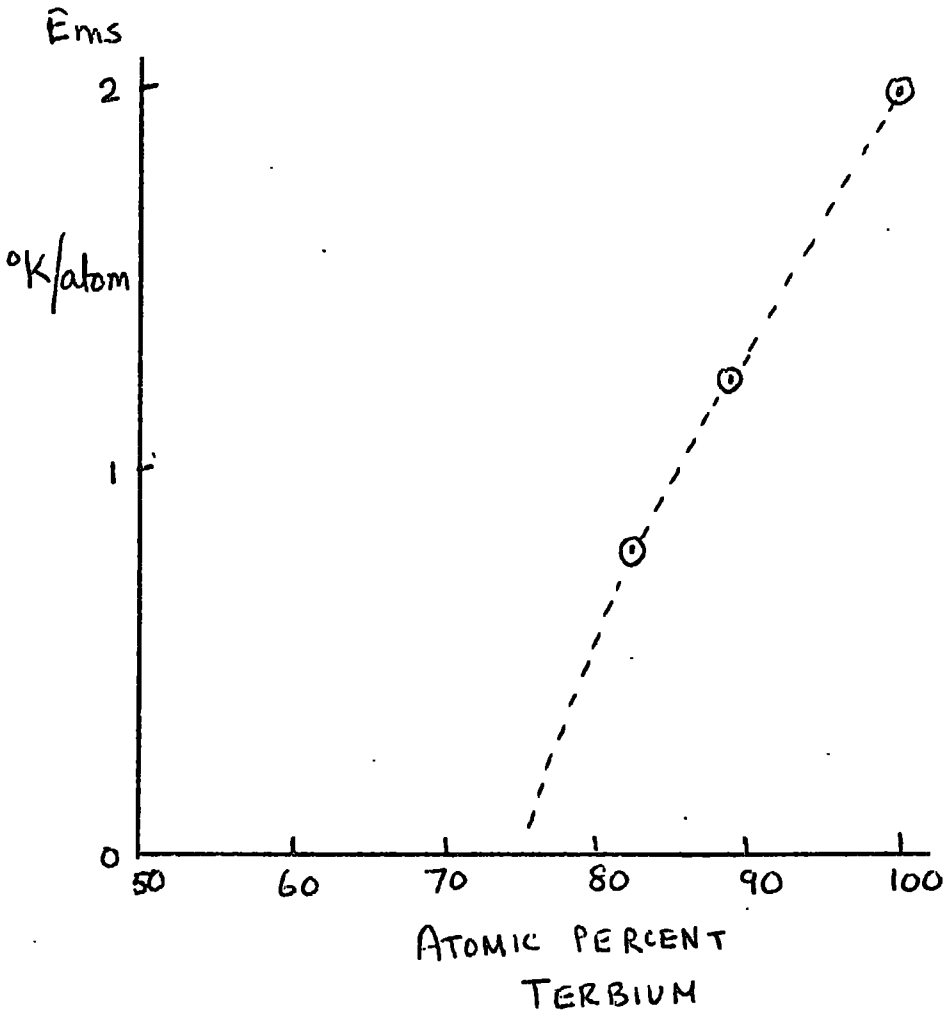

Fig. 5.10

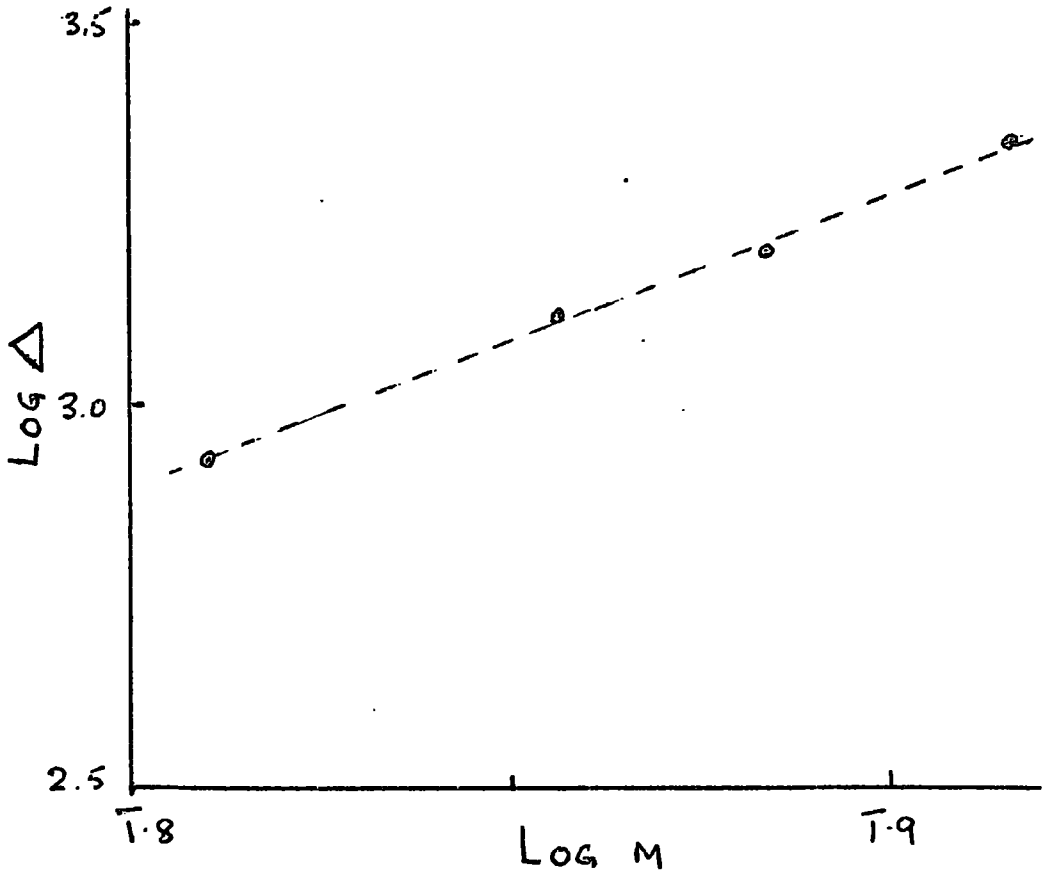

Fig. 5.11

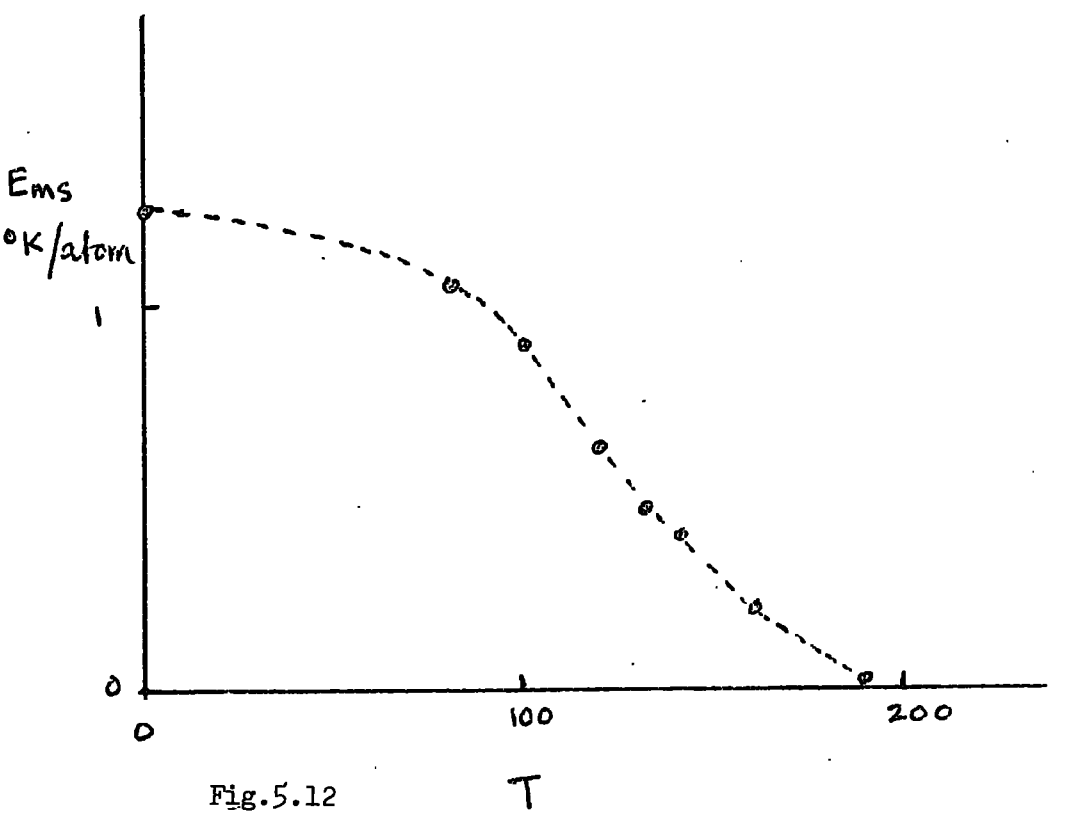

Fig.5.12

CHAPTER 6

6.1 Summary

The neutron diffraction measurements on the terbium-scandium alloys pointed to significant differences in the properties from those of the terbium-yttrium alloys. Magnetic measurements on the terbium-scandium alloys substantiate these findings. It is found that the paramagnetic Curie points follow a higher power dependence on the effective de Gennes function ($\theta_p \propto \bar{G}^2$) in contrast to the linear variation found for the terbium-yttrium alloys. It is also found that the Néel points follow a $T_N \propto \bar{G}^{4/3}$ law for the series as opposed to the $T_N \propto \bar{G}^{2/3}$ law, which is followed by all the alloys of heavy rare earths with yttrium and the intra rare earth alloys. These differences are attributed to possible changes in the interaction due to the contraction of the lattice. Since a simple model of the RKKY interaction does not cater for any variations due to changes in lattice spacings, it is possible that the interaction is changed by a change in the Fermi wave number or changes in $\chi(q)$, the conduction electron susceptibility.

The magnetostriction and thermal expansion measurements on single crystals of alloys of compositions $Tb_{0.89}Sc_{0.11}$ and $Tb_{0.825}Sc_{0.175}$ have been used to estimate the magnetostrictive energy and this energy falls off rapidly with the addition of scandium to terbium. If the ferromagnetic ordering is due to the magnetostriction in the system, the absence of a ferromagnetic phase, even in alloys with a high proportion of terbium,

If the ferromagnetic ordering is due to the magnetostriction in the system. the absence of ferromagnetic phase, even in alloys with a high proportion of terbium, will be accounted for by the fall off in the magnetostrictive energy.

An estimate of the interlayer exchange constants and their derivatives has also been made for the $Tb_{0.89}Sc_{0.11}$ alloy with the help of turn angle data provided by Dr. H.R. Child of the Oak Ridge Laboratories. They have the same qualitative variation as the heavy rare earths (e.g. Dysprosium).

6.2 Suggestions for Further Work

There are several interesting features in these alloys which need attention. Single crystals in the critical composition range (73-77 atomic percent terbium) will provide more information about the ferromagnetic-antiferromagnetic transition. Elastic constant measurements over the whole range of composition will be useful to permit estimation of the energy terms accurately. To get a better idea of the energy in the ordered state the anisotropy contribution needs to be taken into account. Experiments to obtain these constants should provide useful information.

Inelastic neutron diffraction experiments will be very useful in obtaining the exciton spectra and will be of great help in the understanding of the system. If very pure materials are available, Fermi surface measurements will be interesting to observe the effects of the contraction of the lattice. This may provide us with an answer to the nature of the interactions in these alloys.

APPENDIX I

Stereographic Projections for Hexagonal Crystals

Standard projections for the three principal directions in hexagonal crystals were necessary in course of these investigations. The (0001) projection is available from any standard book (e.g. ref. 75), but the $(11\bar{2}0)$ and $(10\bar{1}0)$ projections were not obtainable directly. Koepke and Scott's work (ref. 74) mentions these but no projections are produced.

A simple computer programme to work out the angle between the planes (h k l) and h'k'l'), where the indices were varied from 0 to 3, was used. Figs. A1 to A3 show the standard projections for the three principal directions on standard Wulff nets. These projections are for the $^{c}/_{a}$ value of 1.58. This is useful for most heavy rare earths and their alloys. It is not difficult to plot these for other values of $^{c}/_{a}$.

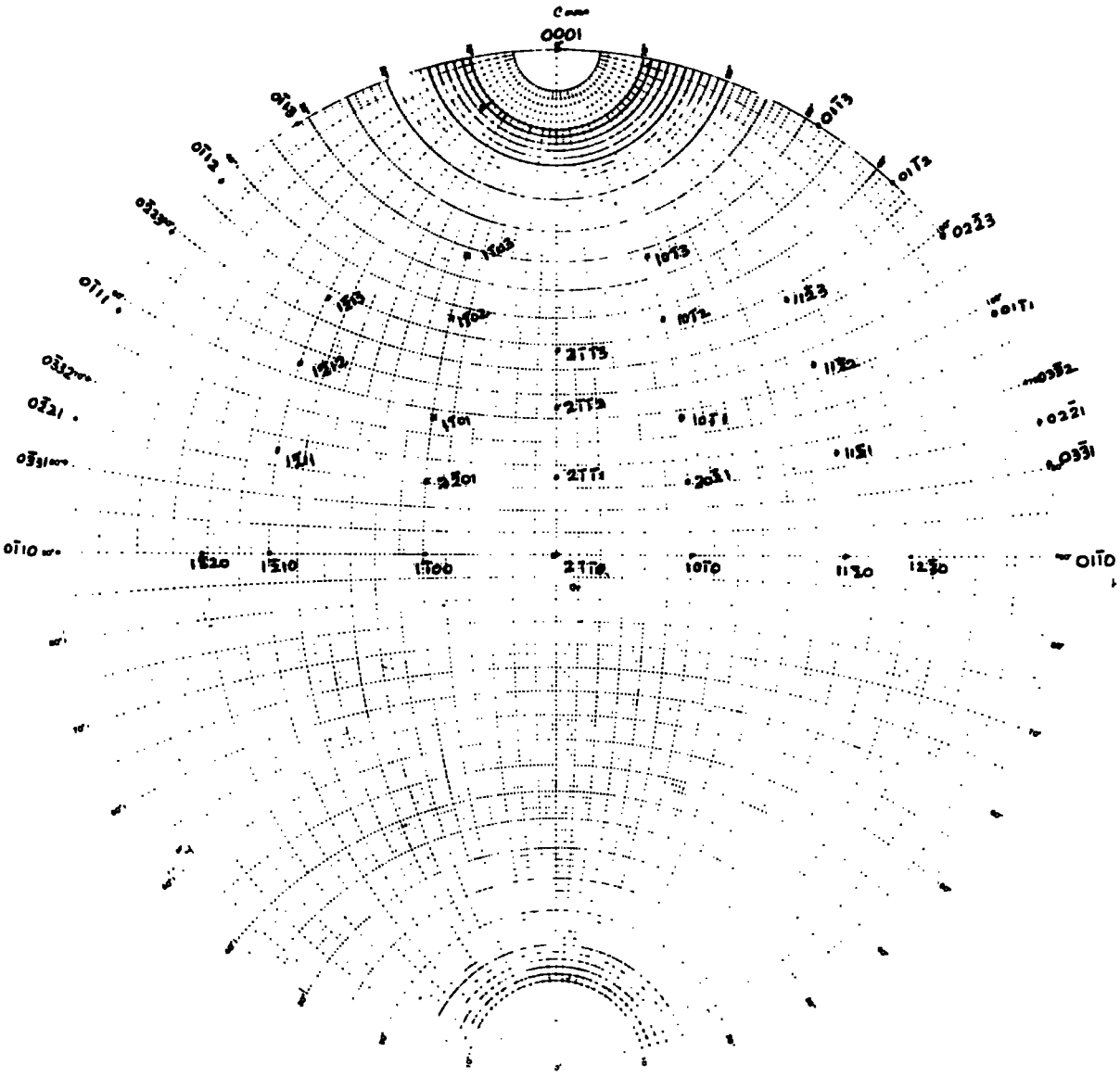
C
0001
$01\bar{1}3$
$01\bar{1}2$
$02\bar{2}3$
$01\bar{1}1$
$02\bar{2}1$
$03\bar{3}1$
$01\bar{1}0$
$\bar{1}\bar{1}23$
$\bar{1}\bar{1}22$
$\bar{1}\bar{1}21$
$\bar{1}\bar{1}20$
$\bar{2}\bar{2}01$
$\bar{1}\bar{1}00$
$2\bar{1}\bar{1}0$
$10\bar{1}0$
$\bar{1}\bar{1}10$
$\bar{1}\bar{2}10$
$\bar{1}\bar{2}20$
$\bar{1}\bar{1}30$
$01\bar{1}0$

A1

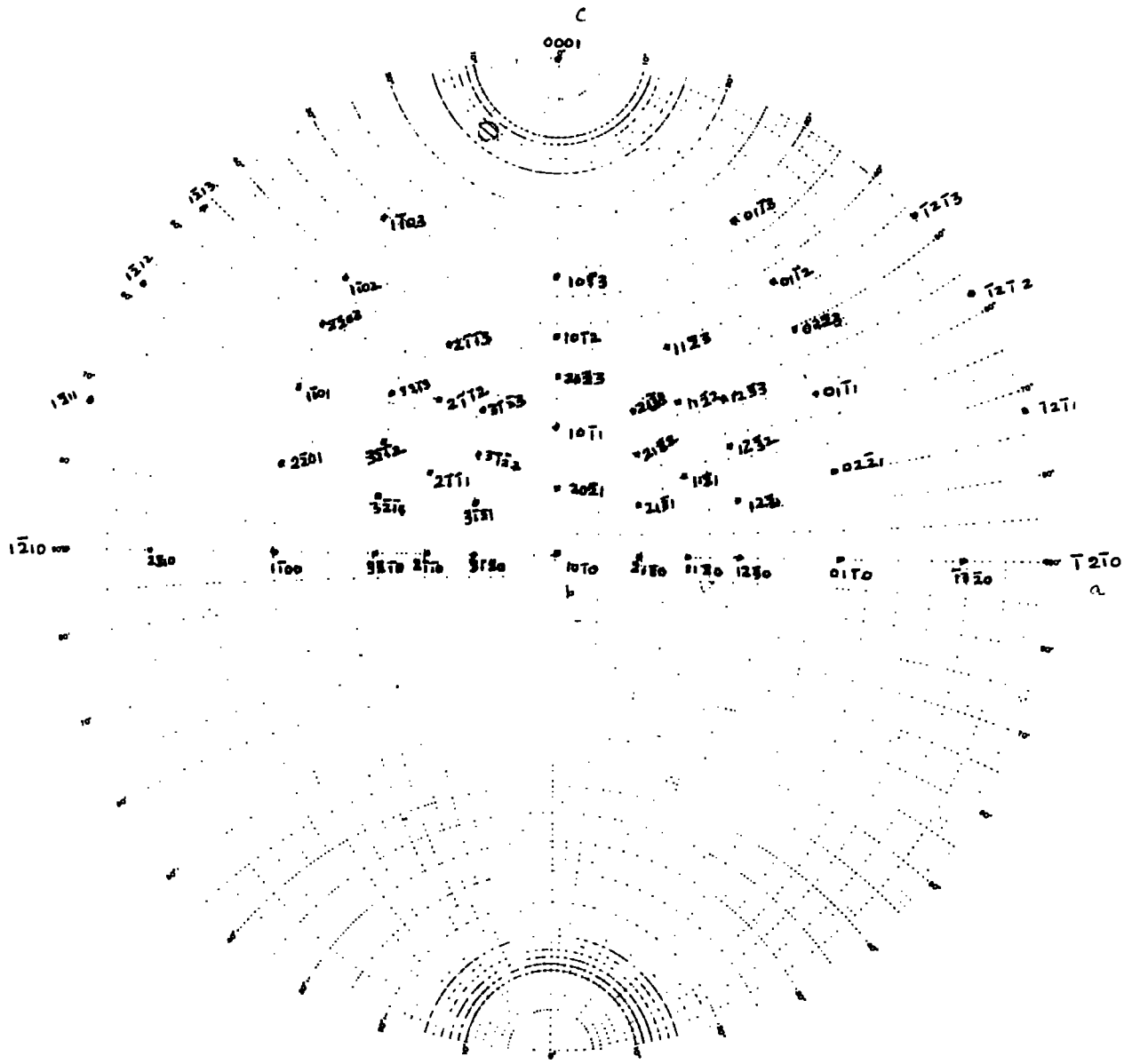

A2

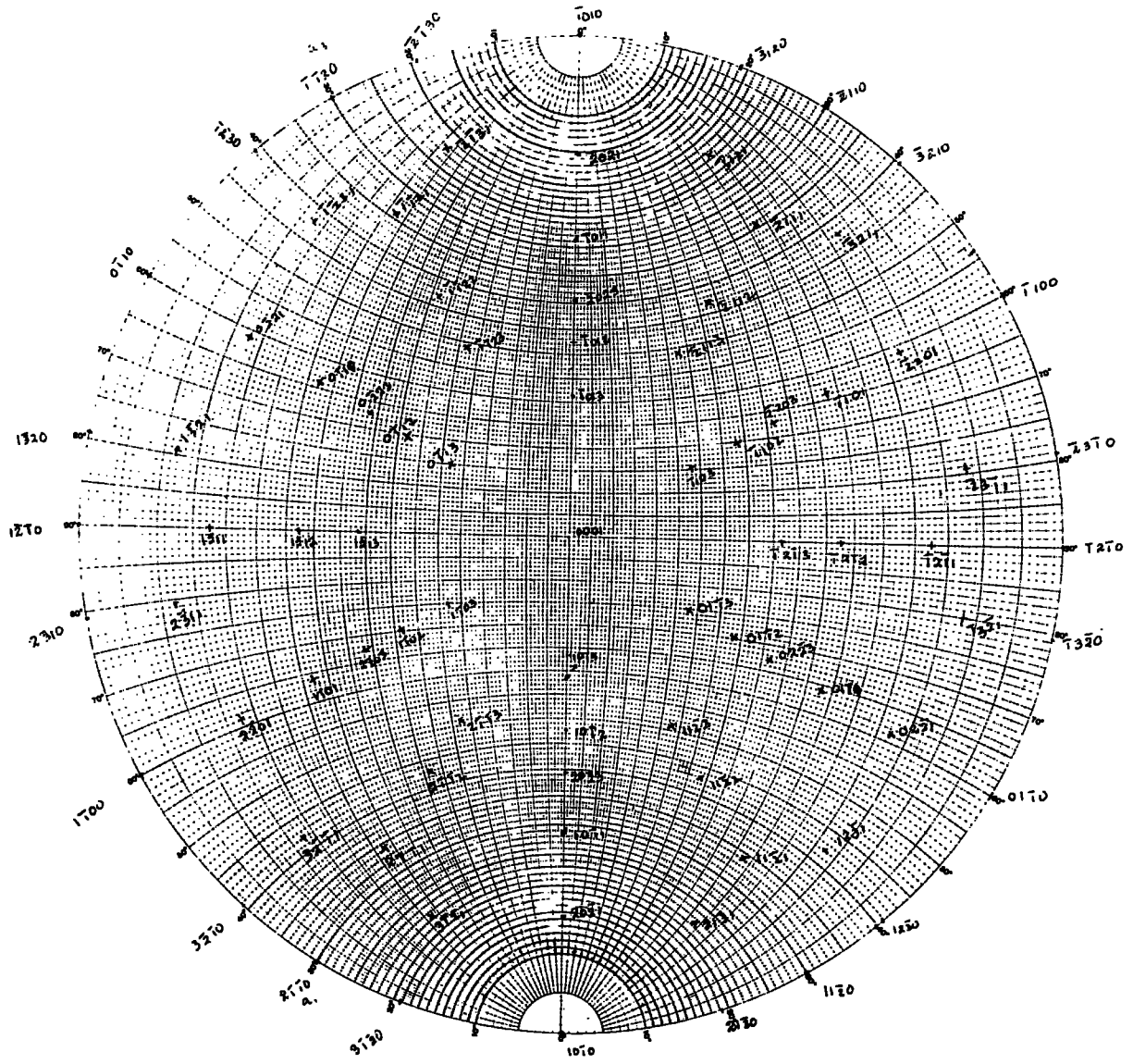

A3

ACKNOWLEDGEMENTS

I should like to express my sincere thanks to my supervisor, Dr. W.D. Corner, for his guidance and help throughout this project.

I am grateful to Professor G.D. Rochester, F.R.S. for the research facilities of the Physics Department and to the staff of the workshops for their technical assistance. I should also like to acknowledge the help of Dr. K.N.R. Taylor and other members of the Rare Earth research group of Durham University.

Thanks are due to Metals Research Ltd. for preparing the single crystals used in this investigation and to Mrs. S. Naylor for typing the manuscript.

I am grateful to all members of my family for their help and encouragement.

REFERENCES

1. K.A. GSCHNEIDNER. 'Rare Earth Alloys' published by D. Van Nostrand & Co., 1961.

2. S. CHIKAZUMI. 'Physics of Magnetism' published by John Wiley & Sons, 1964.

3. M.K. WILKINSON, H.R. CHILD, C.J. McHARGUE, W.C. KOEHLER and E.O. WOLLAN. Phys. Rev. 122, 1409, 1961 (Ce)

4. J.W. CABLE, R.M. MOON, W.C. KOEHLER and E.O. WOLLAN Phys. Rev. Letts. 12, 553, 1964. (Pr)

5. R.M. MOON, J.W. CABLE and W.C. KOEHLER, J.A.P. Suppl. 35, 1041, 1964. (Nd)

6. N.G. NEARSON, C.E. OLSEN and H.A. ALPERIN, Phys. Rev. 135, A176, 1964. (Eu)

7. G. WILL, R. NATHANS and H.A. ALPERIN, J. Appl. Phys. 35, 1045, 1964 (Gd)

8. J.W. CABLE and E.O. WOLLAN, Phys. Rev. 165, 733, 1968. (Gd)

9. W.C. KOEHLER, H.R. CHILD, E.O. WOLLAN and J.W. CABLE, J. Appl. Phys. 34, 1335, 1963. (Tb)

10. W.C. KOEHLER, H.R. CHILD, E.O. WOLLAN and J.W. CABLE J. Appl. Phys. 32, 48S, 1961. (Dy)

11. W.C. KOEHLER, J.W. CABLE, M.K. WILKINSON and E.O. WOLLAN, Phys. Rev. 151, 414, 1966. (Ho)

12. J.W. CABLE, E.O. WOLLAN, W.C. KOEHLER and M.K. WILKINSON, Phys. Rev. 140, 1896, 1965. (Er)

13. W.C. KOEHLER, J.W. CABLE, E.O. WOLLAN and M.K. WILKINSON. Phys. Rev. 126, 1672, 1962. (Tm)

14. B. LEBECH and B.D. RAINFORD, J. de Phys. 32, C1-370, 1971.

15. H.E. NIGH, S. LEGVOLD and F.H. SPEDDING, Phys. Rev. 132, 1092, 1965.

16. W.D. CORNER, W.C. ROE and K.N.R. TAYLOR, Proc. Phys. Soc. 80, 927, 1962.

17. C.D. GRAHAM, Jr., J. Phys. Soc. Japan, 17, 1310, 1962.

18. S.H. LIU, Phys. Rev. 123, 470, 1961.

19. K.P. BELOV, R.Z. LEVITIN, S.A. NIKITIN and A.V. PEDKO, Sov. Phys. JETP 13, 1096, 1961.

20. D.E. HEGLAND, S. LEGVOLD and F.H. SPEDDING, Phys. Rev., 131, 158, 1963.

21. D.R. BEHRENDT, S. LEGVOLD and F.H. SPEDDING, Phys. Rev., 109, 1544, 1958.

22. D.L. STRANDBURG, S. LEGVOLD and F.H. SPEDDING, Phys. Rev. 127, 2046, 1962.

23. W.C. KOEHLER, J.W. CABLE, H.R. CHILD, M.K. WILKINSON and E.O. WOLLAN. Phys. Rev. 158, 450, 1967.

24. R.W. GREEN, S. LEGVOLD and F.H. SPEDDING, Phys. Rev. 122 827, 1961.

25. R.B. FLIPPEN, J. Appl. Phys. 35, 1047, 1964.

26. R.Z. LEVITIN and B.K. PONOMAREV, Sov. Phys. JETP, 26, 1121, 1968.

27. J.J. RHYNE, S. FONER, E.J. McNIFF, Jr. and R. DOCLO, J. Appl. Phys. 39, 892, 1968.

28. M. SCHIEBER, S. FONER, R. DOCLO and E.J. McNIFF, Jr. J. Appl. Phys. 39, 885, 1968.

29. K.P. BELOV, R.E. LEVITIN and S.A. NIKITIN, Sov. Phys. Uspekhi 7, 179, 1964.

30. R.J. ELLIOT in MAGNETISM VOL. IIA ed by G.T. RADO and H. SUHL published by Academic Press, 1965.

31. T. KASUYA in MAGNETISM VOL. IIB same as ref. 30.

32. R.M. BOZORTH and C.D. GRAHAM, Jr. I.B.M. Res.Reports Rc 1635, 1966.

33. B.R. COOPER in Solid State Physics Vol. 21 published by Academic Press, 1968.

34. K.N.R. TAYLOR, Contemp. Physics 11, 423, 1970.

35. C. ZENER. Phys. Rev. 81, 440, 1951
83, 299, 1951

36. M.A. RUDERMANN and C. KITTEL, Phys. Rev. 96, 99, 1954.

37. T. KASUYA, Progr. Theoret. Phys. (Kyoto), 16, 45, 1956.

38. K. YOSIDA, Phys. Rev., 106, 893, 1957.

39. P.G. De GENNES, Compt.Rend. 247, 1836, 1958.

40. L.M. ROTH, H. ZEIGER and T.A. KAPLAN, Phys. Rev. 149, 579, 1966.

41. F. SPECHT, Phys. Rev. 162, 389, 1967.

42. R.M. BOZORTH and R.J. GAMBINO, Phys. Rev. 147, 487, 1966.

43. R.M. BOZORTH, J. Appl. Phys. 38, ~~1866~~ 1366, 1967.

44. R.M. BOZORTH, R.J. GAMBINO and A.E. CLARK, J. Appl. Phys., 39, ~~853~~ 883, 1968.

45. W.C. THOBURN, S. LEGVOLD and F.H. SPEDDING, Phys. Rev. 110, 1298, 1958.

46. S. WEINSTEIN, R.S. CRAIG and W.E. WALLACE, J. Appl. Phys. 34, 1354, 1963.

47. S. WEINSTEIN, R.S. CRAIG and W.E. WALLACE, J. Chem. Phys. 39, 1449, 1963.

48. H.R. CHILD, W.C. KOEHLER, E.O. WOLLAN and J.W. CABLE, Phys. Rev. 138, A1655, 1965.

49. H. NAGASAWA and T. SUGAWARA, J. Phys. Soc. Japan, 23, 711, 1967.

50. V.A. FINKEL and V.V. VOROBEV, Sov. Phys. JETP., 26, 1086, 1968.

51. H.E. NIGH, S. LEGVOLD, F.H. SPEDDING and B.V. BEAUDRY, J. Chem. Phys, 41, 3799, 1964.

52. H.R. CHILD and W.C. KOEHLER, J. Appl. Phys. 37, 1353, 1966.

53. H.R. CHILD and W.C KOEHLER, Phys. Rev. 174, 562, 1968.

54. E.O. WOLLAN, J. Appl. Phys. 38, 1371, 1967.

55. E.O. WOLLAN, Phys. Rev. 160, 369, 1967.

56. A.H. MORRISH, 'The Physical Principles of Magnetism' published by John Wiley & Sons, 1965.

57. W. HEISENBERG, Z. Physik 49, 619, 1928.

58. S. LIU, D.R. BEHRENDT, S. LEGVOLD and R.H. GOOD, Phys. Rev., 116, 1464, 1959.

59. U. ENZ, J. Appl. Phys. 32, 22S, 1961.

60. A. YOSHIMORI, J. Phys. Soc. Japan, 14, 807, 1959.

61. A. HERPIN and P. MERIEL, J. de Physique, 22, 337, 1961.

62. H. MIWA and K. YOSIDA, Progr. Theor. Phys.(Kyoto) 26, 693, 1961.

63. T. NAGAMIYA in Solid State Physics, Vols. 20 and 22 published by Academic Press.

64. R.J. ELLIOT, Phys. Rev. 124, 346, 1961.

65. J.J. RHYNE and A.E. CLARK, J. Appl. Phys. 38, 1379, 1967.

66. P.H. BLY, W.D. CORNER, K.N.R. TAYLOR and M.I. DARBY, J. Appl. Phys. 39, 1336, 1968.

67. J.L. FERON, G. HUG and R. PAUTHENET, Proc. C.N.R.S. Grenoble Conf. Vol. 2, 19,1970.

68. W.P. MASON, Phys. Rev. 96, 302, 1954.

69. E.R. CALLEN and H.B. CALLEN, Phys. Rev. 129, 578, 1963.

70. E.R. CALLEN and H.B. CALLEN, Phys. Rev. 139, A455, 1965.

71. A.E. CLARK, B.F. De SAVAGE and R. BOZORTH, Phys. Rev. 138, A216, 1965.

72. M. ABRAMOWITZ and I.A. STEGUN. 'The Handbook of Mathematical Functions' published by Dover Pub. Inc. 1965.

73. W.A. ROMAN. G.E. Technical Information Series Rep. No. 65-C-017.

74. B.G. KOEPKE and T.E. SCOTT. Trans. Met. Soc. AIME, 236, 1363, 1966.

75. C.S. BARRETT. 'Structure of Metals' McGraw Hill Book Co. 1952.

76. A.L. BIERMASZ and H. HOEKSTRA, Philips Tech. Rev. 11, 23, 1950.

77. F.C. NIX and D. McNAIR, Phys. Rev. 60, 597, 1941.

78. W.C. ROE, Ph.D. Thesis (Durham University), 1961.

79. A.R. PIERCY, Ph.D. Thesis (Durham University), 1968

80. P. WEISS and R. FORRER, Ann Phys. (Paris), 12, 279, 1929.

81. H. ZIJLSTRA. Experimental Methods in Magnetism Vol. 2 p. 72, published by North-Holland Publishing Co. 1967.

82. D.T. NELSON and S. LEGVOLD, Phys. Rev. 123, 80, 1961.

83. D.B. McWHAN and A.L. STEVENS, Phys. Rev. 154, 438, 1967.

84. F. MILSTEIN and L.B. ROBINSON, Phys. Rev. 159, 466, 1967.

85. H.R. CHILD, private communication.

86. F.J. DARNELL and E.P. MOORE, J. Appl. Phys. 34, 1337, 1963.

87. H.S. JARRETT and R.J. ELLIOT, J. Phys. Soc. Japan, 17-B-1, 8, 1962.

88. P. LANDRY and R. STEVENSON, Can. J. Phys. 41, 1273, 1963.

89. E.W. LEE, Proc. Phys. Soc. 84, 693, 1964.

90. J.J. RHYNE, S. LEGVOLD and E.T. RODINE, Phys. Rev. 154, 266, 1967.

91. P.C. LANDRY, Phys. Rev. 156, 578, 1967.

92. S.B. PALMER, private communication.

93. H. BJERRUM MØLLER, J.C. GYLDEN HOUMANN and A.R. MACKINTOSH, J. Appl. Phys. 39, 807, 1968.

94. E.S. FISHER and D. DEVER, Trans. Met. Soc. AIME, 239, 48, 1967.

95. M. LONG Jr. A.R. WAZZAN and R. STERN, Phys. Rev. 178, 775, 1969.

96. M. ROSEN and H. KLIMMER, Phys. Rev. B. 1, 3748, 1970.

97. D.B. McWHAN, E. CORENZWIT and A.L. STEVENS, J. Appl. Phys. 37, 1355, 1966.

98. R.M. McCLINTOCK, Rev. Sci. Instr. 30, 715, 1959.